Ablation of hard biological tissue and osteotomy with pulsed CO_2 lasers

Inaugural-Dissertation

zur

Erlangung des Doktorgrades der
Mathematisch-Naturwissenschaftlichen Fakultät
der Heinrich-Heine-Universität Düsseldorf

vorgelegt von
Martin Werner
aus Essen
2006

Aus dem Institut für Lasermedizin
der Heinrich-Heine Universität Düsseldorf

Gedruckt mit der Genehmigung der
Mathematisch-Naturwissenschaftlichen Fakultät der
Heinrich-Heine-Universität Düsseldorf

Referent: Prof. Dr. P. Hering
Koreferent: Prof. Dr. K. Schierbaum

Tag der mündlichen Prüfung: 16.11.2006

Meinem Bruder

Summary

This thesis describes a variety of experiments and results concerning the ablation of hard biological tissue, mainly compact bone, with pulsed CO_2 lasers. Laser processing of bone is a very complicated task since bone consists of different components with very different physical properties that give bone its combination of flexibility and solidity. While the mineral bone component melts at temperatures above 1280°C, bone cells will already be damaged by minor temperature rises above 42°C.

The process model for hard tissue ablation with pulsed IR lasers is the so-called thermo-mechanical ablation. It is based on the fast evaporation of the enclosed tissue water and the resulting strong pressure increase that tears the tissue apart and ejects parts of the tissue. The very strong absorption of the CO_2 laser radiation in the bone enables a highly localised energy deposition.

One aim of this thesis is the detailed analysis of the ablation process of bone with pulsed CO_2 lasers. The dependence of the ablation efficiency on the water content of the bone tissue was examined. Therefore, bone samples with different water contents were irradiated with a pulsed CO_2 laser. For analysis, optical measurements of the ablation depth and -volume, morphological examinations of the surface of the laser incisions with <u>s</u>canning <u>e</u>lectron <u>m</u>icroscopy (SEM) were conducted. The chemical composition of cut surfaces was determined with <u>e</u>nergy <u>d</u>ispersive <u>X</u>-ray fluorescence spectroscopy (EDX). The results of these examinations support the thermo-mechanical process model for hard tissue ablation with pulsed CO_2 lasers.

Temperature measurements with an IR camera showed only minor temperature rises of the surrounding tissue during the correct application of the multi pass scan procedure in combination with a fine water spray, a procedure for bone tissue ablation that was developed in our research group and presented in this thesis.

Moreover, comparative measurements of the ablation efficiency with different CO_2 lasers and an excimer laser system as well as measurements with a scanning technique for widening the laser incision were conducted. This gave valuable insights into the practical use of this technique. An additional, artificial widening of the incisions enables deep incisions (up to 20 mm). As a result, the multi pass scan procedure in combination with a cut dilation technique presented in this thesis makes a practical medical application of laser osteotomy in hard tissue surgery possible for the first time.

Kurzfassung

In dieser Arbeit wird die Ablation von biologischem Hartgewebe, hauptsächlich kompaktem Knochen, mit gepulsten CO_2-Lasern untersucht. Knochengewebe ist ein sehr schwieriges Material für die Laserbearbeitung, da es aus verschiedenen Komponenten zusammengesetzt ist, deren Eigenschaften dem Knochen seine Kombination von Flexibilität und Festigkeit geben. Während der mineralische Knochenbestandteil erst bei Temperaturen oberhalb 1280°C schmilzt, können Knochenzellen schon bei leichtem Temperaturanstieg über 42°C geschädigt werden.

Das Prozessmodell für die Ablation von Hartgewebe mit gepulsten IR Lasern ist die so genannte thermo-mechanische Ablation. Sie beruht auf der schnellen Verdampfung des eingeschlossenen Gewebswassers, verbunden mit einem starken Druckanstieg, der das Gewebe zerreißt. Die sehr starke Absorption der Strahlung des CO_2 Lasers im Knochen ermöglicht eine sehr lokalisierte Energiedeponierung.

Ein Ziel dieser Arbeit ist die genaue Analyse des Ablationsprozesses von Knochen mit gepulsten CO_2 Lasern. Untersucht wurde die Abhängigkeit der Ablationseffizienz vom Wassergehalt des Knochengewebes. Hierfür wurden Knochen mit unterschiedlichem Wassergehalt mit einem gepulsten CO_2 Laser bestrahlt. Zur Auswertung wurden optische Messungen der Ablationstiefe, des Ablationsvolumens sowie morphologische Untersuchungen der Oberflächen der Schnitte mittels Rasterelektronenmikroskopie (REM) durchgeführt. Für die Bestimmung der chemischen Zusammensetzung der Schnittoberflächen wurde die energiedispersive Röntgenfluoreszenzspektroskopie (EDX) verwendet. Die gewonnenen Daten unterstützen das thermo-mechanische Prozessmodell der Hartgewebeablation mit gepulsten CO_2 Lasern.

Temperaturmessungen mit einer IR Kamera belegen eine nur geringe Erwärmung des umliegenden Gewebes bei korrekter Anwendung des in der Arbeitsgruppe entwickelten und in dieser Arbeit vorgestellten Multi-Pass-Scan-Verfahrens für Knochenschnitte bei gleichzeitiger Verwendung eines feinen Wassersprays während der Lasereinwirkung.

Weiterhin werden für die praktische Anwendung des Verfahrens relevante Untersuchungen zum Vergleich der Abtragseffizienz von verschiedenen CO_2- und einem Excimerlaser sowie Techniken zur Schnittaufweitung durchgeführt. Eine künstliche Erweiterung der Spaltbreite des Laserschnittes ermöglicht es tiefe Schnitte zu erzielen (bis 20 mm). Das vorgestellte Multi-Pass-Scan-Verfahren in Kombination mit einer Schnittaufweitung ermöglicht erstmals eine praktische Anwendung der Laserosteotomie in der Hartgewebechirurgie.

Figures

Figure	Chapter	Title
2.1	2.1	The epiphysis and part of the diaphysis of a long bone
2.2	2.1	Internal features of a portion of the diaphysis of a long bone
2,.3	2.2	The hierarchical structure of bone
2.4	2.2	Osteon structures in bone
2.5	2.4.3	Absorption properties of human cortical femur bone
3.1	3.2.2	Temporal evolution of surface temperature (z=0) in the one dimensional model
4.1	4.1.1	Temporal pulse profile TEA CO_2 laser (MTL 3)
4.2	4.1.1	Temporal pulse profile slab CO_2 laser (RS SC x 30)
4.3	4.1.2	Schematic view of experimental set-up with drive stage
4.4	4.1.2	Schematic view of experiment. set-up with laser beam scanner
4.5	4.2	Overview over sample preparation after laser irradiation
4.6	4.2	Illustration of geometrical pulse overlap factor *n = 1*
4.7	4.3	Average ablation depth per pulse δD against incision depth D for the TEA CO_2 laser and the slab CO_2 laser
4.8	4.3	Specific ablation energy W_{sp} against incision depth D for the TEA CO_2 laser and the slab CO_2 laser
5.1	5.1.1	Incision depth D against equivalent pulse number N_{eq} for laser incision with TEA CO_2 laser in different sample groups
5.2	5.1.1	Specific ablation energy in J/mm^3 against incision depth D in mm for laser incision with TEA CO_2 laser in different sample groups
5.3 - 5.4	5.1.2.1	SEM image of a laser incision in pure hydroxyapatite
5.5 - 5.9	5.1.2.2	SEM image of a laser incision in ethanol dehydrated bone
5.10 - 5.14	5.1.2.3	SEM image of a laser incision in acetone dehydrated bone
5.15 – 5.18	5.1.2.4	SEM image of a laser incision in fresh bone
5.19	5.1.3.1	EDX X-ray fluorescence spectrum: untreated surface of fresh bone
5.20	5.1.3.1	EDX X-ray fluorescence spectrum: surface of laser incision in fresh bone
5.21	5.1.3.2	EDX X-ray fluorescence spectrum: non-irradiated surface of a bone from ethanol preparation
5.22.a&b	5.1.3.2	EDX X-ray fluorescence spectrum: surface of laser incision in a bone from ethanol preparation
5.23	5.2.1	Spectral sensitivity of the QWIP detector in the Flir SC 3000 camera
5.24	5.2.2	Experimental set-up for temperature measurements during laser ablation
5.25.a	5.2.3	Temperature distribution T(x,y) during laser drilling (no beam movement) at backside of bone sample (thickness 1 mm) directly before breakthrough (T_{max} = 344°C), air jet applied on irradiation spot on front side
5.25.b	5.2.3	Colour-coded temperature distribution T(x,y) during laser drilling (no beam movement) at backside of bone sample (thickness 1 mm) directly before breakthrough (T_{max} = 344°C), air jet applied to irradiation spot on front side
5.26.a	5.2.3	Temperature distribution T(x,y) during laser drilling (no beam movement) at backside of bone sample (thickness 1.3 mm) directly before breakthrough (T_{max}= 142°C), water spray applied to irradiation spot on front side

Tables

Table	Chapter	Title
2.1	2.3.2	Thermal properties of bone
2.2	2.3.3	Absorption coefficients of the particular bone components
2.3	2.3.3	Calculated absorption coefficients
5.1	5.1	Overview of different sample groups used for experiments
5.2	5.1.3	Overview of presented EDX spectra
5.3	5.1.3.2	Relative occurrence of the different elements in the examined area of the ethanol prepared bone sample
5.4	5.2.1	Specifications of the Flir SC 3000 camera
6.1	6.1	Laser parameter used in the described experiments
A.1	Appendix A	Parameters of the prototype laser osteotome "osteoLAS" used during the in-vivo trials on the tibiae of sheep
A.2	Appendix A	Overview of the first series of in-vivo laser osteotomy of tibia of sheep
A.3	Appendix A	Overview of the second series of in-vivo laser osteotomy of tibia of sheep
B.1	Appendix B	Overview of laser bores in teeth
B.2	Appendix B	Overview of SEM images of laser irradiated teeth
T.1	Appendix T	Estimation of the emissivity ε of compact bone dependent on the filtering of the camera

Contents

1 Introduction

Already soon after T. Maiman had built the first working laser in 1960 [Mai60] the possible use of lasers for medical applications was investigated [e.g. Zar61]. Nowadays lasers have gained access to various fields of medicine as standard instruments and are widely used in medical treatment as well as diagnostics. Areas to which the laser has introduced fundamentally new treatment options are, first and foremost, ophthalmology and dermatology. The first useful medical application was introduced in 1963 when Campbell et al. evaluated the use of the ruby laser to treat retinal detachment [Cam63]. In the following decades, many other medical disciplines incorporated the laser in their treatment spectrum. There are also modern diagnostic techniques based on the use of laser as a light source such as the OCT (optical coherence tomography) [Hua91] for morphological tissue imaging, the spectroscopic detection of trace gases in human breath as indicators of certain diseases [Mür05] or for holographic facial topometry [Fre05].

However, the field of hard tissue processing, like cutting and ablation in standard medical practice, has not been made available to the application of the laser yet. In principle the processing of hard tissue in medical interventions has not changed over the last several thousand years [Alt97, Cap06]. Simple mechanical tools like saws, drills, burs or mills are still used. Because of friction these methods can cause severe mechanical trauma, pain and thermal damage to the adjacent remaining tissue. Moreover, the mechanical processing of hard tissue with a saw limits the choice of incision geometry drastically since only straight cuts or large radii of curvature are applicable.

The research and first experiments on the use of laser for ablation of hard biological tissue started in 1964 when Stern et al. [Ste64] vaporised dental enamel

with pulses from a ruby laser. During the 1970ies and the beginning of the 1980ies studies conducted mainly with cw- or long-pulsed medical CO_2 laser systems developed for soft tissue applications caused severe thermal side effects like carbonisation and the melting of the bone minerals [Hor77, Ger81]. This resulted in significantly delayed bone healing in animal experiments. The results achieved during that time did not allow thinking of lasers as a tool for hard tissue surgery.

Despite these problems the possible advantages of laser osteotomy (cutting of bone) are obvious. First of all the use of lasers for osteotomies offers completely free cut geometries. The possibility of computer controlled steering of the laser beam with motorised optics allows highly precise and accurate cutting of bone with minimised loss of bone tissue. This can be essential for certain interventions e.g. maxillofacial surgery. Because there is no direct contact with the bone, the procedure reduces mechanical trauma induced to the bone tissue [Fre03]. Moreover due to the absence of metal abrasion, no disturbing artefacts in NMR imaging are created from small metal particles left in the incision, which is especially important for neuro-surgical interventions.

During the 1980ies and 1990ies it was shown that biocompatible and effective hard tissue ablation with short pulsed laser systems, which are strongly absorbed in the respective tissue, is possible [Hib89, Wal89, For93, Iva98]. The laser systems considered to be successful in practice are the Er:YAG-, the Er:YSGG- and the CO_2 laser, of which radiations are very strongly absorbed in hard tissue.

Laser ablation of hard tissue is not a straightforward task. However, the structural composition and the natural water content of hard tissue can be exploited to induce an effective and clean thermo-mechanical ablation process in the case of pulsed middle-infrared laser systems. This ablation process is based on the fast evaporation of enclosed tissue water which tears the bone apart in micro-explosions.

The structure of bone and its physical properties in relation to laser ablation are described in the second chapter of this thesis.

An overview of hard tissue ablation processes with different laser systems and a description of the thermo-mechanical laser ablation model will be given in chapter 3.

Chapter 4 describes the CO_2 laser systems used for bone tissue ablation experiments presented in this thesis.

In the model of the thermo-mechanical ablation process of hard tissue with pulsed IR lasers the fast evaporation of water is the driving force for material removal. To verify this model, the influence of the internal water content in the bone on the ablation efficiency is examined in the thesis. Morphological analysis of the irradiated bone sample with a scanning electron microscope and the examination of the chemical composition with energy dispersive X-ray spectroscopy complete the analysis of the ablation process. The temperatures arising during the ablation process were measured with a fast IR camera system. These studies regarding the mechanism of the ablation process are presented in chapter 5 of this thesis.

Chapter 6 contains examinations concerning the practical use of lasers for osteotomy. A comparison of the bone tissue ablation efficiencies with different pulsed laser systems and different irradiation techniques are presented here.

Some medical applications and first clinical in-vivo trials with the laser system developed in our group are summarised in the appendix for completeness.

2 Bones

In this chapter the material "bone", which was used for the experiments, will be introduced. First, the anatomy of bone and the hierarchical structure from large to small structures will be shortly described. The composition of bone will be explained with emphasis on the properties, which are important for laser ablation. Finally, the mechanical, thermal and optical properties of bone tissue will be summarised from the literature. At the end of this chapter, the reader will have an idea why laser processing of bone is not a simple task, and which parameters are essential to achieve effective and cautious laser bone ablation.

2.1 Anatomy of Bones

The bones in the skeletal systems fulfil structural functions like support and movement of the whole body, protection of the inner organs, as well as metabolic functions like storage of calcium and phosphate and blood cell formation in the bone marrow. Bone has four basic shapes: long bones, e.g. the femur; short bones, as wrist or ankle bones; flat bones, like skull bones or the sternum; and irregular bones with no distinct form, such as vertebrae and some facial bones. Bone is structured in dense compact bone and spongy cancellous bone as seen in figure 2.1 and 2.2. A long bone is subdivided into a diaphysis, the shaft of the bone, mostly consisting of compact bone and the epiphysis situated at the end of the bone which is mainly cancellous bone covered with a layer of compact bone and cartilage at the articulations. Inside a long bone lies the medullary cavity, which is filled with bone marrow. In long bones of adults, it is mostly adipose yellow bone marrow, while the red bone marrow responsible for the blood cell formation is situated in the bones in the torso and skull bones.
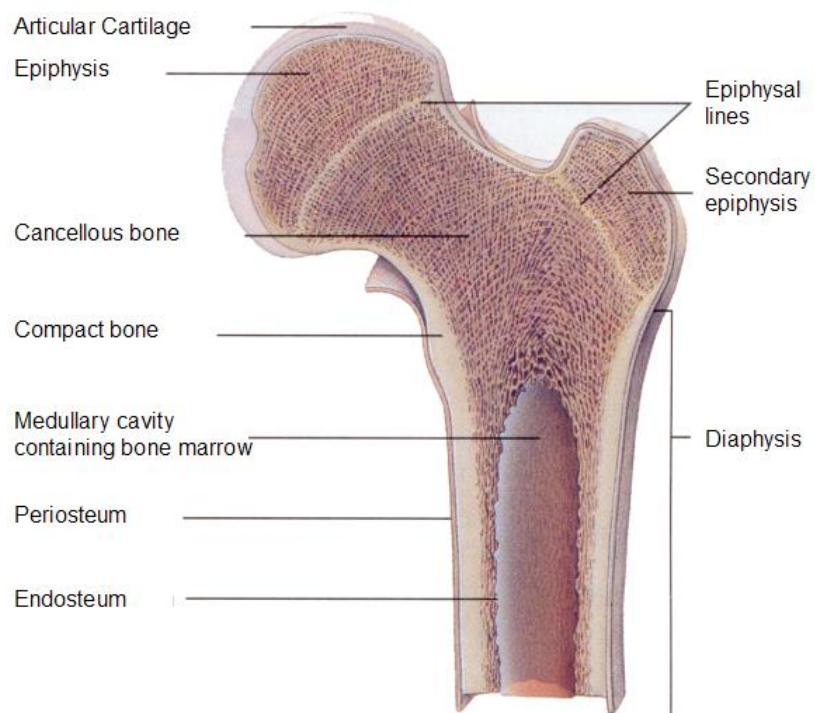
Figure 2.1: The epiphysis and part of the diaphysis of a long bone [See98]

The bone seen in figure 2.2 is covered with the periosteum, a double layered connective tissue. The inner layer consists of a single layer of different types of bone cells.
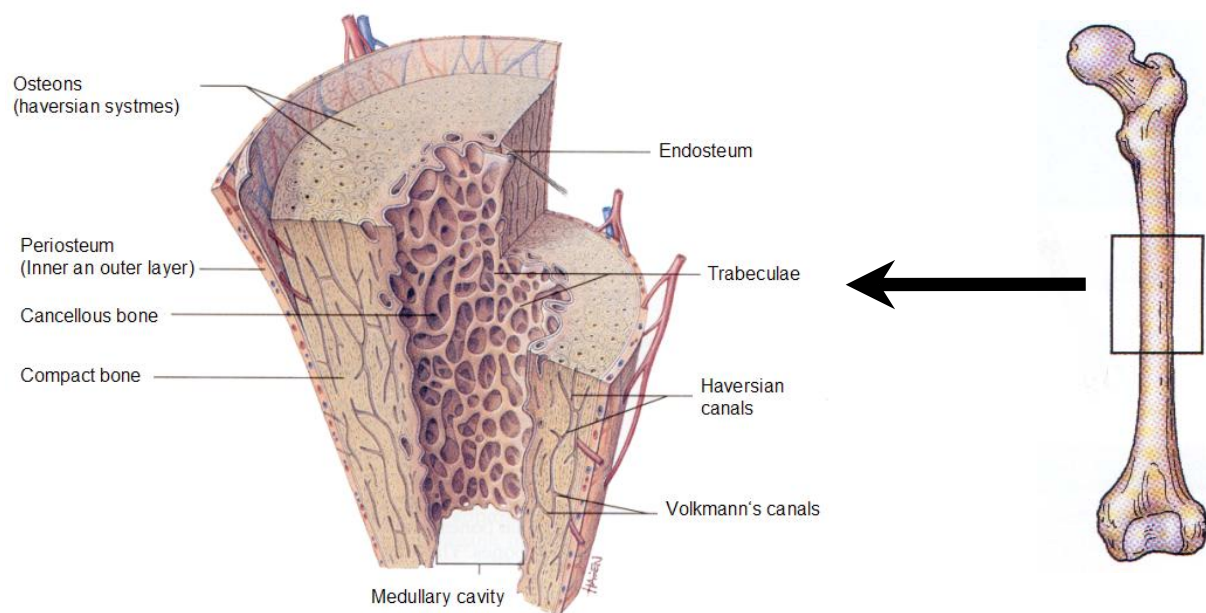
Figure 2.2: Internal features of a portion of the diaphysis of a long bone [See98]

2.2 Structure and Composition of Bone

Bone consists of extracellular bone matrix and bone cells as osteoblasts (bone building cells) and osteoclasts (bone resorbing cells). The composition of the bone matrix determines the physical characteristics of bone and will be described in this section. In this sense, bone is a natural composite material [Mar99, Fun93]. With its structure, it reveals unique properties that match its function. It is important to keep in mind that bone is a living material that contains cells and is subject to constant remodelling processes.

Bone is composed of a matrix of organic collagen fibres (almost entirely collagen type I) and the inorganic component the bone apatite, sometimes called dahllite, which is basically carbonated hydroxyapatite (molecular formula $(Ca_{10}(PO_4)_6(OH)_2)$ [See98, Win02, Fun93, Wei98]. In the comprehensive review of Duck on physical properties of tissue [Duc90], the composition of human cortical bone is given as 55-58% mineral, 25-26% collagen, 12-15% water, and about 1% lipids. These values are weight percentages. The relative volumetric composition percentages can be calculated from this data with the mass densities of the constituents of bone. The volumetric composition is then 36% mineral, 37% collagen, 25% water, and about 2% lipids. In other literature sources, the composition of bone differs slightly from the values given above. For example, Scholz [Sch92] summarises data already published elsewhere and states the following weight percentages: 20% organic matrix (collagen), 50-60% inorganic compounds (hydroxyapatite), and even 20% water.

The macroscopic structure of bone, arranged in hierarchical levels, is shown in figure 2.3.
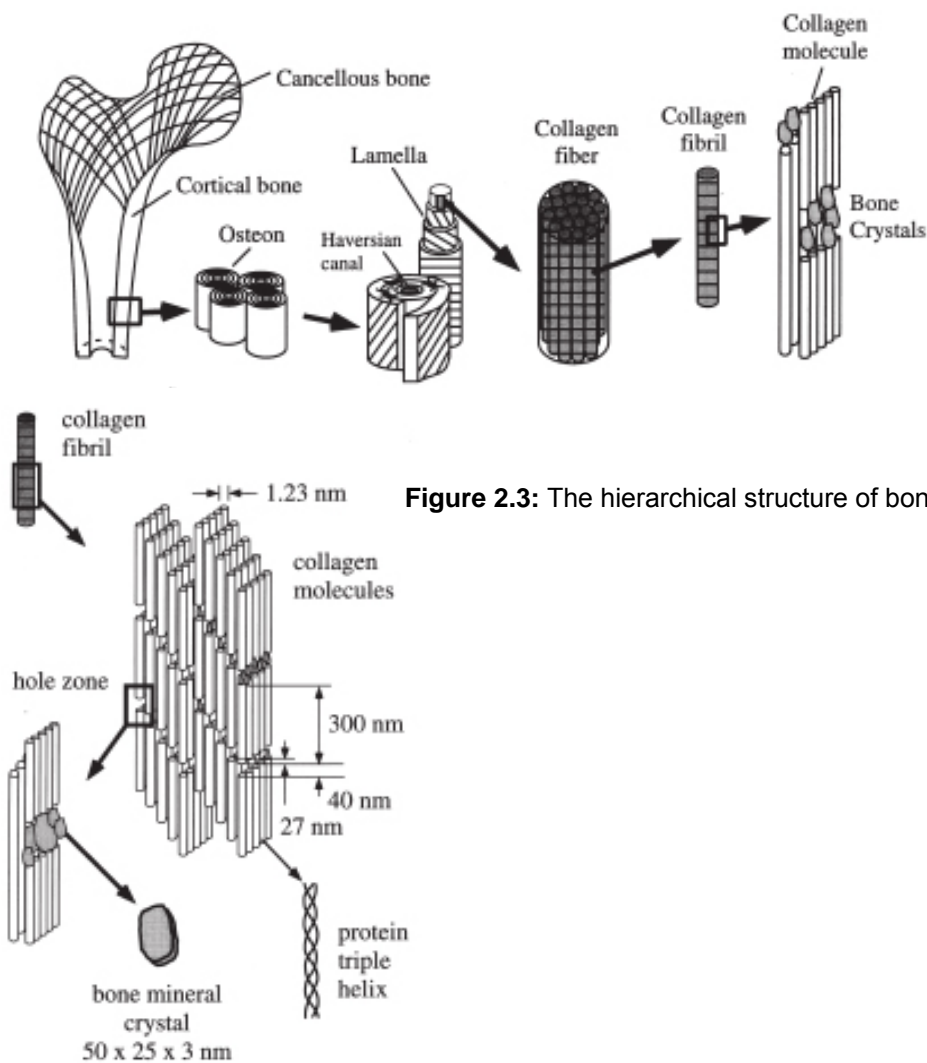
Figure 2.3: The hierarchical structure of bone (after [Rho98]).

Bone is divided into cancellous (trabecular) and compact (cortical) bone. Cancellous bone is generally metabolically more active compared to cortical bone. Due to the more frequent remodelling of cancellous bone, it is in average younger than compact bone. This can influence the microstructure of the bone (e.g. average crystal size of the mineral component) and, consequently, the physical properties, even though the material is the same [Rho98, See98].

Compact bone is composed of regular, cylindrically shaped lamellae, which are between 3 to 7 µm wide. The lamella consists of mineralised collagen fibres. In mature compact bone, 3 to 8 lamellae are wrapped around one central canal. These structures are called osteons or haversian systems. Inside the canal, blood vessels and nerves are situated. The osteons are rather cylindrical and have a diameter of

around 200 µm [Mar99]. The axes of the osteons are approximately parallel to the long axis of the bone. Other forms of compact bone in which the mineralised collagen fibres are less structured, are called woven bone [Rho98]. The collagen fibrils inside one individual lamella are roughly parallel, whereas the orientations of the fibres in adjacent lamellae differ, resulting in a plywood like structure [Wei92, Wei98]. In the collagen fibres, groups of collagen fibrils run parallel to each other and form the fibres. The values for the diameter of the collagen fibrils found in the literature vary from 80 - 100 nm [Wei98] to 500 nm [Rho98]. A more detailed description can be found in the literature cited above.

The main mineral component of the bone is hydroxyapatite ($Ca_{10}(PO_4)_6(OH)_2$). The hydroxyapatite is present in the form of very small plate-shaped crystals. The average value for the size of these plates given in the literature is 50 x 25 nm [Wei92, Wei98, Rho98], but this can vary quite drastically from 10 to 100 nm [Wei92]. The thickness of the plate-shaped crystals is between 2 to 3 nm [Wei92, Rho98]. This makes them the probably smallest crystals which are formed biologically [Wei92]. The crystals show a remarkable uniform thickness in edge-on views in transmission electron microscopy (TEM). Whereas small angle X-ray scattering (SAXS) is the most reliable tool for measuring the small dimensions, the results vary from 1.5 nm for mineralised tendons to 4 nm for some mature bone types [Wei98]. The nano-crystallinity of the hydroxyapatite is of essential importance since the smaller size of the crystals, compared to stoichiometric hydroxyapatite, guarantees a higher solubility, which is important for the metabolic disposability [Win02]. This may be a reason why sintered hydroxyapatite, which is normally micro-crystalline, looses its biocompatibility.

The organic collagen fibres impart flexible strength to the material, whereas the inorganic hydroxyapatite lends the material a high weight–bearing strength and high ultimate tensile strength. The bone matrix can be compared with reinforced concrete. The collagen fibres act like steel bars, and the hydroxyapatite acts like the surrounding concrete. The macroscopic structure of bone, with its haversian

systems (osteons) with blood vessels along the long axis and Volkman's canals with blood vessels running perpendicular to the bone's axis, is shown in figure 2.4.
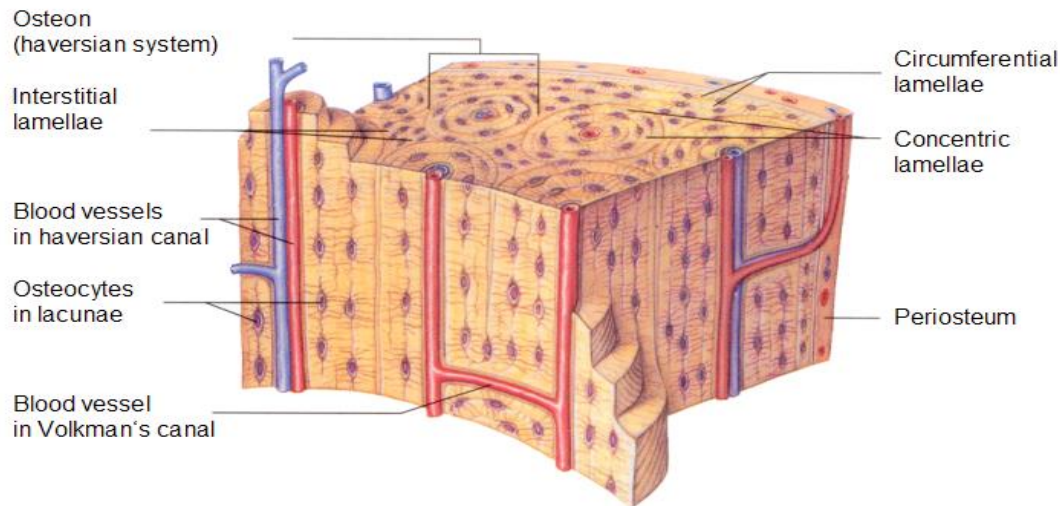
Figure 2.4: Osteon structures in bone [See98]

It has to be emphasised that bone contains biological sensitive structures (e.g. bone cells) which are thermally sensitive and will get damaged already by small temperature rises.

2.3 Physical Properties

In the following section the physical properties of bone material will be summarised from the literature. The values mentioned in this sub-chapter are typical average values for bone tissue. The actual properties vary from bone to bone depending on age, sex, health and species.

2.3.1 Mechanical Properties

Bone is a natural composite material which combines high tensile strength and high stiffness with low weight. The mechanical properties are strongly dependent on the direction of the acting forces. They are determined by the organic collagen fibres as well as the inorganic hydroxyapatite crystals. The collagen fibres mainly take the tension forces, whereas the mineral part takes the compression forces. Bone can bear a strain of about 2%, above this limit the bone fractures. The tensile strength of bone reaches two thirds of the compressive strength. This is why compact bone usually starts fracturing in areas where there is a tensile overload. The value for the elasticity module (Young's module) E varies between 12 and 23.1 GPa [Win02]. In Duck's comprehensive overview of physical properties of tissue, the elasticity module of human femoral compact bone is stated with 18.5 GPa for the longitudinal direction and 12.5 GPa for the transverse direction [Duc90].

Albright states a value of 2 g/cm^3 for the average mass density of compact human bone [Alb79]. Duck gives a value of 1.75 – 2 g/cm^2 for the mass density of compact human femoral bone [Duc90]. The ultimate tensile strength for compact human femoral bone found in the literature is 133 MPa in longitudinal direction and 51 MPa in transverse direction [Duc90]. Scholz determined the ultimate tensile strength for sheep tibia to be 134 MPa [Sch92]. Depending on the orientation and the fraction of collagen fibres in the bone, the properties of bones can vary considerable based on their location.

2.3.2 Thermal Properties

The thermal properties of bone play an important role in the process of laser ablation of bone with IR laser, since the mechanism causing tissue removal is in principal a thermal process. Three parameters are important in characterising the thermal properties of a material: the specific heat capacity c [J (g K)$^{-1}$], the thermal conductivity k [W (m K)$^{-1}$ = J (s m K)$^{-1}$] (often also denoted as λ_H in the literature), a

measure of how good heat is conducted in a material, and the thermal diffusivity or temperature conductivity χ [m^{2}s^{-1}] which is defined as $\chi = k\,(\rho\,c)^{-1}$, where ρ is the mass density and c the specific heat capacity of the material. The values for the specific heat capacity, thermal conductivity, and diffusivity for compact human femur bone found in the literature are summarised in table 2.1.

Table 2.1: Thermal properties of bone

Heat Capacity c [J(gK)$^{-1}$]	Thermal Conductivity k [W (m K)$^{-1}$]	Thermal Diffusivity χ [cm^{2}s^{-1}]	Source
1.5 - 2.37	0.26 - 0.34	$0.1 - 0.13 \cdot 10^{-2}$	Fresh human femur [Biy86]
1.14 – 1.64	0.16 - 0.24	$0.1 – 0.23 \cdot 10^{-2}$	Dry human femur [Biy86]
1.3	0.3 – 0.5	$0.12 - 0.22 \cdot 10^{-2}$ (calculated from given data for c, k and ρ)	Human femur (compact bone) [Duc90]

The thermal properties of bone are important for the efficiency of laser ablation and for the potential thermal damage during laser treatment. They are strongly dependent on the macroscopic structure (compact or cancellous bone), microscopic structure (orientation, size of the osteons), the lipid and water content of the tissue, as well as the vascularisation of the bone. As a result, the values for the heat capacity and the thermal diffusivity determined by Biyikli et al. [Biy86] vary considerably along the long axis of the examined femurs, corresponding to the measured bone fluid content for different positions along the bone's axis. The heat conductivity is relatively constant over the whole length of the femur and is about 50% higher for fresh bone than for dry bone as can be seen in table 2.1.

At elevated temperatures, bone material transformations take place. Collagen is denatured (coagulated) at 60°C and is thermally decomposed (vaporised) at temperatures above 100 °C and then carbonised at temperatures above 150 °C [Nie96, Yan72]. Crystallographic transformations in hydroxyapatite start at temperatures of 400°C [Ste66, Kur86, Fow86, Fea87], melting begins at 1000-1280 °C [Cor74, New77, Nis01].

2.3.3 Optical Properties

The optical properties of hard tissue play a major role in the ablation process. During the interaction of light with matter the energy is conserved. So one can write

$$A + R + S + T = 1 \tag{2.1}$$

A denotes the absorption, *S* the scattering, *R* the reflectivity and *T* the transmission coefficient. Unlike in the visible or near infrared spectral region, scattering in hard biological tissue like bone and tooth is negligible in the middle IR, where CO_2 lasers emit [Fri97]. Reflectance takes place at the tissue surface and can de divided into specular and diffuse components, with the relative portions depending on the surface roughness. The specular reflection happens at smooth surfaces, and the diffuse reflection takes place at interfaces with surfaces which are rough in the optical dimension. The specular (Fresnel) reflection at the interface air / dielectric (like bone, enamel or dentin) is described by following the equation:

$$R = \frac{(n-1)^2 + k_{ext.}^{\;2}}{(n+1)^2 + k_{ext.}^{\;2}} \tag{2.2}$$

n is the refractive index and $k_{ext.}$ the extinction coefficient of the dielectric. The absorption coefficient μ_a of the dielectric is connected to the extinction coefficient $k_{ext.}$ and the wavelength λ by the following equation:

$$\mu_a = \frac{4\pi k_{ext.}}{\lambda} \tag{2.3}$$

The reflection and absorption characteristics of materials, in this case bone or tooth, at or near an absorption band (molecular vibrational modes in the IR region) or an absorption line of the tissue water can vary significantly. Fried et al. [Fri97] have conducted measurements on the reflectance of rough and polished human dentin and enamel for the wavelengths 9.3, 9.6, 10.3, and 10.6 µm with an integrating sphere. For polished human enamel, the reflectance at 9.6 µm is 49 % and at 10.6 µm is 13 %, human dentin reflects 17 % at 9.6 µm and 9 % at 10.6 µm.

For the efficient and "gentle" laser ablation with minimal thermal side effects, a small light penetration depth is needed. This means that a very high absorption of

the laser radiation in the bone tissue is necessary [Iva05]. The light attenuation in material with negligible scattering is described by the Lambert-Beer law:

$$I(z) = I_0 e^{-\mu_a z} \qquad\qquad\qquad\qquad (2.4)$$

I_0 ·is the incident irradiance and I(z) is the irradiance at the depth z in the absorber. The depth at which the irradiance drops to the 1/e level is called optical penetration depth d and is given by:

$$d = \frac{1}{\mu_a} \qquad\qquad\qquad\qquad (2.5)$$

In compact human bone the smallest penetration depths are achieved in the mid-infrared spectral region for the wavelengths near 3 μm, from about 5 to 7 μm and from 9 to 11 μm as can be seen in a transmission spectrum for compact human femur bone in figure 2.5. The optical transmission of human compact bone was investigated by Kar [Kar92] with an FTIR spectrometer. It is very difficult to measure the transmission or absorption properties of strongly absorbing media like bone, enamel or dentin. The absorption around the major absorption bands in the IR region is so strong that a sample with a thickness even below 10 μm would already absorb practically the whole incident radiation. For this reason, mixtures of finely milled and degreased compact bone is moulded with KBr in proportion 1:250 and used for transmission measurements in [Rog03]. However, these measurements do not give very exact results due to changes in the state and composition of the bone material during the described preparation.

The three strong absorption bands are visible in the spectrum in figure 2.5, each mainly attributed to one of the three major constituents of bone. The absorption maximum for bone tissue around 3 μm is attributed to the strong absorption band in water [Rog03]. Almost identical to the strong absorption maximum in water or bone is the wavelength of the Er:YAG laser 2.94 μm. As a result of this, many experiments on hard tissue ablation have been conducted with Er:YAG lasers [e.g. Ape02, Hib97]. These will be described in more details in the next section. The absorption maximum around 5 to 7 μm is caused by absorption due to vibrational modes of proteins (collagen) at 6.1 and 6.45 μm [Pea99, Spe99]. At these wavelengths, only free electron lasers (FEL) are available. Ablation

experiments with FEL yield interesting scientific results, but these systems are not suitable for practical medical applications, e.g. for osteotomy. The strong absorption in the wavelength region of 9 to 11 µm, which coincides with the strongest CO_2 laser lines at 9.6 and 10.6 µm, is caused by three vibrational modes of the phosphate ion-group PO_4^{3-} of the hydroxyapatite. These are symmetric and antisymmetric stretching modes of the P-O bond with transition energies equivalent to wavelengths of 9.2, 9.6, and 10.3 µm [Fri97, Fow66]. High absorption in this wavelength region in water also takes place, but the absorption in the phosphate ion-group of the hydroxyapatite is clearly dominant. The absorption maximum around 16 µm is also mainly caused by absorption in the mineral part of the bone.
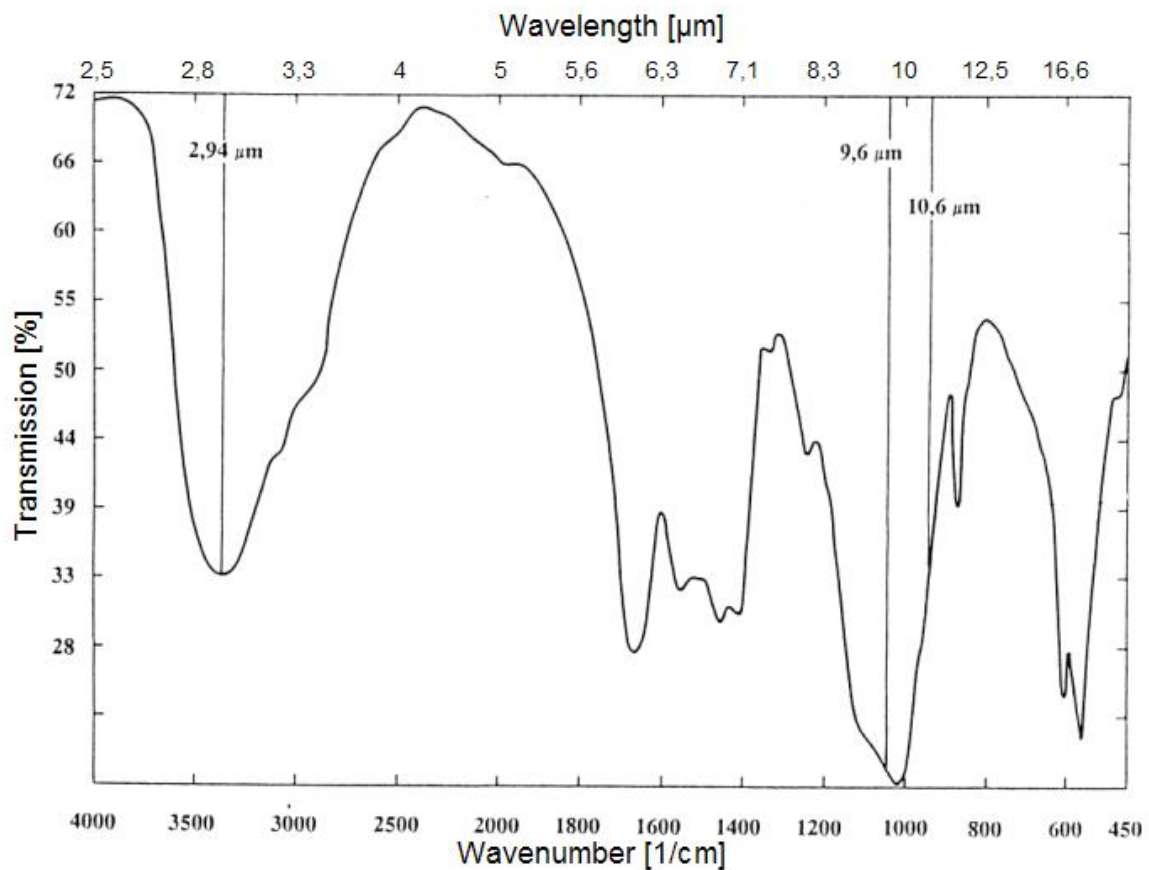
Figure 2.5: Absorption properties of human cortical femur bone (after [Kar92])

Forrer et al [For93] have collected data of the absorption coefficients for the three particular bone components at CO_2 and Er:YAG laser wavelengths. This data is summarised in table 2.2.

Table 2.2: Absorption coefficients of the particular bone components found in the literature [For93]

Absorption coefficient of the particular component μ_{ai} [1/cm]	Relative appearance [weight%]	Wavelength [µm]				
		2.94	9.3	9.6	10.3	10.6
Collagen	27	1330	502	556	212	222
Water	13	11850	554	577	709	817
Minerals	60	648	5200	5494	4572	3475

With the knowledge of the absorption coefficients μ_i, the mass density of the particular components ρ_i and their weight proportion x_i, it is possible to estimate the absorption coefficient μ_a of the compound material bone, dentin, and enamel with the mass density ρ of the composite with the following formula [Iva05]:

$$\mu_a = \rho(\mu_{HA}x_{HA}/\rho_{HA} + \mu_{H_2O}x_{H_2O}/\rho_{H_2O} + \mu_{Coll}x_{Coll}/\rho_{Coll} + \mu_{Lip}x_{Lip}/\rho_{Lip}) \quad (2.6)$$

The values for the calculated absorption coefficients for cortical and cancellous bone, dentin and enamel are summarised in table 2.3.

Table 2.3: Calculated absorption coefficients [Iva05, PC], weight proportions according to [Duc90]

Calc. absorption coefficient [1/cm]	Wavelength [µm]			Weight proportion [%]			
	2.94	9.6	10.6	Water	Mineral	Collagen	Lipid
Cortical bone	3800	2250	1500	13.5	60	25.5	1
Cancellous bone	5900	1300	970	30.5	34	34	1.5
Dentin	4640	2610	1770	16.7	67.8	15.5	0
Enamel	2170	4470	3080	4.5	95	0.5	0

3 Overview of Laser Hard Tissue Ablation

Almost immediately after the first report on a working laser was published by Maiman in 1960 [Mai60], lasers were tested for use in medical applications like tissue coagulation, vaporisation, and ablation. Various laser types have been used on almost all kinds of tissues for different therapeutic and diagnostic purposes. Laser tissue interaction can generally be divided into five categories: photochemical interaction, thermal interaction including thermo-mechanical ablation, photoablation, plasma-induced ablation, and photodisruption [Nie96].

The photochemical interaction, mainly used in photodynamic therapy, needs a photosensitiser which reacts chemically under laser irradiation. This causes the desired effect in the tissue, usually a cell toxic effect that kills cancer cells. Wavelengths in the red visible region to near infrared (diode or dye lasers) are used due to the high optical penetration depth of these wavelengths in soft tissue. The duration of the laser pulses begins at about one second to cw laser action. Usually low irradiances are used.

In thermal interaction, it is essential to achieve a certain temperature at which the desired effect (coagulation, vaporisation, ablation, etc.) takes place. The laser energy is deposited in the tissue and transformed into heat which drives the actual process. As a result, laser types of which radiation is strongly absorbed in the concerning tissue are used in this case. These are CO_2 lasers or solid-state lasers such as Nd:, Er:, and Ho:YAG laser. Pulse durations from about 1 µs up to cw are used and irradiances are up to the MW/cm^2 range. The thermal interaction process

will be discussed in much more detail in chapter 3.2, which has the hard tissue ablation mechanism as special subject.

For photoablation, high photon energies are necessary as the process is based on the direct breaking of molecular bonds. Therefore, excimer lasers in the UV range (ArF, XeCl, etc.) are used with short pulse durations between 10 to 100 ns and resulting high irradiances of 10^7 to 10^{10} W/cm^2. This process will also be discussed briefly in chapter 3.2 since studies on hard tissue ablation with excimer lasers have been carried out as well.

By increasing the irradiance to values of above 10^{11} W/cm^2, optical breakdown in solids and liquids occurs. This results in avalanche material ionisation and formation of plasma. Optical breakdown enables the energy deposition not only in strongly absorbing tissue but also in weakly absorbing media. For this interaction mechanism with tissue, short pulsed solid state lasers like the Nd:YAG, Nd:YLF, and Ti:Sapphire with pulse durations between 100 fs and 500 ps and resulting irradiances between 10^{11} to 10^{13} W/cm^2 are used.

When the irradiance is increased even further to values of up to 10^{16} W/cm^2, photodisruption sets in. In this case the effects associated with optical breakdown, are plasma formation and shock wave generation. If the optical breakdown takes place inside a (soft) tissue or fluid, cavitation and jet formation can also take place. The tissue is fragmented or ablated by the resulting mechanical effects. Due to the mechanical nature of the process, the term disruption (photodisruption) is chosen.

In the first part of this chapter (3.1) an overview of the current status of research on hard tissue ablation with different laser types will be given. In the second part (3.2), the so-called thermo-mechanical ablation mechanism for infrared lasers will be explained in more detail.

3.1 Different Laser Systems for Hard Tissue Ablation

The laser systems for which applications in the field of hard tissue ablation are reported can be roughly divided into three categories.

The first group consists of various mid IR lasers, foremost the CO_2 laser (9.6/10.6 µm) [For93, Mey96, Iva98, Fre03, Iva05, Iva05b] and the Er:YAG/YSGG laser (2.94/2.79 µm) [Zah97, El M 97, Ape02, Sas02]. Other laser systems in the mid IR spectral range have also been used, but to a much lesser extent, e.g. the Ho:YAG laser (2.12 µm) [Bar97, Won00], the hydrogen fluoride laser (2.71, 2.83, 2.91 µm) [Iza90b], and free electron lasers (tuneable wavelength) [Spe99, Pea99]. The interaction mechanism of IR laser radiation with (hard) tissue is a thermally induced process. If the necessary conditions are met, effective and sparing thermo-mechanical ablation can take place.

The second group of laser systems for hard tissue ablation are UV radiation emitting excimer lasers, e.g. the XeCl laser (0.308 µm) [Mur04, Jah92 Yow89] and the ArF laser (0.193 µm) [Lus91, Lus92, Nak99]. A general postulate often found in the literature is that a direct photoablation due to dissociation of organic molecules takes place in this case. However especially for the longer excimer wavelength (XeCl @ 0.308 µm), there is a considerable thermal component in the ablation process. Sanchez et al. [San97] also report thermal interaction with surface melting for higher radiant exposures (>1.5 J/cm^2) with an ArF excimer laser at 0.193 µm on dentin.

The last group consists of "ultra-short" pulsed laser systems (ps or fs pulse duration) [Nie94, Nee96, Arm02]. In this case, the wavelength is not important since plasma-induced ablation or photodisruption takes place due to the high irradiances.

3.1.1 Hard Tissue Ablation with UV Lasers

Clean and very precise ablation of hard tissue with only minimal thermal damage to the surrounding tissue can be achieved with UV radiation emitting excimer lasers. Due to the athermal nature of photoablation for the short wavelength of the ArF laser (0.193 mm) and the strong absorption in collagen for all excimer laser wavelengths, a large heating of the remaining surrounding tissue can be prevented. Furthermore, because of the low absorption in water and their transmissibility through standard quartz optical fibres, the ablation with excimer lasers is often done under water, which prevents tissue parching and offers optimal cooling. However, ablation rates of hard tissue with UV lasers are very low. Difficulties in handling, especially in clinical environments, arise from the necessary use of halogen gases (chlorine, fluorine). The ablation rates reported in the literature for XeCl and ArF excimer lasers are all in the region of 1 - 3 µm per pulse or even below [Lus91, Nak99, Mur04, Dre91, Jah92]. Yow et al. [Yow89] presented cut depths of just below 2 mm with high radiant exposures of a longer pulsed (120 ns) XeCl laser in rabbit bones with a thermal damage zone of only 2 – 3 µm. Murray et al. [Mur04] reached ablation rates of almost 2 µm/pulse at radiant exposures of 14 J/cm^2/pulse in dentin with a 200 ns pulsed XeCl laser. Especially for the short wavelength ArF excimer laser (0.193 µm), a very small thermal damage zone of below 1 µm [Lus91] or one that is not even detectable [Nak99] are reported. However, bone damage represented by osteocyte destruction presumably caused by photo-acoustic waves in a region of up to 1.45 mm from the irradiated site was found by Lustmann et al. [Lus92]. Recently, some studies of hard tissue ablation with alternative UV laser sources like the frequency tripled Nd:YAG laser at 0.355 µm have been conducted [Del04, She04]. Dela Rosa et al. [Del04] used a short pulsed (5 ns) frequency tripled q-switched Nd:YAG laser for ablation of bone and produced incisions of a maximal depth of 0.43 mm at a radiant exposures of 50 J/cm^2/pulse. No thermal damage could be detected with polarised light microscopy of 100 µm thick slices. However severe mechanical damage (cracking) set in at radiant exposures above 5 to 10 J/cm^2/pulse. This effect was even more pronounced with the additional use of a water spray.

To summarise the data found in regard to UV (mainly excimer) laser ablation of hard tissue, it can be said that clean ablation with very small thermal damage is possible. However, the ablation efficiency is much too low for any practical use on hard tissue, moreover, mechanical alterations of the surrounding tissue due to photo-acoustic effects from the short pulse interactions cannot be ruled out.

3.1.2 Hard Tissue Ablation with Ultra-Short Pulsed Lasers (ps / fs)

In recent time, the wider availability of ultra-short pulsed laser systems in the ps and fs range has encouraged research of hard tissue ablation with these systems. The advantage of these laser systems is the complete absence of thermal damage due to the completely athermal interaction mechanism with the tissue, which is plasma induced ablation or photodisruption. As a wavelength matching the material absorption is not necessary for the interaction, the "usual" ultra short pulsed laser types as the Ti:Sapphire (fs range) and the Nd:YLF (ps range) can be used. Niemz has achieved quite promising results for cavity preparation in dentistry with a Nd:YLF laser (30 ps pulse duration). However, the ablation rate is still quite low (10 µm/pulse at 8.2 mJ pulse energy for healthy dentin and 3 µm/pulse at 10 mJ pulse energy for healthy enamel) [Nie94, Nie96 (chapter 4.2)], and the systems are still much more complex and expensive than Er:YAG or CO_2 lasers which can also be used for this purpose. Armstrong et al. [Arm02] ablated incus and stapes bones (ossicle bones in the middle ear) with 350 fs pulses from a 1.053 µm chirped pulse amplifier Ti:Sapphire laser system at a repetition rate of 10 Hz. At a radiant exposure of 2 J/cm^2/pulse and a beam diameter of 0.4 mm, a precisely reproducible ablation rate of 1.26 µm/pulse could be achieved. Scanning electron images revealed no thermal damage and only minimal mechanical damage from expanding gases. Ultra-short laser pulses could offer a possibility for high precision laser ablation of minimal bone volumes as it is needed for example for a stapedotomy in

the treatment for otosclerosis. However, this will not be a feasible alternative for larger bone volumes in the near future.

3.1.3 Hard Tissue Ablation with Infrared Lasers

The first reports on hard tissue processing with lasers were already presented in 1964 when dental enamel was vaporised with ruby laser pulses [Ste64]. (With a wavelength of 0.694 µm the ruby laser is not an IR laser. However, the interaction mechanism in this case is thermal interaction the same as for the IR lasers.) During the ongoing research in the following forty years, the two most promising laser sources for hard tissue ablation in the infrared spectral region were found to be the CO_2 laser (9.6 & 10.6 µm) and the Er:YAG laser (2.94 µm) (resp. Er:YSGG laser (2.78µm)). This was mainly because of very strong absorption of their wavelength in hard tissue. In the beginning, many studies carried out with cw and long (ms) pulsed CO_2 lasers [Hor77, Ger81, Kla92]. These irradiations caused severe thermal damage to the adjacent tissue with charring and carbonisation. During in-vivo animal experiments the thermal damage led to delayed healing compared to conventional mechanical osteotomies. During this stage of development, the achieved results did not indicate a possibility to apply laser technology to osteotomies in human patients.

However, since the end of the 1980ies several comprehensive studies with different shorter pulsed laser system (µs range) have been carried out [Nus88, Hib89, Wal89, Yow89, Cla89, Nel89, Wal91, Hib92, For93]. The results of these studies showed that, with strongly absorbed laser wavelengths and pulse durations below the thermal relaxation time, hard tissue ablation is possible with acceptable thermal damage zones. Especially good results in hard tissue ablation indicated by small thermal damage zones and high ablation efficiency were achieved with short pulses (µs to ns range) of Er:YAG, Er:YSGG, and CO_2 lasers in combination with an additional water replacement during the laser irradiation, e.g. in form of a fine water spray [Ert93, Vis96, Mey96, Whi00, Fri01, Fri02, Ape02, Wig 02, Mül02, Fre03,

Iva98, Iva00b, Iva02, Afi03, Iva05, Iva05b, Iva05c]. Ivanenko and Hering (in co-operation with different co-workers) have achieved incisions in compact bone with extremely small thermal damage to the adjacent tissue with different pulsed CO_2 laser systems at 9.6 and 10.6 µm. Ivanenko, Hering et al. [Iva02] report on an extremely narrow thermally altered layer of between 2 and 6 µm at the border of incisions of 1 to 5 mm depth in cortical bovine bone with sub-µs pulses of a mechanically q-switched CO_2 Laser (300 ns FWHM, 9 J/cm^2/pulse). Frentzen, Ivanenko, Hering et al. [Fre03] present ex-vivo laser irradiations of pig ribs and porcine cortical bone with a RF excited slab CO_2 laser with 80 µs pulse duration and with a radiant exposure of 360 J/cm^2/pulse at the irradiation site. Thermal damage zones at the border of the incisions with a width of under 10 µm were identified. First in-vivo experiments on canine mandibles with a similar laser system [Iva05b, v.Hän03] have shown that effective CO_2 laser osteotomy without aggravating thermal side effects and without healing delay is possible when using the multi-pass irradiation technique and water spray (further described in chapters 3.2 and 4 of this thesis).

3.2 Ablation Mechanisms

In this chapter, the mechanisms of hard tissue ablation will be discussed. Most of the chapter will be assigned to the thermo-mechanical ablation model for CO_2 lasers (9.6 and 10.6 µm). However the considerations are generally valid for other IR lasers like the Er:YAG (2.94 µm), Er:YSSG (2.79 µm), or free electron lasers (2.1 - 9.8 µm). The thermo-mechanical ablation is basically a thermal interaction since the laser energy is absorbed in the tissue and transferred into heat energy which heats tissue components like water or collagen, depending on the laser wavelength. This process happens extremely fast and results in a high pressure build-up which triggers fragmentation and ejection of the hard tissue fragments [Wil01, For93, Iza90].

In the case of UV laser radiation, the ablation mechanism is usually described as photoablation or direct photoablation. This means the laser photons have enough

energy to break molecular bonds i.e. the photon energy is high enough to create repulsive states in which the molecule breaks apart, thus causing tissue ablation. UV radiation is strongly absorbed in bio-molecules like proteins, for example collagen in bone. However, this term is not well defined. Customarily it is used for precise ablation caused by UV photons. At least the photons of the ArF excimer laser (λ = 0.193 µm; E_{photon} = 6.4 eV) reach energies which can dissociate macromolecules [Hib97]. It is assumed that significant material ablation takes place when a critical density of broken molecular bonds is reached; this leads to a threshold value for the absorbed laser energy per volume [Jel84]. Generally, it is believed that the ejected particles carry away much of the energy deposited in the tissue. However, the part of the energy below the threshold of ablation remains in the tissue as heat which can cause significant thermal damage when applying UV laser pulses to weakly absorbing tissues or using high pulse repetition rates. Moreover, the process is not pure photoablation unless the short wavelength of 0.193 µm of the ArF laser is used. Especially for the longer UV wavelengths, there is a considerable thermal component of the tissue ablation. In [Sut86] the authors even propose a pure thermal interaction for ablation of PMMA with a XeCl excimer laser at 0.308 µm. In chapter 6.1 measurements of compact bone tissue ablation with a XeCl excimer laser (λ = 0.308 mm) will be presented.

The rest of this chapter will deal exclusively with the thermo-mechanical ablation model for IR lasers.

3.2.1 Water Driven Thermo-Mechanical Ablation

Infrared lasers are used for hard tissue ablation because of their very strong absorption in the tissue, as it is explained in chapter 2.3.3 (see table 2.3). A high absorption coefficient guarantees light absorption in a very thin layer at the surface of the tissue. The penetration depth $d = 1/\mu_a$ (equation 2.5) for cortical bone is only 3 µm for Er:YAG laser radiation at 2.94 µm. For CO_2 laser radiation at wavelengths of

9.6 μm and 10.6 μm the penetration depth amounts to 4 μm and 7 μm, respectively. In this layer a very fast conversion of the absorbed light energy into heat takes place. The liquid (mainly water) confined in this tissue layer is vaporised. This leads to a rapid internal pressure build-up, which surmounts the ultimate tensile strength. This finally breaks the microscopic bone structures apart thus leading to ejection of the solid tissue components in form of micro-particles. The time scale for the start of the ablation process is usually shorter than the pulse length. So, the ablation front proceeds deeper into the tissue during the laser pulse. Thus, it is possible to achieve higher ablation depths per pulse δD than the penetration depths of the laser wavelength, especially for longer laser pulses (80 - 225 μs) [Mit02, Afi04, Iva05]. The high absorption at the CO_2 laser wavelength of 9.6 and 10.6 μm is mainly due to absorption in the mineral component. However, the absorption in water is also strong at this wavelength (see table 2.2). So, for the CO_2 lasers used in the presented studies, both strong direct absorption in water and fast heat transfer from the hydroxyapatite to the water in the bone causes the "water-micro-explosions" which enable effective and "clean" ablation of hard tissue. Contrarily, the absorption of the Er:YAG laser radiation at 2.94 μm is mainly linked directly to strong absorption in water and at a lesser extend to the mineral component. Because of this the model for hard tissue ablation through water micro-explosion was originally postulated for the Er:YAG laser by various authors (see for example [Wal91, Hib93]) and was later adopted to CO_2 lasers by Forrer et al. [For93] and Ivanenko et al. [Iva98].

For the ablation process to be effective and sparing for the surrounding tissue, a fast energy deposition is obviously required. It is necessary to guarantee that the internal pressure build-up is faster than the heat diffusion. Only in this case will the main part of the deposited energy be used for the ablation itself and the heat will leave the tissue together with the ejected tissue particles (debris) and vapour. It is obvious that the ablation efficiency directly influences the thermal side effects. For an effective ablation process, the following prerequisites have to be achieved. A well-localised energy deposition due to strong absorption in the irradiated tissue is needed. This energy deposition should take place on a time scale, which is shorter

than for the thermal diffusion. Additionally a sufficient quantity of "driving" material is necessary for the micro-explosions, i.e. enough tissue water.

3.2.2 Thermal Relaxation Time

The parameter which characterises the time scale of the heat diffusion into the tissue after laser induced heating is the thermal relaxation time τ_{therm}. In the literature it is sometimes defined in different ways. The definition found most often [Nie96, Cho01, McK90] is:

$$\tau_{therm} = \frac{1}{4\chi\mu_a^2} \qquad\qquad (3.1)$$

This term can be derived from the solution of the following equation for the heat diffusion in solid mediums [Car59, Cho01]:

$$\nabla^2 T - \frac{1}{\chi}\frac{\partial T}{\partial t} + \frac{q_{gen}}{k} = 0 \qquad\qquad (3.2a)$$

$$\frac{\partial^2 T}{\partial z^2} - \frac{1}{\chi}\frac{\partial T}{\partial t} + \frac{q_{gen}}{k} = 0 \qquad \text{(one dimensional)} \quad (3.2b)$$

T is the temperature at time t and depth z, χ the thermal diffusivity (cm^2/s), k the thermal conductivity (W/(cm·K)), and q_{gen} the heat (laser) source term (W/cm^3). This differential equation can be solved analytically for an infinitely thin heat source Q_S (J/m^2) covering the material surface (an idealised conception for a tissue heated superficially with a laser pulse) [McK90]:

$$T(z,t) = \frac{Q_S}{2\rho c\sqrt{\pi\chi t}}e^{\frac{-z^2}{4\chi t}} \qquad\qquad (3.3)$$

ρ is the mass density (g/cm^3). The thermal penetration depth z_{therm} can now be defined as the depth where the exponential term in equation (3.3) has the value -1 [Nie96, Sch92]:

$$z_{therm} = \sqrt{4\chi t} \qquad\qquad (3.4)$$

The thermal penetration depth is the depth in which the temperature T has decreased to 1/e of its initial peak value at the surface.

The thermal relaxation time τ_{therm} is according to [Wol71] the time for which the optical penetration depth $d = 1/\mu_a$ (equation 2.5) equals the thermal penetration depth z_{therm}. This gives the following equation for the thermal relaxation time:

$$z_{therm} = d \Rightarrow \sqrt{4\chi\tau_{therm}} = \frac{1}{\mu_a} \Leftrightarrow \tau_{therm} = \frac{1}{4\chi\mu_a^2} \qquad (3.5)$$

Despite its name, it has to be mentioned that the thermal relaxation time is not the time in which the temperature has decreased to 1/e of its initial value; the temporal progression of the temperature distribution (eq. 3.3) does not have the form $T \sim exp\ (-t/\tau_{therm})$.

In case one single laser pulse with a duration τ_L shorter than the thermal relaxation time τ_{therm} ($\tau_L < \tau_{therm}$), impinges on the material, the depth to which considerable heat can diffuse during the pulse action is even shorter than the thermal penetration depth. Thermal damage to optically non effected tissue is negligible during the pulse (but not necessarily after the pulse). For laser pulse durations longer than the relaxation time ($\tau_L > \tau_{therm}$), heat can diffuse to areas where the tissue is not reached by the laser radiation and thermal damage to adjacent tissue is already possible during the laser action. Due to the dependence of the optical penetration depth on the absorption coefficient μ_a the thermal relaxation time becomes proportional to $\tau_{therm} \sim \mu_a^{-2}$ and is dependent on the wavelength. As a result, the thermal relaxation time is the shortest at the wavelength where absorption is the strongest. Stronger absorption leads to steeper temperature gradients and, with that, to faster heat diffusion. With the values for the thermal properties of compact bone from table 2.1 ([Duc90] $\chi \approx 0.002$ cm^2/s) and the absorption coefficients for compact bone at different wavelengths from table 2.3 (μ_a = 3800 cm^{-1} @ λ = 2.94 µm; μ_a = 2250 cm^{-1} @ λ = 9.6 µm; μ_a = 1500 cm^{-1} @ λ = 10.6 µm), the thermal relaxation time can be estimated for the different wavelengths to be approximately 9 µs for λ = 2.94 µm, 25 µs for λ = 9.6 µm and 55 µs for λ = 10.6 µm. (These values are only estimations due to the variation in the material constants of bone tissue. In [Iva05] the values estimated for the three thermal relaxation times from the literature material constants are 7 µs, 20 µs, and 45 µs for 2.94, 9.6, and 10.6 µm, respectively.)

The thermal relaxation time is only a scale parameter defined in a special way which gives an estimate of the time required for heat to conduct away from a laser-heated tissue region after application of an instantaneous heat source. In the case of an irradiation with repetitive laser pulses, as it would be necessary for most applications in medicine, a thermal accumulation of the heating takes place even if the time between two pulses is considerably longer than the thermal relaxation time [Jan93, Cho01]. These results indicate that complete thermal relaxation of tissue to the initial temperature before the laser induced heating is a relatively slow process and takes place in time scales longer than the defined thermal relaxation time. Choi and Welch [Cho01] have calculated effective relaxation times τ_{eff}, which are the times required for the maximal temperature after laser-heating T_{peak} to decrease to values just above the original baseline temperature. For the calculation of the temperature development with time, they have used a one-dimensional analytical solution for equation (3.2b), with an initial temperature distribution that is proportional to $exp(-\mu_a z)$, corresponding to the light absorption in the tissue (Lambert-Beer law). Also one- and two-dimensional numerical models were applied in the work. For the one-dimensional case the calculated τ_{eff} times agreed with in 1 % between the analytical and the numerical model. The study showed that this effective relaxation time was considerably larger than the thermal relaxation times calculated with the conventional model, according to equation (3.1).

In figure 3.1 the temporal evolution of the temperature at the tissue surface (*z = 0*) for irradiation of compact bone tissue with a CO_2 laser in the one dimensional case calculated according to the two existing models [McK90, Cho01] is depicted. The temperature development for the laser wavelengths 9.6 and 10.6 µm is calculated according to Choi and Welch's model where the heat is initially distributed corresponding to the light absorption governed by the Lambert-Beer law [Cho01]. In case that the initial heat distribution is assumed to be an infinitely thin layer on the bone surface the temporal change of the surface temperature is calculated with equation 3.3 according to McKenzie [McK90].
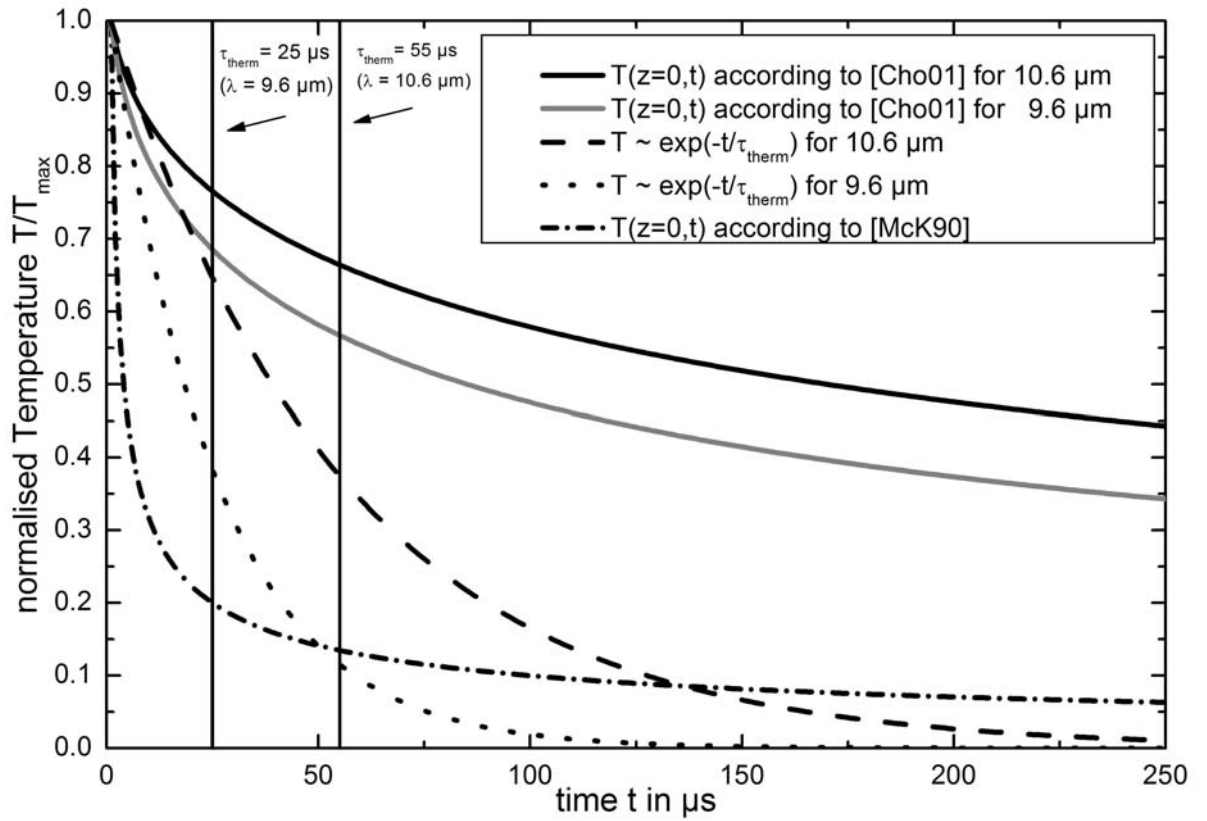
Figure 3.1: Temporal evolution of the surface temperature (z=0) calculated with the one dimensional models from literature. Straight lines: initial heat distribution according to light absorption (according to [Cho01]) black (——) for 10.6 μm and grey (——) for 9.6 μm; (•---•): initial heat distribution only on the surface (eq. 3.3 for z = 0 from [McK90]); exponential decay $\sim exp(\tau_{therm}/t)$ (- - -) for 10.6 μm and (•••) for 9.6 μm.

As can be seen in figure 3.1, the time scale for complete temperature decrease to the baseline temperature is, in fact, remarkably longer than the thermal relaxation time. However, it has to be considered that the equations for the temperature evolution are based on a static model where no heat is removed by convection or, what is much more important in the case of tissue ablation, with heated ejection particles in the ablation debris. The initial fast temperature decrease at the time scale of about 10 μs is however, quite well described by the thermal relaxation time constant. Therefore, it can be used to estimate the competition of light induced tissue heating and heat diffusion into adjacent tissue areas, at least during the initial pre-ablative stage.

3.2.3 Threshold for Radiant Exposure and Irradiance

To describe the prerequisites for effective clean hard tissue ablation with infrared lasers, Hibst [Hib97] introduced a model with two thresholds for the thermo-mechanical ablation process. There is a threshold for the radiant exposure Φ_{th} and for the irradiance I_{th}. The threshold for the radiant exposure corresponds to the heat of ablation (minimal specific ablation energy) H_{abl} (J/mm^3) which is needed to initiate the ablation process, multiplied by the depth of the light absorption i.e. the optical penetration depth $d = 1/\mu_a$.

$$\Phi_{th} = H_{abl} \cdot d = \frac{H_{abl}}{\mu_a} \qquad\qquad (3.6)$$

According to estimations found in the literature [For93, Iva05], the value for the heat of ablation for bone is about H_{abl} = 1.2 to 1.4 J/mm^3. The calculated ablation threshold for radiant exposure for compact bone with a 9.6 µm CO_2 laser derived from equation (3.6) with the corresponding absorption coefficient from table 2.3 gives values in the range from Φ_{th} = 0.53 to 0.62 J/cm^2. The calculated value for the threshold lies below the data we collected in our group on the radiant exposure threshold, for ablation of compact bone tissue with a CO_2 laser at 9.6 µm wavelength. Our measurements gave values of Φ_{th} = 0.7 J/cm^2 for a pulse duration of τ_{FWHM} = 45 ns and Φ_{th} = 1.6 J/cm^2 for a pulse duration of τ_{FWHM} = 225 µs [Iva05, Afi04]. The lowest measured threshold value of 0.7 J/cm^2 corresponds to a heat of ablation value slightly below 1.6 J/mm^3.

The threshold for the irradiance I_{th} reflects the competition between the velocity of energy deposition in the tissue and the loss of heat from the ablation volume by heat diffusion in surrounding tissue areas. As already discussed above, the thermal relaxation time can be used as a time constant for the initial phase of the ablation process, so the irradiance threshold may therefore be described as:

$$I_{th} = \frac{\Phi_{th}}{\tau_{therm}} \qquad\qquad (3.7)$$

With equation (3.1) and (3.6) the irradiance threshold I_{th} can be written as:

$$I_{th} = 4H_{abl}\chi\mu_a \qquad\qquad (3.8)$$

From equation (3.6) and equation (3.8) follows that for effective and thermally sparing ablation the following two conditions have to be fulfilled by the radiant exposure of the laser pulse with duration τ_L.

Radiant exposure threshold: $\Phi \gg \Phi_{th} = \dfrac{H_{abl}}{\mu_a}$ (3.9)

Irradiance threshold: $\Phi \gg I_{th}\tau_L = \dfrac{\Phi_{th}}{\tau_{therm}}\tau_L = 4H_{abl}\chi\mu_a\tau_L$ (3.10)

It is necessary to fulfil both conditions at the same time for effective and clean ablation. Short pulses with high pulse energy are essential for good results. It is also noteworthy to state that both conditions depend on the absorption coefficient μ_a in the opposite way. The radiant exposure threshold decreases with increasing absorption due to stronger energy concentration in a thinner tissue layer. The irradiance threshold increases with increasing absorption in the tissue due to steeper heat gradients resulting in faster heat diffusion.

3.3 Summary Chapter 3

In this chapter the current state of the research on hard tissue ablation with different laser systems was presented. Ablation rates and biological compatibility of the different systems were compared. It was pointed out that the best suited laser systems for hard tissue processing are pulsed Er:YAG and the CO_2 lasers due to their strong absorption in hard biological tissue. In the second part of the chapter the thermo-mechanical ablation mechanism for IR lasers, which is based on the fast laser-induced pressure build-up during the evaporation of the tissue water, was described. The time scaling parameter for the thermal diffusion the thermal relaxation time was introduced. For effective thermo-mechanical ablation of hard tissue the thresholds for radiant exposure and irradiance have to be exceeded and a sufficient water content of the tissue is necessary to effectively drive the ablation process.

4 Methods

4.1 Laser Sources and Irradiation Set-Ups

4.1.1 Laser Sources

For the experiments described in this thesis two different CO_2 laser systems are mainly deployed. The first system is a TEA CO_2 laser (<u>t</u>ransversely <u>e</u>xcited <u>a</u>tmospheric pressure) with sub-µs pulse duration (model "MTL 3 GT" from Edinburgh Instruments). A diffraction grating acts as one of the resonator mirrors in this system. Therefore the wavelength of this laser system is tuneable between 9.2 to 10.7 µm. The temporal pulse shape, shown in figure 4.1, consists of a short peak with a duration of about τ_{FWHM} = 45 ns (<u>f</u>ull <u>w</u>idth at <u>h</u>alf <u>m</u>aximum) and a pulse tail with a duration of about 900 ns. The complete pulse is about 1 µs long.
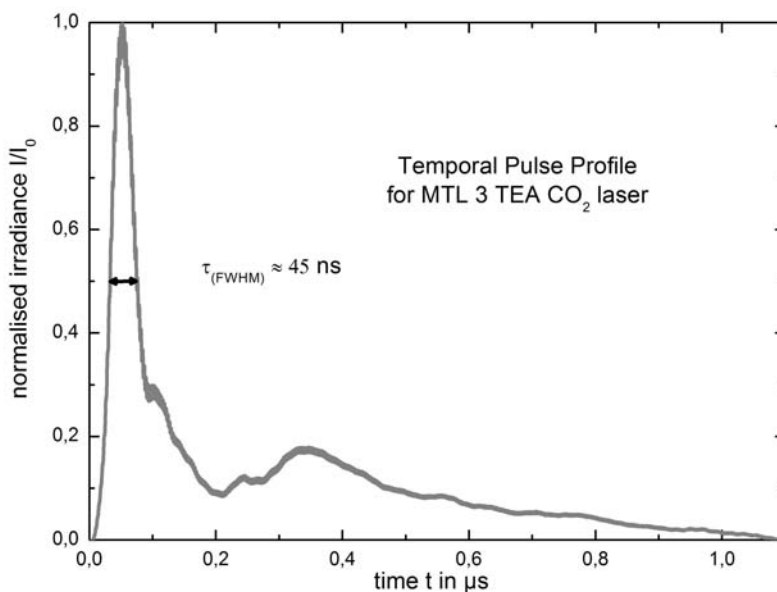

Figure 4.1: Temporal pulse profile TEA CO_2 laser (MTL 3), $\tau_{FWHM} \approx$ 45 ns

The pulse energy can be varied with the laser discharge voltage. The pulse energies used for the experiments were between 30 and 40 mJ. Pulse repetition rates of up to 100 Hz can be realised, but only repetition rates of up to 50 Hz were employed in the experiments presented here. A mode filter is installed in the resonator of the TEA laser. As a result the laser emits a single basic mode TEM_{00} and has a nearly Gaussian beam profile. The M^2 beam quality factor is around 1.26, which gives the laser a good focusability. The focussing parameters will be given individually for each experiment presented in this thesis. The TEA CO_2 laser was utilised mainly for the laboratory experiments on the ablation mechanism and on the temperature measurements, described in chapter 5.

The second laser system used for the studies presented in this thesis is a RF excited diffusion-cooled CO_2 slab laser system. The slab concept for CO_2 lasers has been increasingly utilised in recent years to realise reliable and convenient laser systems for technical and industrial tasks [v.B05, Mar05]. Our group uses a Rofin Sinar SC x 30 slab CO_2 laser. The pulse duration of this system can be chosen from τ_{FWHM} = 5 to 400 µs. In the experiments presented here laser pulses with a duration of τ_{FWHM} = 80 µs were applied on hard bone tissue. The pulse duration of 80 µs was chosen, since a trade off between short pulse duration and high pulse energy has to be found for optimal ablation results. Laser pulses below 80 µs have disproportionately low pulse energies because of a pulse rising time of 40 - 50 µs (figure 4.2). So no shorter pulse durations could be applied without loss of peak pulse power and the resulting loss of the ablation efficiency. On the other hand, pulse durations that are as short as possible should be used to minimise thermal damage. Thus, the shortest pulse duration of 80 µs, which allows the full exploitation of the potential of the slab laser, was used. The pulse energy amounts to 80 - 90 mJ for this duration. To some extent, the pulse energy depends on the temperature of cooling water and on the pulse repetition frequency, which can be increased up to several tens of kHz but is limited by a maximal duty cycle value of 0.5 (duty cycle = pulse duration · repetition rate). The experiments with the slab CO_2 laser presented in this thesis were conducted at 200 Hz unless stated else. The spectrum of the slab CO_2 laser system consists almost entirely of the 10P18 CO_2 laser line at 10.57 µm

with only minimal parts of other neighbouring laser lines. The wavelength of the slab CO_2 laser is not tuneable. Due to the slab geometry of the exciting electrodes, which give this laser type its name, the original laser beam propagates differently in the X- (free propagation) and Y-direction (waveguide propagation). After the resonator, a considerable effort in beam shaping with cylindrical optical elements and spatial filtering is necessary to obtain a single TEM_{00} mode beam with a Gaussian radial beam profile at the output. The beam quality factor M^2 of the output beam is between 1.2 and 1.29, which gives the laser a good focusability. A typical temporal pulse profile of the RS SC x 30 laser with τ_{FWHM} = 80 µs is shown in figure 4.2.
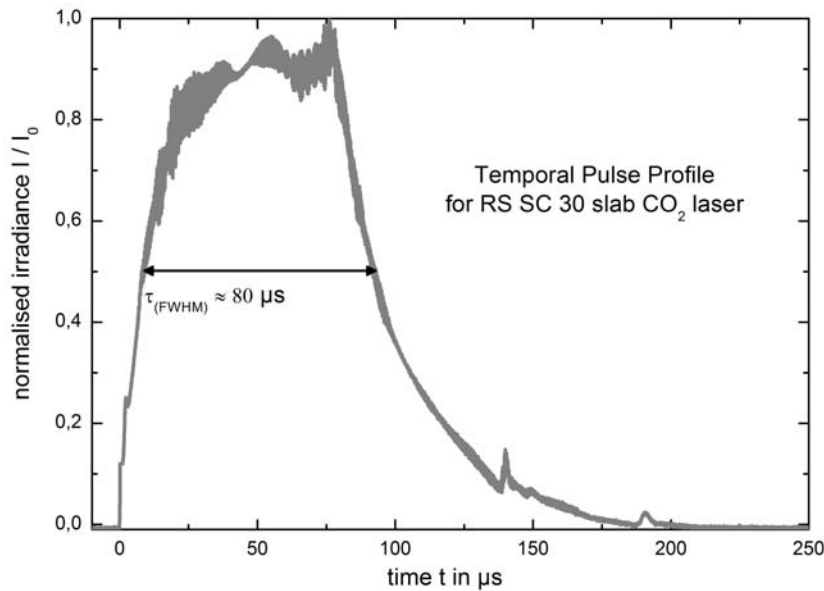
Figure 4.2: Temporal pulse profile slab CO_2 laser (RS SC x 30), $\tau_{FWHM} \approx 80$ µs

A very detailed description on CO_2 lasers in general can be found in the book of Witteman [Wit87]. The thesis of Dr. Said Afilal [Afi04] gives detailed information about the specific models used in our research group.

4.1.2 Irradiation Set-Ups

Two basically different set-ups were used for ablation experiments with bone tissue. In one set-up the bone sample is moved through the focussed laser beam with a

precision motorised linear drive stage (OWIS Limes 150 with a DC motor). The laser beam is focussed by a lens with a focus length of F = 127 mm. For the experiments with the short pulsed TEA CO_2 laser a spherical pre-focussing mirror with a curvature radius of R = 2300 mm (F = 1150 mm) was positioned at a distance of 980 mm in front of the lens to enlarge the final focus diameter and to keep the peak irradiance below the optical breakthrough threshold. A schematic diagram of the experimental set-up with the drive stage is shown in the following figure 4.3. In this set-up, the bone sample is moved relatively to the laser beam.
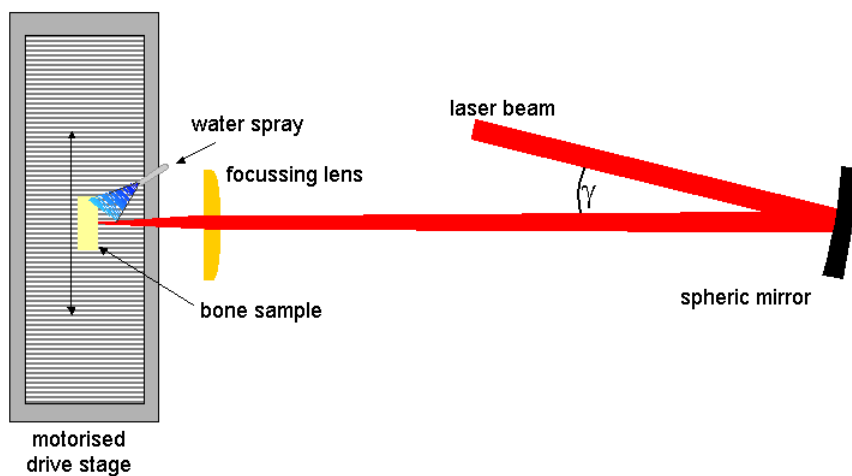
Figure 4.3: Schematic view of experimental set-up with drive stage

The second set-up incorporates a laser beam scanner. A laser beam scanner consists of three blocks of optical components: first, a telescope for adjusting the beam diameter of the incoming laser beam to the scanner aperture; second the scanning unit itself which is built out of two mirrors. These mirrors are attached to fast computer controlled galvanic drivers. With a synchronised movement of these two mirrors the laser beam can be moved along arbitrary trajectories. And third, after the scanning unit the laser beam is focussed with a plane field lens. The two scanner models that are used in our group are the Arges Elefant 20 and the Raylase Turboscan C-17. In the Raylase system the telescope is set manually to a fixed magnification value (about 1.6). In the Arges system the telescope adjustment can be done with a fast computer controlled galvanic driver. Thus, it is possible to adjust the telescope settings synchronously with the movement of the two mirrors. A variation of the distance between the two telescope lenses changes the size of the

laser beam on the flat field focusing lens. In this way the focus position and focus size behind the flat field lens can be controlled within a certain range. With this option the Elefant 20 scanner can be used for three dimensional applications or for the automatic adjustment of the focal position during laser irradiations. A schematic diagram of the experimental set-up with a laser beam scanner is shown in figure 4.4. This set-up was only used in combination with the slab CO_2 laser. In this set-up the laser beam is moved relatively to the bone sample.
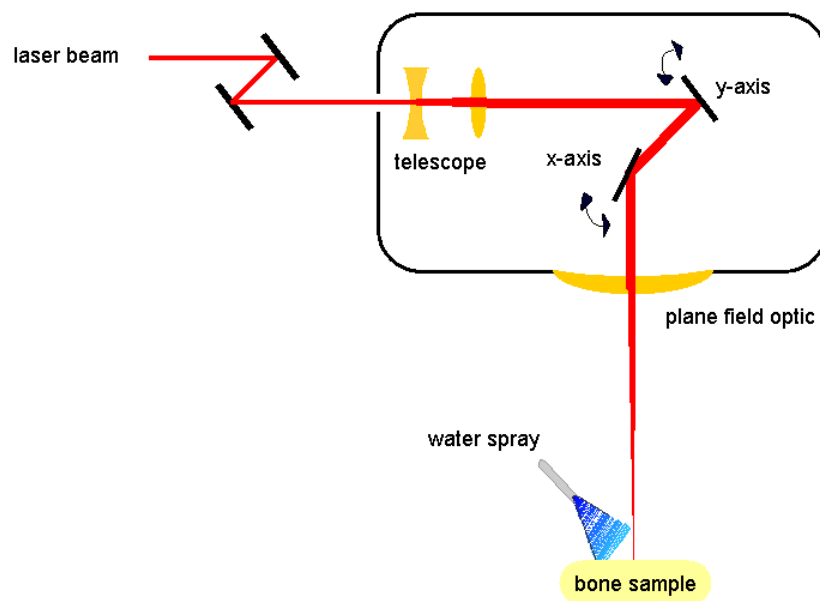
Figure 4.4: Schematic view of experimental set-up with laser beam scanner

The laser incision into the bone sample is created in a multi-pass process, where the focused laser beam is repeatedly moved over the bone sample in exactly the same way. With regard to the optical axis, the focus is positioned on the bone surface. An important part of both set-ups is a fine water spray, which is applied continuously during the laser irradiation. The water spray is directed towards the ablation spot on the bone sample. The flow rate of the water reaches values of up to 20 ml/min for the slab CO_2 laser system, but it is lower for the TEA CO_2 laser which has a lower average power. Due to the low water aerosol density, the loss of laser energy in the spray does not exceed 3%. The water spray is mainly used to prevent tissue parching during ablation. A sufficient water content in the bone tissue is essential for an effective and clean ablation process. This is described in detail in

chapter 3. Another positive effect of the water spray is the cooling of the irradiated tissue. This is especially important for the irradiations at higher average powers with the slab CO_2 laser system.

4.2 Preparation and Examination of Bone Samples and Definition of Parameters

Measurements are done on cortical bone samples, which are taken from the diaphysis of bovine femur bones. The bovine femur can be easily obtained and contains a thick (1 - 1.5 cm) layer of relatively homogenous cortical bone tissue (compact bone). Rectangular bone blocks of an approximate size of 1 x 1 x 2 cm^3 are cut out with a mechanical saw (diamond band saw Proxxon MBS 230). The blocks are fixed on the drive stage or in front of the scanner. All measurements during one experimental series are preferably done with the same bone sample or with comparable samples from the same slice of the femur. During an experimental series several parallel incisions with increasing number of beam passes are created in the sample. After the laser irradiations, the bone block is cut into two parts with the mechanical saw perpendicular to the laser cuts as seen in figure 4.5.

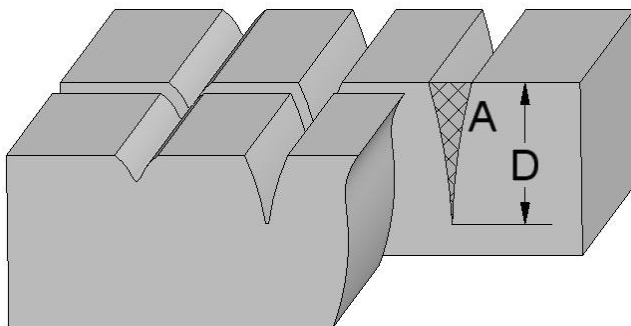**Figure 4.5:** Overview over sample preparation after laser irradiation [Iva05]

The profiles of the incisions are examined under an optical microscope (Olympus SZX 12) and digital photos are taken with a CCD camera (Spot RT). From the digital photo of the cut profile, the area *A* and the depth *D* of the cut profile, as seen in figure 4.5, can be determined with an image processing software (Adobe Photoshop).

Some parameters have to be defined to analyse the ablation results. The geometrical pulse overlap factor n is defined as:

$$n = \frac{f \cdot w_f}{v} \qquad (4.1)$$

f is the laser repetition rate, w_f is the radius of the beam focus at the $1/e^2$ level, and v is the velocity with which the bone is moved through the beam or with that the beam moves over the bone. The distance the beam focus has moved between two pulses is $\Delta x = v / f$. This means that for a pulse overlap factor $n = 1$ the shift between two pulses is one focus radius w_f. The situation for $n = 1$ is illustrated in figure 4.6. The geometrical pulse overlap factor used for experiments is usually chosen to be substantially below one ($n \ll 1$) for the slab CO_2 laser and to be around $n = 1$ for the TEA CO_2 laser.
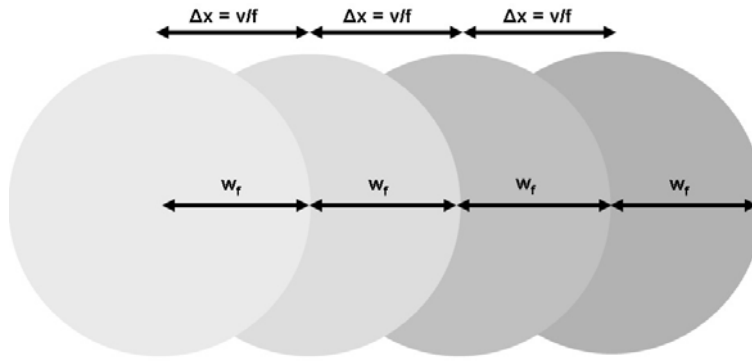
Figure 4.6: Illustration of geometrical pulse overlap factor $n = 1$. The circles indicate the laser focus diameter ($1/e^2$ level).

The equivalent pulse number N_{eq} is defined as a measure for the number of laser pulses that effectively impinge on each point of the incision, when the laser beam passes N_{pass} times over the sample.

$$N_{eq} = n \cdot N_{pass} \qquad (4.2)$$

With the equivalent pulse number the average ablation depth δD per pulse can be calculated as:

$$\delta D = \frac{D}{N_{eq}} \qquad (4.3)$$

Another important parameter for the comparison of the ablation speed for different laser systems or different focus diameters is the average cutting rate per pulse R. The rate R can be calculated without using the focus diameter w_f of the laser beam:

$$R = \frac{D \cdot L_{cut}}{N_{pulse}} = \frac{D \cdot v}{N_{pass} \cdot f} = \delta D \cdot w_f \qquad (4.4)$$

L_{cut} is the length of the laser cut and N_{pulse} is the number of applied pulses.

The specific ablation energy W_{sp} is the total energy E_{total} needed to ablate a volume V_{abl} of tissue, including all losses due to absorption in debris and heat conduction, divided by this volume:

$$W_{sp} = \frac{E_{total}}{V_{abl}} = \frac{E_{pulse} \cdot N_{pulse}}{A \cdot L_{cut}} = \frac{E_{pulse} \cdot N_{pass} \cdot f}{A \cdot v} \qquad (4.5)$$

E_{pulse} is the energy of one laser pulse. With the knowledge of the pulse energy E_{pulse}, the focus radius w_f, the radiant exposure Φ for a Gaussian beam can be calculated as:

$$\Phi = \frac{E_{pulse}}{\pi w_f^2} \qquad (4.6)$$

4.3 Comparison of Bone Tissue Ablation with Long- and Short-Pulsed CO_2 Laser Systems

The results of ablation measurements with the two different CO_2 laser systems are presented in this section to illustrate the difference in the ablation efficiency between the "short" (about 1 µs) and "long" (80 µs) laser pulses. Additional details will be considered in chapter 6.1.

In a series of laser incisions in a block of cortical bovine bone with increasing number of laser passes N_{pass}, the ablation depth per pulse δD and the specific ablation energy W_{sp} are measured for both laser systems. In figure 4.7, the ablation

depth per pulse δD for the TEA and the slab CO_2 laser are shown in dependence on the incision depth D.
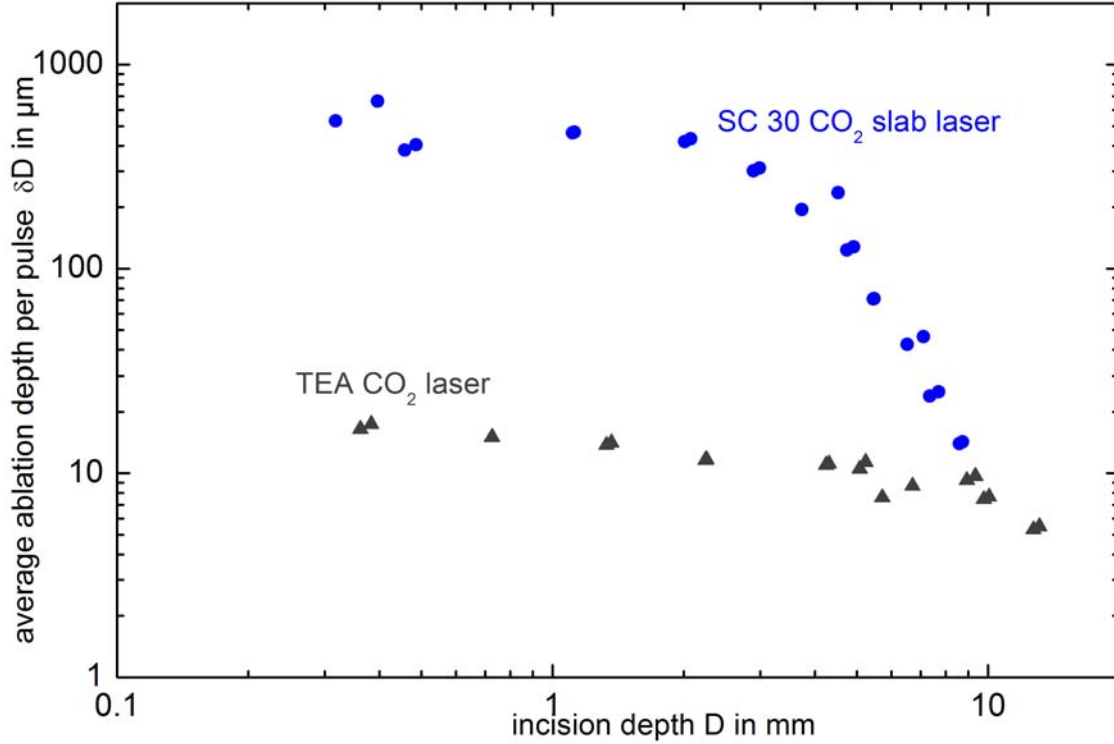
Figure 4.7: Average ablation depth per pulse δD against incision depth D for the TEA CO_2 laser (▲) (wave length λ=9.6 μm (9P22 line), τ(FWHM) = 45 ns, τ(complete) < 1μs; E_{pulse} = 41 mJ, w_f = 130 μm; Φ = 78 J/cm^2; I = 780 MW/cm^2) and the slab CO_2 laser (●) (wavelength λ = 10.6 μm (10P18 line), τ(FWHM) = 80 μs; E_{pulse} = 68.5 mJ; w_f = 60 μm; Φ = 600 J/cm^2; I = 7.5 MW/cm^2)

Figure 4.8 depicts the specific ablation energy W_{sp} in dependence on the incision depth for both laser systems. In figures 4.7 and 4.8 can be seen that the ablation efficiency decreases with increasing incision depths. This effect is quite dramatic for the longer 80 μs pulses of the slab CO_2 laser and less pronounced for the shorter (<1μs) pulses of the TEA CO_2 laser. Figure 4.7 illustrates that for incisions depths above 4 mm the ablation depth per pulse δD for the long pulsed CO_2 slab laser drops quickly with the incision depth D. This behaviour is also visible in figure 4.8 for the specific ablation energy W_{sp}, which rises steeply after an incision depth of 4 mm is reached for the slab CO_2 laser. For the short pulsed TEA CO_2 laser, the decrease in the ablation efficiency with cut depth is less pronounced. For

the two laser systems, the point of intersection of the graphs of the specific ablation energy W_{sp} (figure 4.8) is at $D \approx 6$ mm. Below this incision depth, the longer pulses are more efficient. Above this point more material is removed with the short pulsed TEA CO_2 laser at the same energy deposited in the tissue
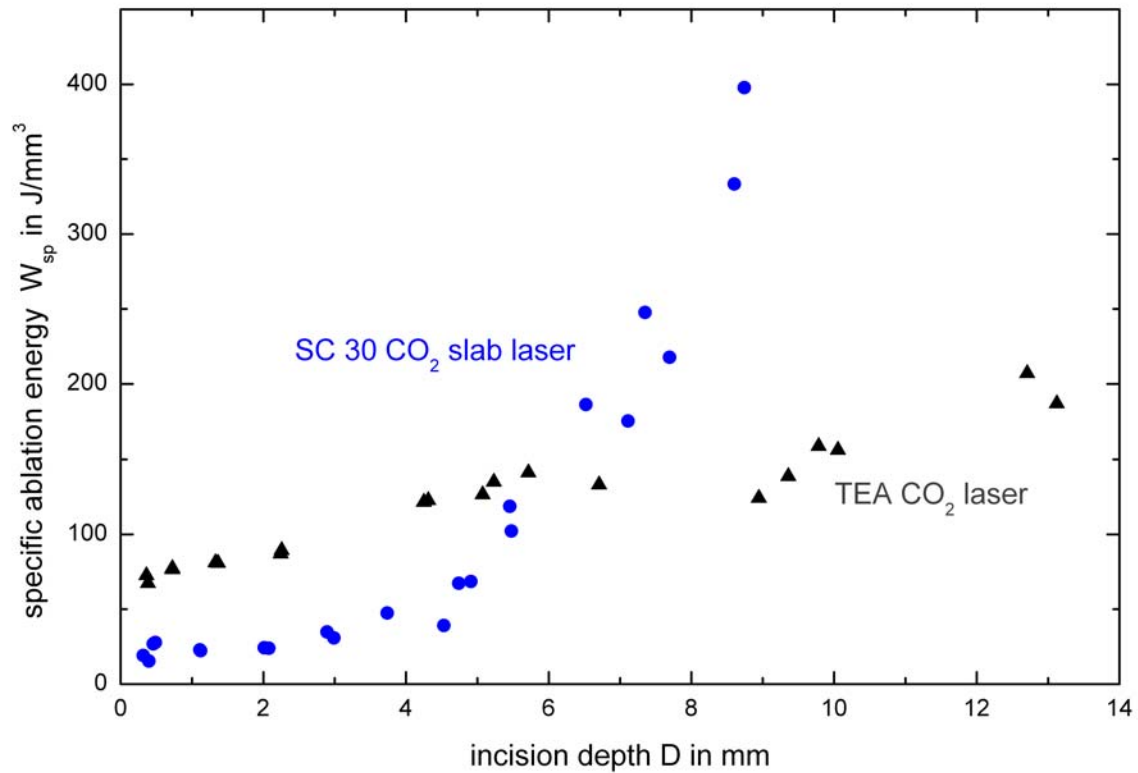
Figure 4.8: Specific ablation energy W_{sp} against incision depth D for the TEA CO_2 laser (▲) and the slab CO_2 laser (●) (same parameters as in figure 4.7)

What is essential in regard to these results is the fact that the cut depth saturates and the ablation efficiency drops with increasing incision depth. This phenomenon is generally found in laser cutting of all kinds of materials. There are two main reasons for this. With increasing incision depth, the surface of the irradiated incision walls gets larger due to the wedge shaped cut profile. As a result, the losses from heat conduction increase. Equivalently, this can be also explained in terms of steeper temperature gradients and faster thermal diffusion for the deep cuts [Iva00]. The effect is described in more detail in chapter 6.2. The second reason is that the ejected ablation products (debris) are more and more confined in the cut profile as the cut progresses deeper into the tissue. So, the absorption of the

laser light in the debris increases with rising cut depth. As a result, less energy reaches the bottom of the incision. Finally, the radiant exposure at the bottom of the incision falls below the threshold value and the ablation does not proceed anymore. These effects are more pronounced for the longer slab laser pulses (see discussion in [Iva05, Afi04]). These results are presented in this thesis to illustrate the ablation behaviour of the used lasers compared to each other. It has to be said that, below an incision depth of 4 mm, the efficiency of short sub-µs pulses is much lower compared to 80 µs pulses which contain more energy. It is interesting to apply the short pulsed TEA CO_2 laser in investigations of the physics of the ablation mechanism, as in the experiments on water dependence of the ablation process in chapter 5.1 and the temperature measurements in chapter 5.2. The slab CO_2 laser is far more suitable for (practical) medical applications as introduced in chapter 6 and the appendix.

4.4 Scanning Techniques

In the (practical) medical applications which will be presented in chapter 6 (and the appendix) of this thesis, it is necessary to achieve a certain cut depth. As mentioned above, the cut depth is, however, limited due to a decrease of ablation efficiency with depth. More precisely, the maximal achievable cut depth depends on the cut width w_{top} on the surface, i.e. the wider a cut is, the higher is the maximal achievable depth is. So actually the ratio of the possibly reached incision depth D_{max} and the width w_{top} of the cut on the sample surface is limited [Iva00]. To overcome this limitation of the cut depth a special scanning technique to broaden the laser incisions was developed in our group. With this technique it is possible to bring more light energy in deeper sections of the incision. To broaden the cut, we superimposed the "regular" trajectory of the laser beam with an additional fine and fast circular movement. That resulted in a spiral movement of the laser focus on the bone tissue sample. An optimal broadening of the original incision is obtained by choosing suitable values for the radius and the frequency of the additional circular movement matched with the laser repetition rate and linear scanning velocity. This technique is called "wobble". A comparison of the ablation efficiency for simple linear line cuts

and broadened "wobble" cuts for one common set of scanning and wobble parameters is given in chapter 6.2.

4.5 Summary Chapter 4

In this chapter the two CO_2 laser systems mainly used for the experiments in this thesis were introduced. The two systems used, are a long-pulsed slab CO_2 laser (τ = 80 µs) and a short-pulsed TEA CO_2 laser (τ = 45ns). For these two systems the ablation depth per pulse and the specific ablation energy were compared to illustrate the different ablation behaviour for different laser pulse durations. Additionally the different experimental set-ups for the laser irradiation of bone samples were described. Moreover the optical analysis of the irradiated bone samples was explained and the relevant physical parameters for quantitative interpretation of the measurement results were defined. At the end different scanning techniques were presented.

5 Investigation of Ablation Process

As described in chapter 3 the physical model of effective and clean ablation of hard bone tissue is based on the fast evaporation of water which is enclosed in the tissue. Hence, a fine water spray is directed onto the ablation spot in practical osteotomies to prevent tissue parching during laser irradiation. In the first section of this chapter the ablation process will be analysed by the comparison of the ablation efficiency for fresh and dehydrated bovine bone samples. Also laser incisions in pure sintered synthetic hydroxyapatite will be analysed. The surfaces of the cuts in different samples are studied with a scanning electron microscope (SEM) and with energy dispersive X-ray spectroscopy (EDX).

In the second section of this chapter (5.2), measurements carried out with an infrared camera, to determine the temperature development in the vicinity of the cut during laser osteotomy will be described. For the practical use in medicine, the explicit confirmation of only a small temperature rise during the ablation process is essential.

5.1 Dependence of the Ablation Process on Tissue Water Content

To investigate the dependence of the ablation process on the tissue water content three sets of bovine bone samples dehydrated in different manners and pure synthetic hydroxyapatite were irradiated with the short pulsed TEA CO_2 laser. The results were then compared with incisions in fresh bone done with the same laser parameters. Blocks of compact bovine femur bone of about 1 x 2 cm size were used. The samples had thicknesses of below 5 mm to achieve complete dehydration. The bone samples were air-dried over several weeks. After the air-

drying one part of these bone samples was furthermore dehydrated in ethanol for ten days, while another part of the bone samples was dehydrated in acetone for four days. The third part of the bones was not treated any further after the air-drying. The different bone sample groups are called air-dried samples, ethanol-preparation and acetone-preparation respectively. The bone samples from the ethanol- and acetone-preparation were taken out of the preparation fluids and were kept in an exsiccator with a desiccant for 24 hours prior to irradiation. As a control group, fresh compact bovine bone that was kept in water until the irradiation to maintain the native water content was used. This sample group is called fresh bone. The sintered synthetic hydroxyapatite sample had a purity of above 99% and did not contain water.

During the irradiation of the fresh bone samples, the usual fine air water spray was used to replace the vaporised water in the bone and prevent tissue parching. For all other samples, a gas jet of pure nitrogen gas was directed on the ablation spot to prevent water absorption from the humidity of the air and to blow away ablation debris.

A summary of the different sample groups and the irradiation set-ups is given in table 5.1.

Table 5.1: Overview of different sample groups used for experiments (colour coded like curves in figures 5.1 and 5.2)

Sample group	Sample material	Sample preparation	Sample irradiation
Ethanol preparation	Bovine femur cortical bone	Air-dried (several weeks) then further dehydration in ethanol (10 days) afterwards 24 h in exsiccator	Laser irradiation with nitrogen gas jet directed at the sample
Acetone preparation	Bovine femur cortical bone	Air-dried (several weeks) then further dehydration in acetone (4 days) afterwards 24 h in exsiccator	Laser irradiation with nitrogen gas jet directed at the sample
Air-dried	Bovine femur cortical bone	Air-dried (several weeks) and no further preparation	Laser irradiation with nitrogen gas jet directed at the sample
Pure hydroxyapatite	Synthetic sintered hydroxyapatite ceramic	No further preparation (sample does not absorb water)	Laser irradiation with nitrogen gas jet directed at the sample
Fresh bone (control group)	Bovine femur cortical bone	Fresh bone, kept in water until irradiation	Laser irradiation with fine water spray directed at the sample

For the experiments the TEA CO_2 laser MTL 3 GT, as described in chapter 4.1, was used. The pulse energy in these experiments was $E_{pulse} \approx 30$ mJ with a repetition rate of $f = 35$ Hz. The wavelength of 9.6 µm (9P22 line) was chosen. The focus diameter was $2w_f = 260$ µm ($1/e^2$ level). This gave a radiant exposure of $\Phi \approx 55$ J/cm^2. The samples were moved with a velocity of $v = 4$ mm/s through the beam with the beam focus on the sample surface, which resulted in a geometrical pulse overlap factor of $n \approx 1.14$.

All the samples were irradiated with $N = 32$, 64, 128 passes and partly also with 256 passes through the laser beam. After the irradiations the samples were analysed with optical microscopy as described in chapter 4.2. The depth D, the width at the sample surface w_{top} of the incision, and the area A of the cut profile were determined. The aim of these experiments was to confirm the postulated model of thermo-mechanical ablation driven by micro-explosions of fast evaporating water in the bone tissue. So, a drop in ablation efficiency for the dehydrated bone samples was expected. A laser irradiation without tissue water and without added water from an additional water spray would also result in some tissue removal. However, the expected ablation has to be less effective than ablation with sufficient water in the tissue. In the case of dehydrated samples, the ablation process happens at much higher temperatures because of the higher transformation and melting temperatures of collagen and hydroxyapatite compared to the water evaporation temperature. Differences in the surface morphology of the laser cuts, depending on the water content of the samples, also allow conclusions about the ablation process. Traces of molten material would indicate the occurrence of high temperatures as hydroxyapatite is thermally stable up to temperatures of 1280 °C [New 77, Nis01, Cor74].

5.1.1 Incision Depth and Specific Ablation Energy

The depth D of the laser incisions is measured directly at the cut profiles of the five sample groups (see table 5.1). In figure 5.1, the values of the incision depth are

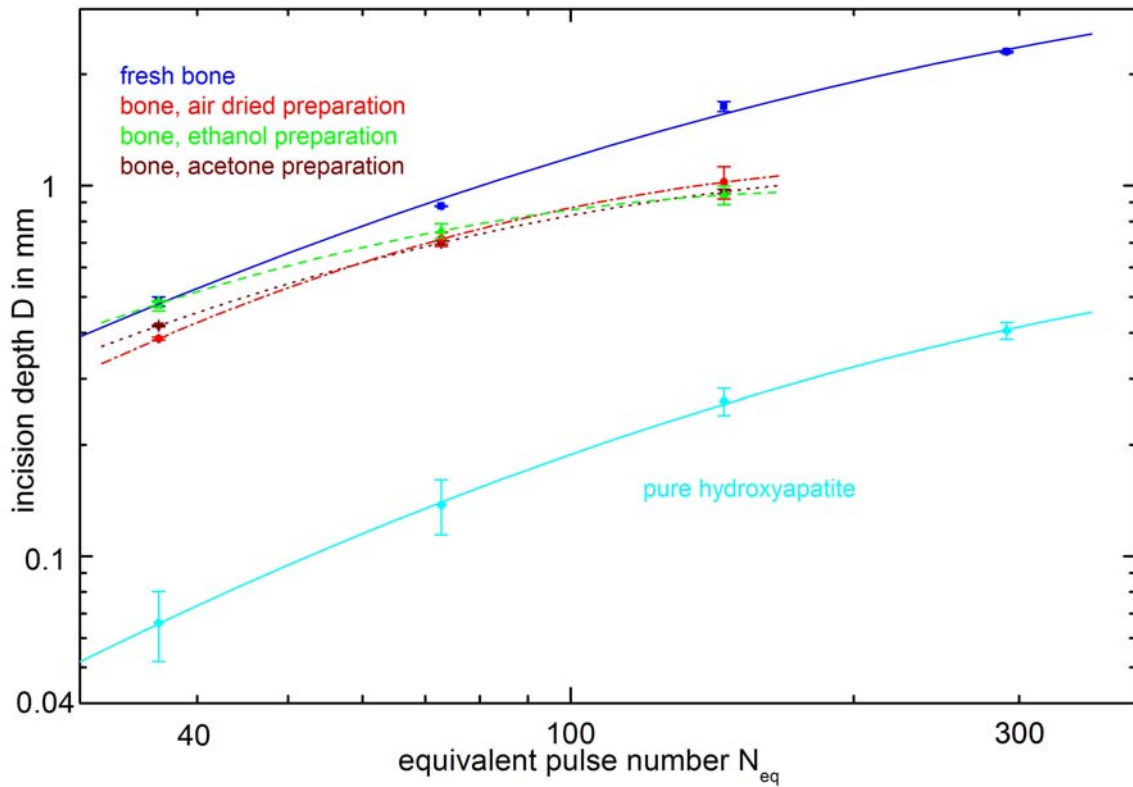plotted against the equivalent number of pulses which impinge effectively on each location along the incision.

Figure 5.1: Incision depth D against equivalent pulse number N_{eq} for laser incision with the TEA CO_2 laser in different sample groups (for fresh bone additional water spray was applied, for all other sample groups nitrogen gas jet was applied; for laser parameters, see text)

Figure 5.1 shows that the ablation of fresh compact bone with water spray is generally more effective than ablation of dehydrated bone without water spray. However, the difference between the incision depth for fresh and dry bone in shallow cuts with $N_{eq} \approx 36$ is only in the order of 0.1 mm or 20%. An especially small difference at $N_{eq} \approx 36$ is observed for the ethanol preparation and fresh bone samples. In this case, the ablation depth is practically identical for both samples. For deeper cuts the difference in the ablation depth between the fresh and the dehydrated bone increases. For an equivalent pulse number of $N_{eq} \approx 146$, the ablation depth for fresh bone is ca. 1.65 mm and for the dehydrated bone only 0.95 mm (relative difference > 40%). The reason for such behaviour is probably the humidity absorption from the atmospheric air in the surface layer of the bone

sample. It could not be completely prevented and makes the difference between fresh and dehydrated samples smaller in the surface layer. This effect seems to be especially pronounced for the sample from the ethanol preparation.

The difference between the fresh bone and the pure hydroxyapatite is considerably larger than between different bone sample preparations. The ablation depth for the fresh bone is between 6 to 7 times higher than for the hydroxyapatite at the corresponding equivalent pulse numbers.

With the data gathered from optical measurements of the cut profiles the specific ablation energy W_{sp} (eq. 4.4) was calculated. It is presented graphically in dependence on the cut depth in figure 5.2.
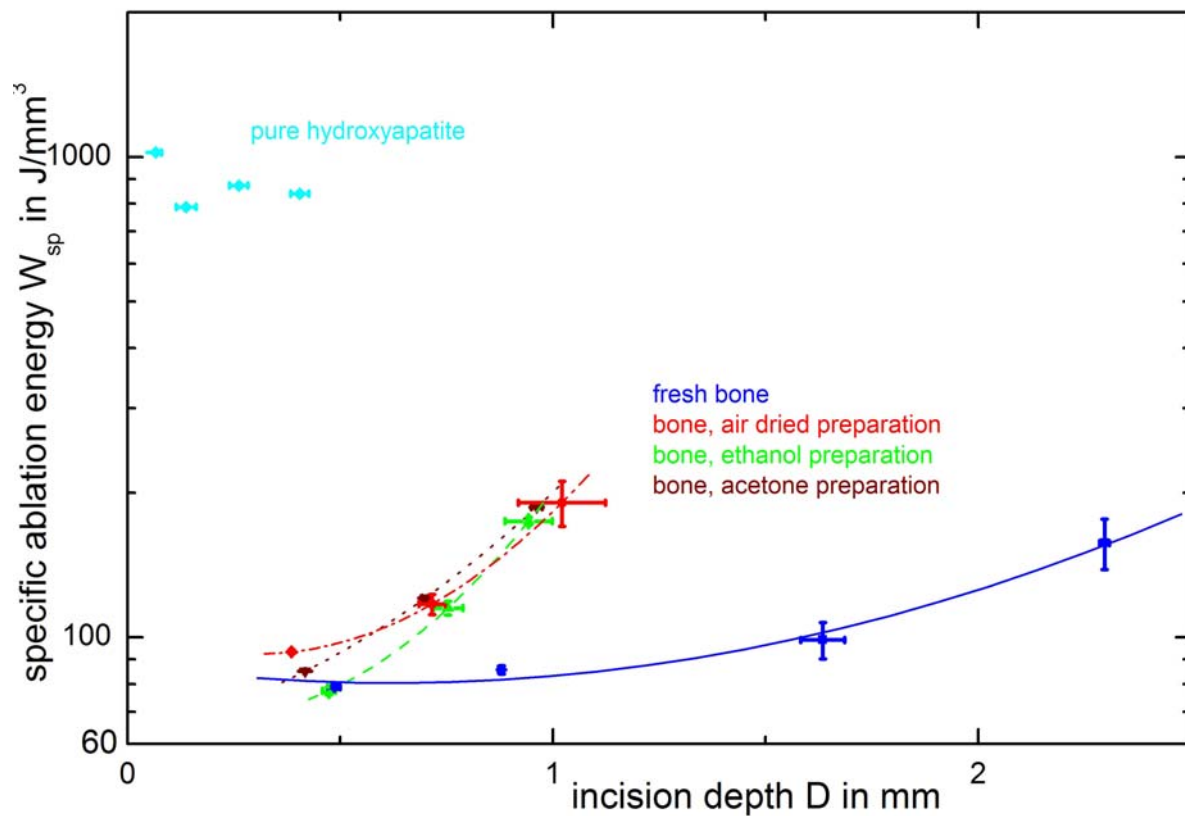

Figure 5.2: Specific ablation energy in J/mm^3 against incision depth D in mm for laser incision with the TEA CO_2 laser in different sample groups (for fresh bone additional water spray was applied, for all other sample groups nitrogen gas jet was applied, for laser parameters see text)

The specific ablation energy for the dehydrated bone samples (with nitrogen gas jet) is higher than for the fresh bone samples (see figure 5.2). This behaviour corresponds to the variation of the incision depths with the equivalent number of pulses described above. As in the plot for the incision depth against the equivalent pulse number, the difference in the specific ablation energy between fresh and dry bones increases with incision depth.

The specific ablation energy for hydroxyapatite is about 10 times higher than for compact bone with a natural composition. The cut depths achieved in the pure hydroxyapatite are very small; therefore, the usual rising of the specific ablation energy with increasing incision depth was not observed. The values for the specific ablation energy for the cut depths of 0.13 – 0.4 mm are smaller, than for D = 0.07 mm. This can be explained with the slightly reduced mechanical strength of the material in the vicinity of the cut after the first laser beam passes. The conceivable mechanism to create the laser incisions in the hydroxyapatite is to melt and vaporise the material. This process requires temperatures of over 1280 °C, as was discussed in chapter 2. This mechanism is supported by the scanning electron images of the cuts in hydroxyapatite, which will be presented in chapter 5.1.2.

Summarising one can say that the dehydration of the bone samples and the use of a nitrogen gas jet during the ablation process instead of a water spray reduces the efficiency of the ablation process, but bone tissue removal is still possible, although with a noticeable thermal damage. The visual appearance of the cuts is slightly darkened. However, a severe carbonisation with a distinctly visible darkening could be avoided in this case due to the use of a nitrogen gas for the "dry" laser irradiations. Nevertheless the occurrence of thermal damage is clearly visible for the "dry" bone ablation in the following analysis of scanning electron images of the cut surfaces. This reduction of the ablation efficiency is an indication for the water driven thermo-mechanical model of the hard tissue ablation. The process of the tissue removal without water can be driven by collagen decomposition, vaporisation and melting of the hydroxyapatite. These processes take place at much higher temperatures than the desired thermo-mechanical ablation process with fast

water evaporation as a driving force. This is also supported by the results of the scanning electron images.

5.1.2 Investigation of Laser Cut Morphology with SEM

With a scanning electron microscope (SEM) it is possible to get high resolution images of sample surfaces with an excellent three dimensional presentation. The SEM images are very suitable for judging the surface structure of the examined sample. In the SEM electrons are emitted thermally or via field emission from a cathode and are accelerated in an electric field with a variable voltage usually of up to 30 kV. With the help of magnetic coils the electron beam is focussed on a small "point" of the sample surface. To create an image, a pair of scanning coils deflects the electron beam in a raster fashion over a rectangular area of the surface. This is the origin of the name scanning electron microscope. For each position of the scanning beam on the sample surface, the amount of secondary and/or backscattered electrons emitted from the sample is detected. So, a two dimensional image of the sample surface is generated. The primary electrons interact with atoms in the sample material, the incoming electrons are in-elastically scattered and the primary electron beam effectively spreads out in the material to a drop-shaped interaction volume extending to a depth of about 1 to 5 μm. The most common way to create the SEM image is the detection of low energy secondary electrons. Due to the low energy of the electrons their origin is positioned in a very thin layer on the sample surface. The surface morphology of the different incisions in the different samples was examined with a scanning electron microscope (LEO Supra 55 for all of the bone samples and Leo 1430 VP for the hydroxyapatite sample). None of the samples used here was coated with a conducting layer (e.g. gold), so the used accelerating voltage was limited to 3 kV for the bone and 20 kV for the hydroxyapatite sample to minimise surface charging effects. Magnification factors of up to 30.000 were reached. SEM images were recorded from laser cuts in the pure hydroxyapatite, in fresh bone and the ethanol and acetone prepared bones.

5.1.2.1 Incisions in Pure Hydroxyapatite

In figure 5.3, a shallow incision with only 8 passes of the focussed laser beam over the hydroxyapatite sample (N_{eq} = 9.1) is shown. The view is from the side into the incision groove. The borderline between the incision groove and the sidewall of the sample is indicated by black arrows. The red arrow indicates the way the laser beam moved.

Figure 5.3: Laser incision in pure hydroxyapatite, 8 laser passes (N_{eq} = 9.12) (irradiation parameters as described in chapter 5.1), red arrow indicates direction of laser movement

The whole cut surface is covered with material which has been molten and has solidified again (vitrification). This indicates that the process temperature during the laser ablation has reached the melting temperature of hydroxyapatite at 1280°C. Material removal is still possible as already mentioned in chapter 5.1. The underlying ablation mechanism here is simple thermal material removal by melting and displacing of the material and not thermo-mechanical ablation. This is supported by the molten and re-solidified surfaces seen in figures 5.3 and 5.4. Figure 5.4 depicts a deeper incision in hydroxyapatite with 128 laser passes (N_{eq} =

145.9) over the sample. The image is from the same relative viewpoint as figure 5.3. The layer of material which was molten during the ablation process is clearly visibly. In the middle of the picture, the end of the incision and the transition from cut wall and not irradiated side of the sample is visible (black arrows). On the right side of the image (white arrow), traces of re-solidified hydroxyapatite are visible which have been blown out of the cut by the nitrogen gas jet while the material was liquid.
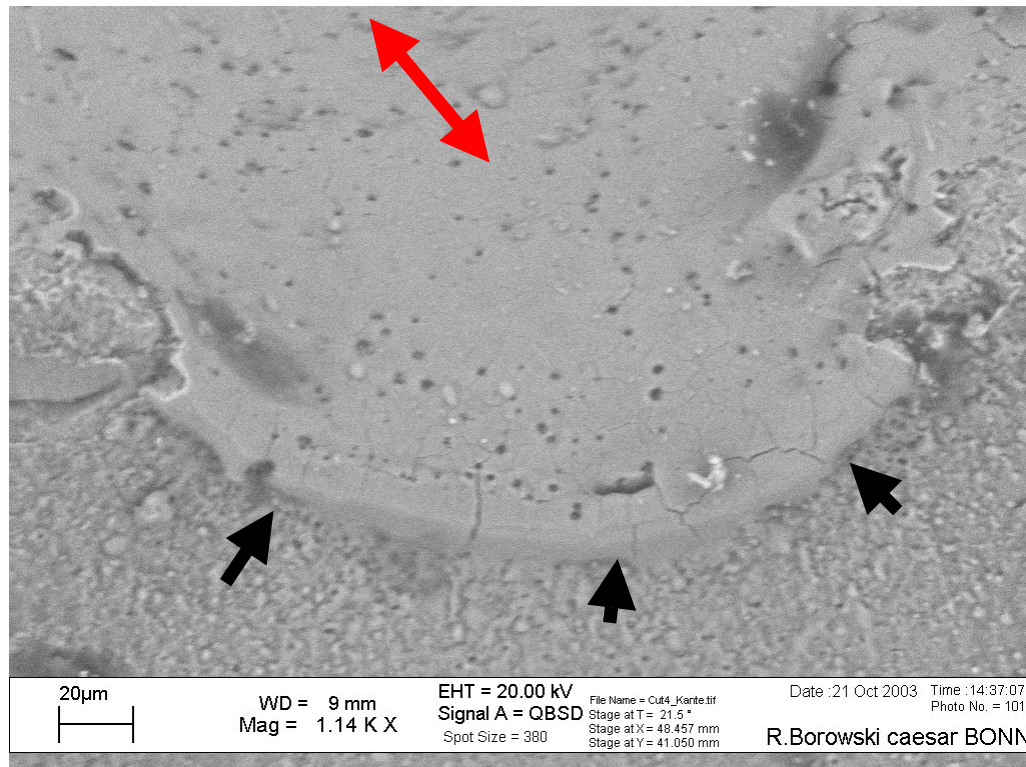

Figure 5.4: Laser incision in pure hydroxyapatite, 128 laser passes (N_{eq} = 145.9) (irradiation parameters as described in chapter 5.1), red arrow indicates direction of laser movement

5.1.2.2 Incisions in Bones after Ethanol Preparation

The walls of the laser incisions in ethanol dehydrated bone also display signs of melting as can be seen in the SEM image in figure 5.5. In this picture, the bottom of the incision is shown after 32 passes ($N_{eq} \approx 36.5$) of the laser beam over the dehydrated sample from the ethanol preparation. In the image, the view into the bottom of the incision is depicted. The direction of the laser beam movement is indicated by the red double arrow. Parallel grooves in the bottom of the incision along the laser beam movement are visible, probably originating from individual

laser passes. The spacing between the grooves is in the range of 10 µm. This observation indicates that the laser beam position slightly moved relatively to the bone sample. The direction of the movement was perpendicular to the sample movement. The movement can result from small variations of the laser pointing stability or from a movement induced by the drive stage. However, the amplitude of the movement is with values in the order of 10 µm quite small. Deposits of molten and re-solidified material, indicated by the white arrows in figure 5.5, are especially along the borders of the individual grooves of the laser passes. In the upper part of the picture the side face of the bone sample is visible. This surface resulted from a saw cut in the bone. The border between the saw cut surface and the laser incision is indicated by black arrows in figure 5.5. In the surface created with a saw cut are multiple cracks, which are not found in areas of laser incisions (excluding the area near the saw surface).
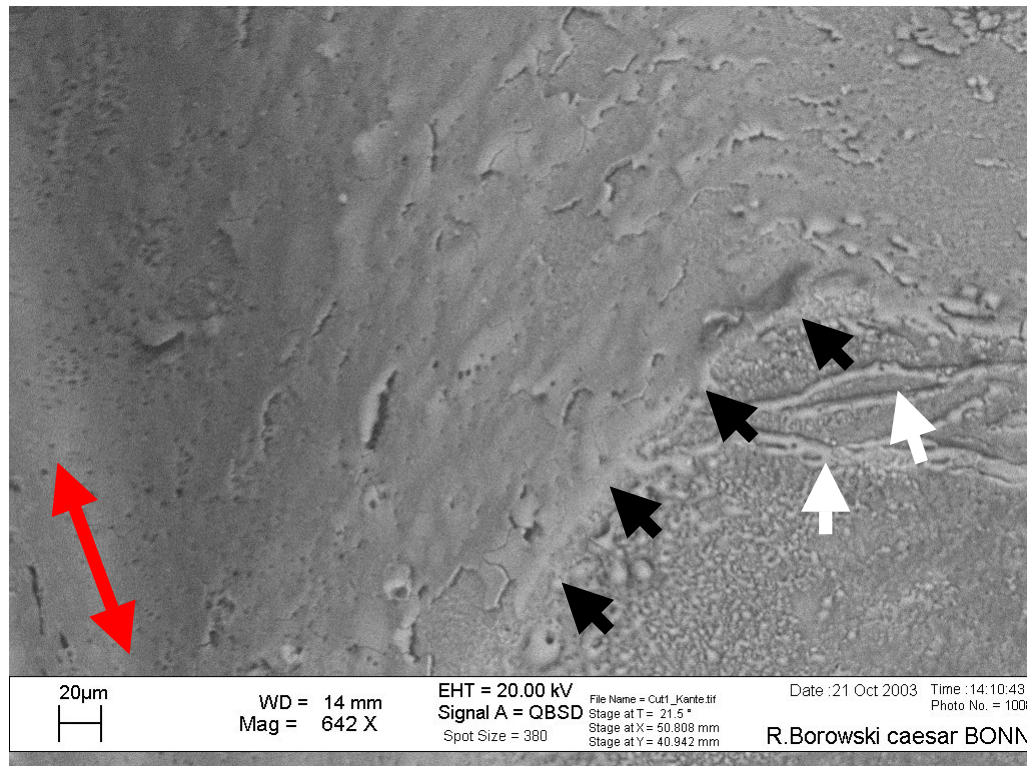

Figure 5.5: Laser incision in ethanol dehydrated bone, 32 laser passes (N_{eq} = 36.5) (irradiation parameters as described in chapter 5.1), red arrow indicates direction of laser movement, white arrows indicate zone where re-solidified molten material is deposited

Figure 5.6 displays a section in the middle part of the bottom of the same incision. Again, the grooves of the individual laser passes can be recognised with

deposition of molten material at the borders (white arrows). In figure 5.7, a higher magnification of a section (white frame in figure 5.6) from the bottom of the laser incision in the ethanol dehydrated bone is shown. Small droplets of re-solidified material characterised by a smooth glazed surface are clearly visible in the high magnification image (figure 5.7, black arrows).
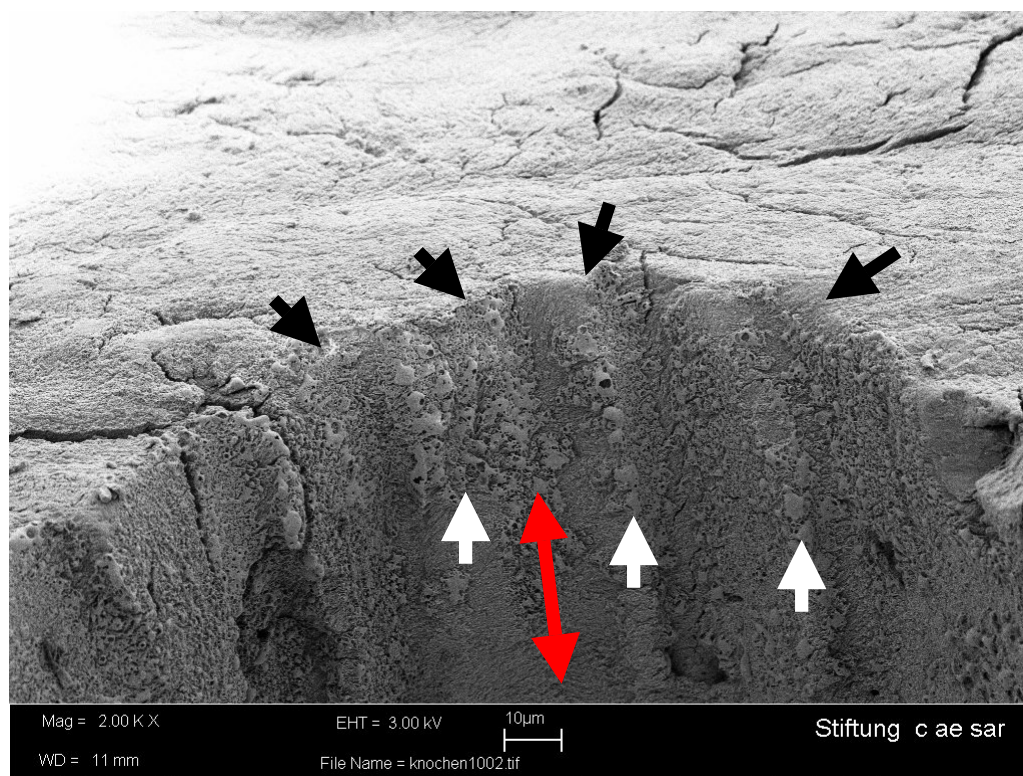

Figure 5.6: Laser incision in ethanol dehydrated bone, 32 laser passes (N_{eq} = 36.5) (irradiation parameters as described in chapter 5.1), red arrow indicates direction of laser movement, view of the bottom of the incision

Figure 5.8 depicts the cut border of a deeper laser incision (64 passes, N_{eq}=73) in ethanol dehydrated bone. At the edge of the incision, at the transition to the sample surface that was not irradiated, extensive deposit of molten and subsequently solidified bone material is recognisable. This strong covering of the upper incision walls probably results from originally hot material which was ejected during the ablation process from deeper incision sections. In figure 5.9.a, a representative area of the cut wall with the covering of molten material is shown. In figure 5.9.b, the area of the white frame in figure 5.9.a is shown at a higher magnification.

Figure 5.7: Laser incision in ethanol dehydrated bone, 32 laser passes (N_{eq} = 36.5) (irradiation parameters as described in chapter 5.1), view of the bottom of the incision, section (white frame) from figure 5.6 with higher magnification
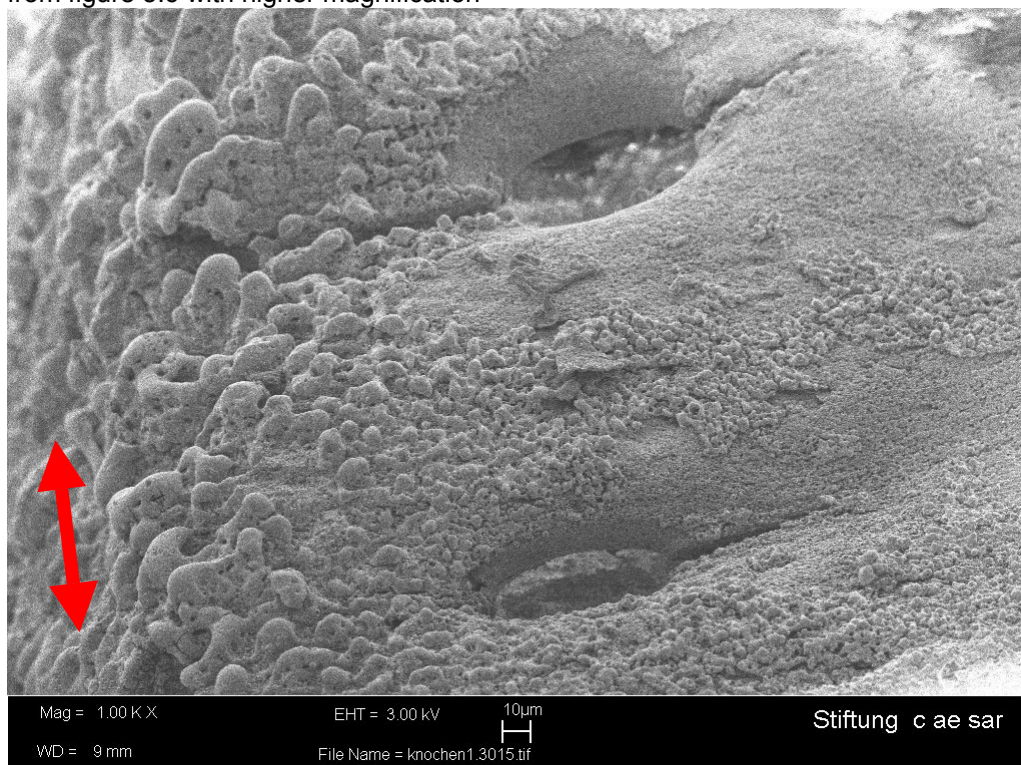
Figure 5.8: Laser incision in ethanol dehydrated bone, 64 laser passes (N_{eq} = 73) (irradiation parameters as described in chapter 5.1), view of the transition between incision sidewall and bone surfaces, pores in the bone surface are visible
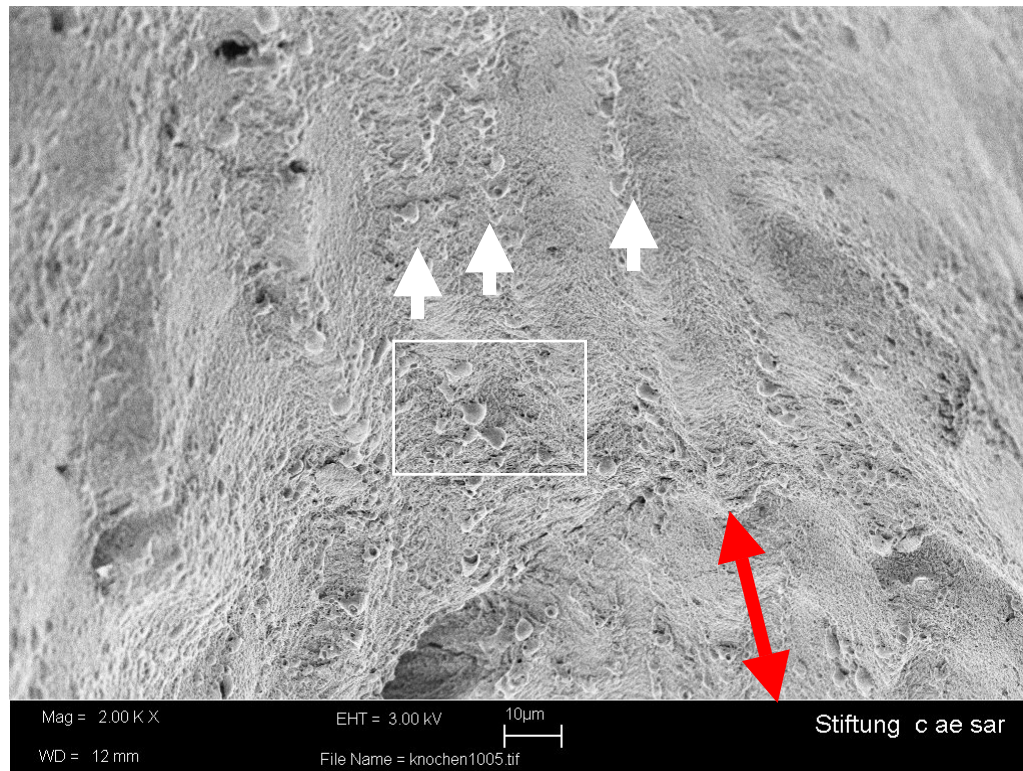
Figure 5.9.a: Laser incision in ethanol dehydrated bone, 64 laser passes (N_{eq} = 73) (irradiation parameters as described in chapter 5.1), view of the incision sidewall and bone surfaces

Figure 5.9.b: Laser incision in ethanol dehydrated bone, 64 laser passes (N_{eq} = 73) (irradiation parameters as described in chapter 5.1), view of the incision sidewall and bone surfaces, higher magnification of a section (white frame) from figure 5.9.a

All pictures of laser incisions in ethanol dehydrated bone reveal distinct signs of mineral component melting (see also results of EDX-spectroscopy in 5.3.1), which indicates very high temperatures during the laser irradiation.

5.1.2.3 Incisions in Bones after Acetone Preparation

The irradiated bone samples dehydrated in acetone show similar signs of melting induced during the ablation process as the ethanol dehydrated bone samples after laser irradiation. In figure 5.10, a laser cut in an acetone dehydrated bone is shown. The red double arrow indicates the direction of the laser beam movement and is positioned at the bottom of the incision. 32 passes of the laser beam over the sample were applied for this incision. The black arrows at the border of the cut indicate a riffled zone with intense deposition of molten bone material.
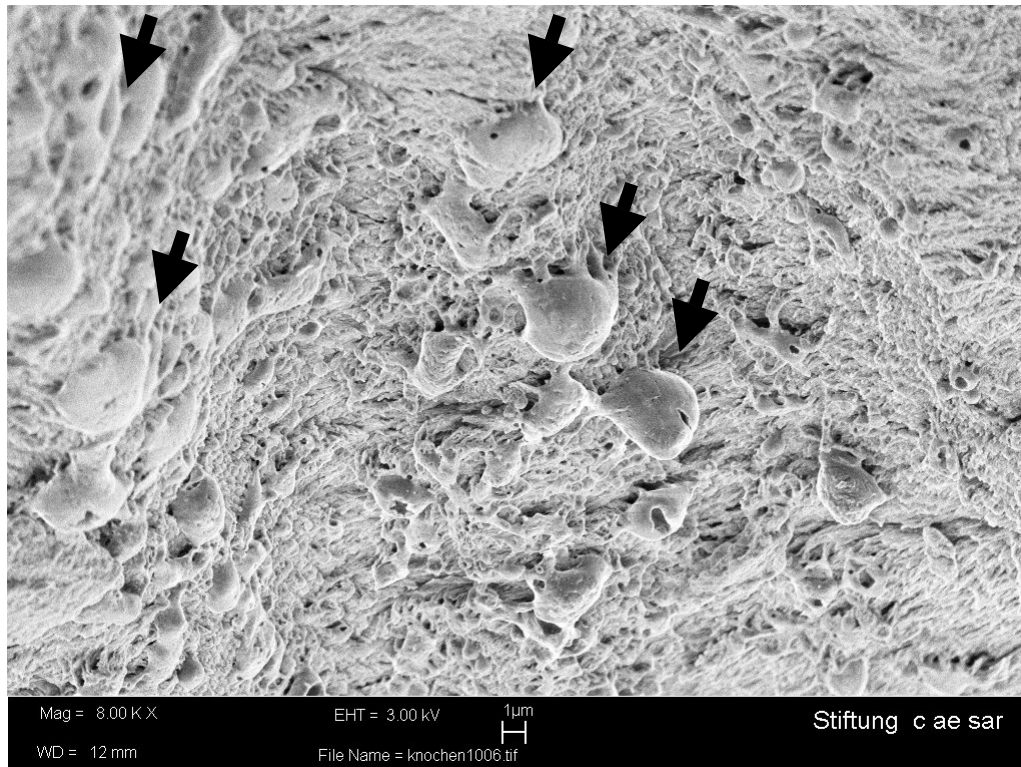

Figure 5.10: Laser incision in acetone dehydrated bone, 32 laser passes (N_{eq} = 36.5) (irradiation parameters as described in chapter 5.1), view into the incision groove created by the laser passing over the sample, red double arrow indicating direction of beam movement

Figure 5.11: Laser incision in acetone dehydrated bone, 32 laser passes (N_{eq} = 36.5) (irradiation parameters as described in chapter 5.1), view of the border of the incision, riffled structure with deposit of molten material, area in white frame is shown also in figure 5.12 with higher magnification
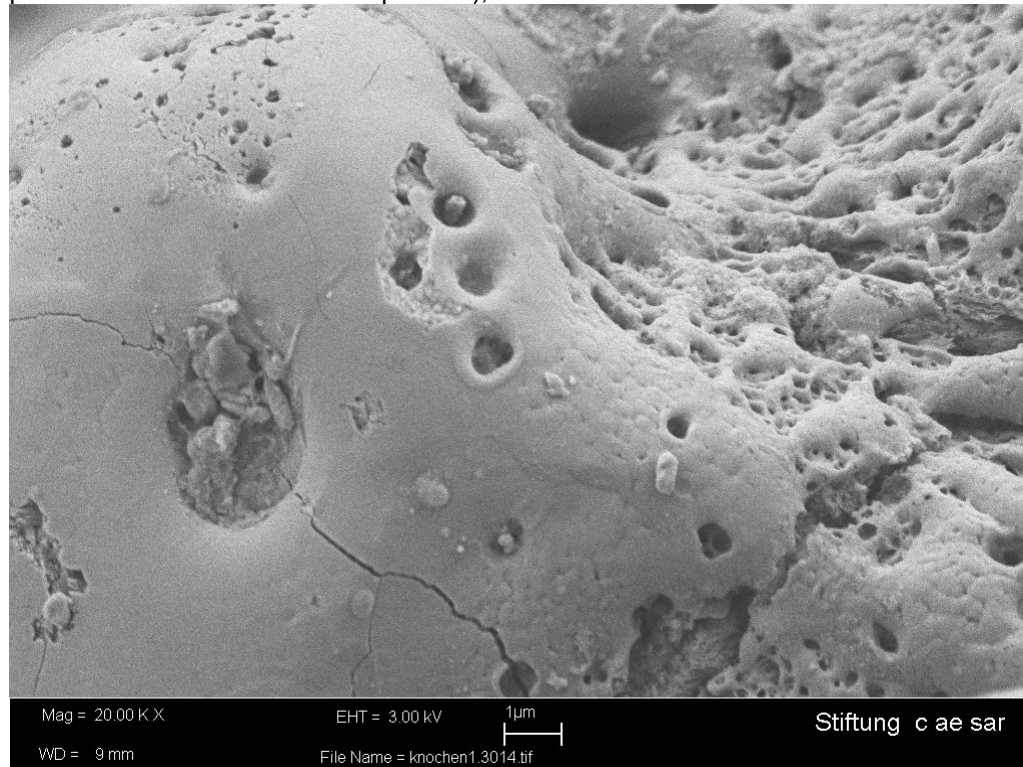

Figure 5.12: Laser incision in acetone dehydrated bone, 32 laser passes (N_{eq} = 36.5) (irradiation parameters as described in chapter 5.1), view of the border of the incision, riffled structure with deposit of molten material, area in white frame from figure 5.11 with higher magnification

In figure 5.11 and 5.12, the riffled zone with strong coating of molten and re-solidified material is shown in a higher magnification. The traces of molten material are clearly visible. The riffle structure is due to the impact of individual laser pulses.

In figure 5.13 a section in the bottom of the incision is shown. A micro-crack is visible and some traces of molten material. The crack could be the result of mechanical stress related to a fast rising of a strong temperature gradient by the laser pulse application without water or from the vacuum preparation for the scanning electron microscopy. In the crack, the fibrous collagen structure is visible. A high magnification image of this section is shown in figure 5.14. Again, signs of bone melting indicate high temperatures during the ablation process without water, as already seen in the ethanol dehydrated samples.

Mag = 21.14 K X   EHT = 3.00 kV   1µm   Stiftung c ae sar
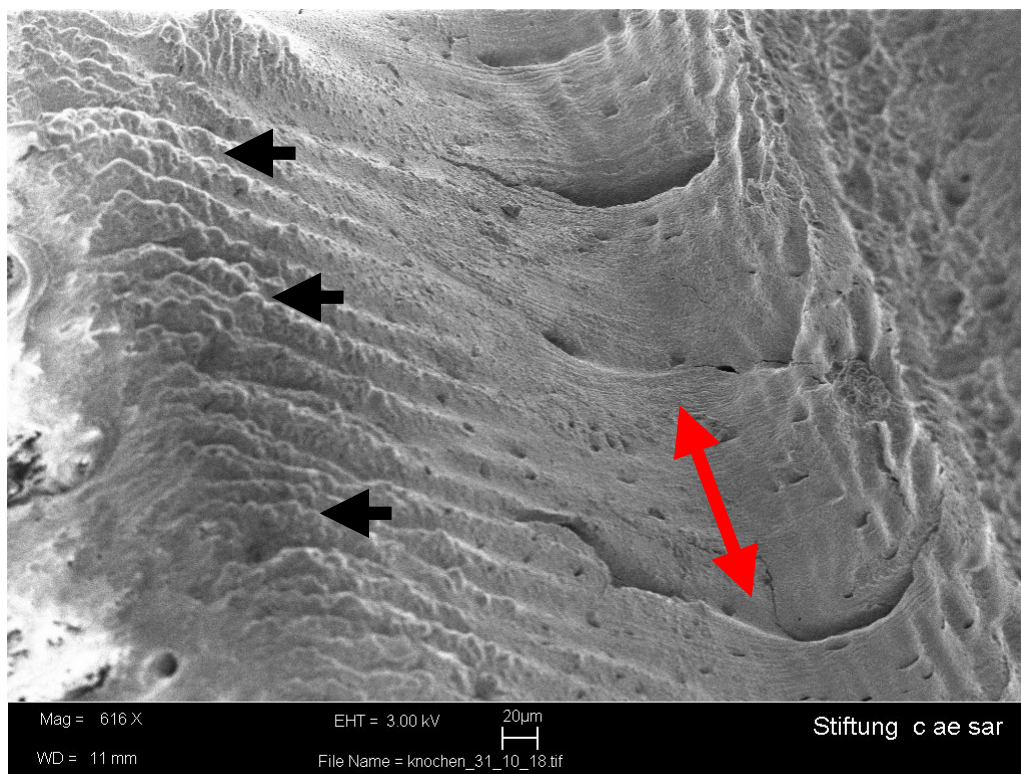WD = 11 mm   File Name = knochen_31_10_28.tif

Figure 5.13: Laser incision in acetone dehydrated bone, 32 laser passes (N_{eq} = 36.5) (irradiation parameters as described in chapter 5.1), view of the bottom of the incision, micro-crack and traces of molten material
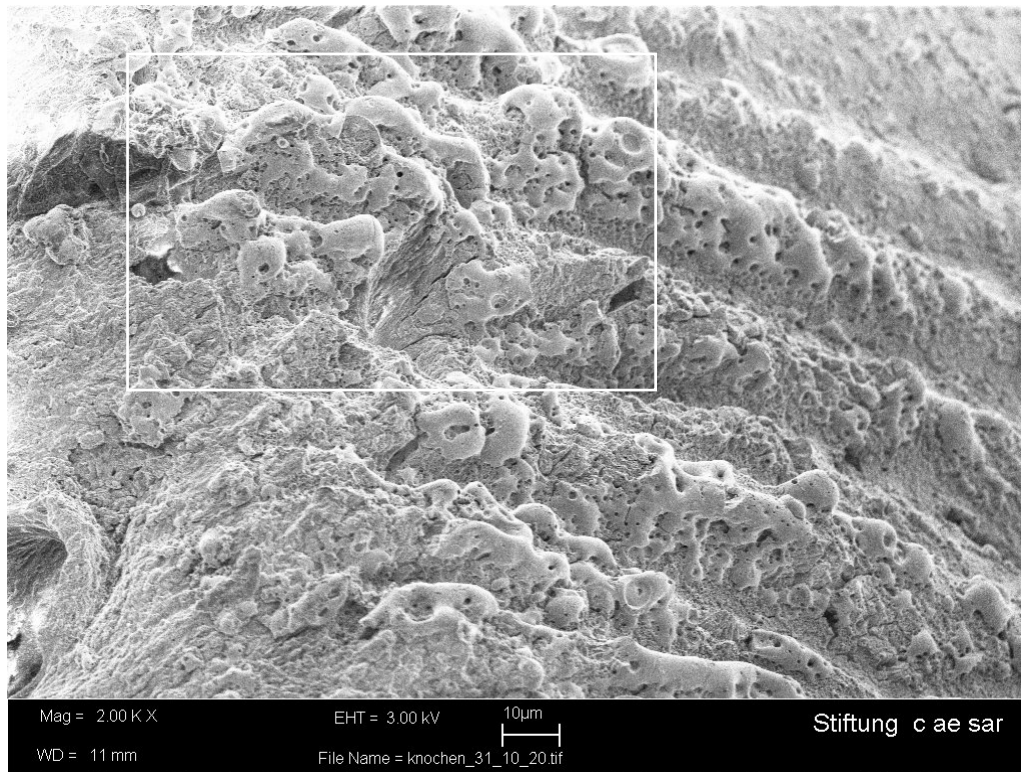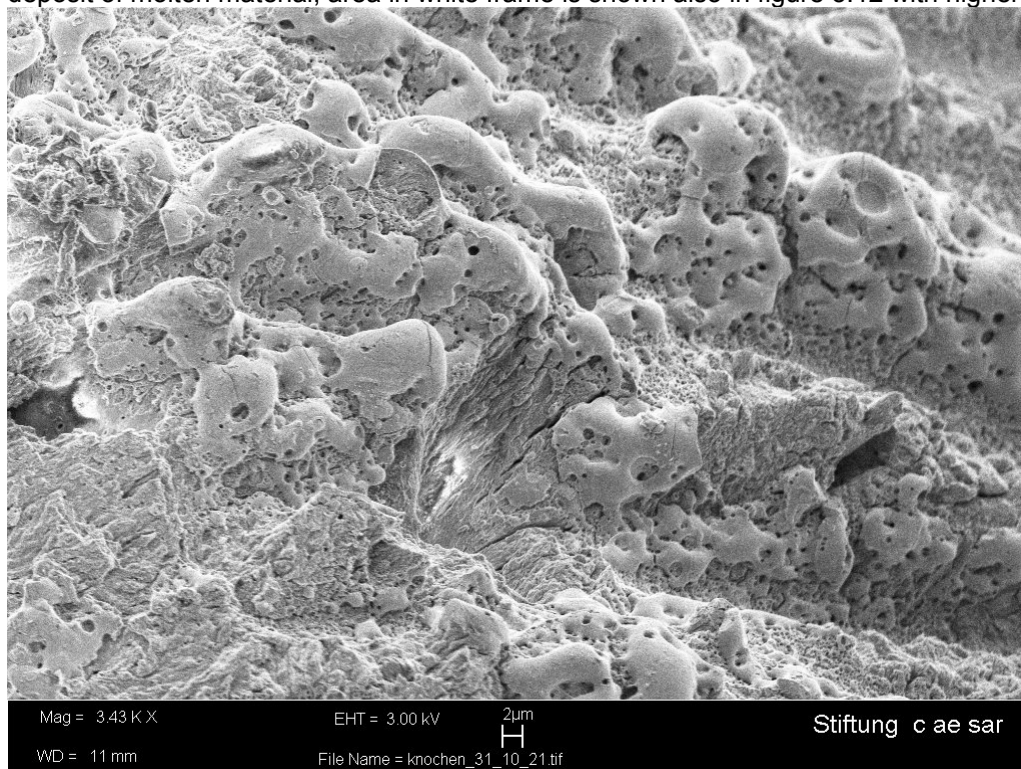
Figure 5.14: Laser incision in acetone dehydrated bone, 32 laser passes (N_{eq} = 36.5) (irradiation parameters as described in chapter 5.1), view of the bottom of the incision, micro-crack and traces of molten material with higher magnification

5.1.2.4 Incisions in Fresh Bones

Figure 5.15 shows a shallow incision in fresh bone with only four laser passes ($N_{eq} \approx$ 4.5). No traces of molten bone material are visible. The direction of the laser beam movement is indicated by the red double arrow. The border of the incision channel is indicated by black arrows. The white arrow indicates the transition between the laser cut and the saw processed side face of the bone sample. Figures 5.16.a and 5.16.b depict a deeper incision in fresh bone. Here, 32 laser passes ($N_{eq} \approx$ 36.5) were applied. No traces of molten bone are visible in the cut or at the edges of the cut of this fresh bone sample irradiated with additional water spray. The rim of the incision groove is not covered with re-solidified bone material as compared to incisions in dehydrated bone, for example with figure 5.8 or 5.10.
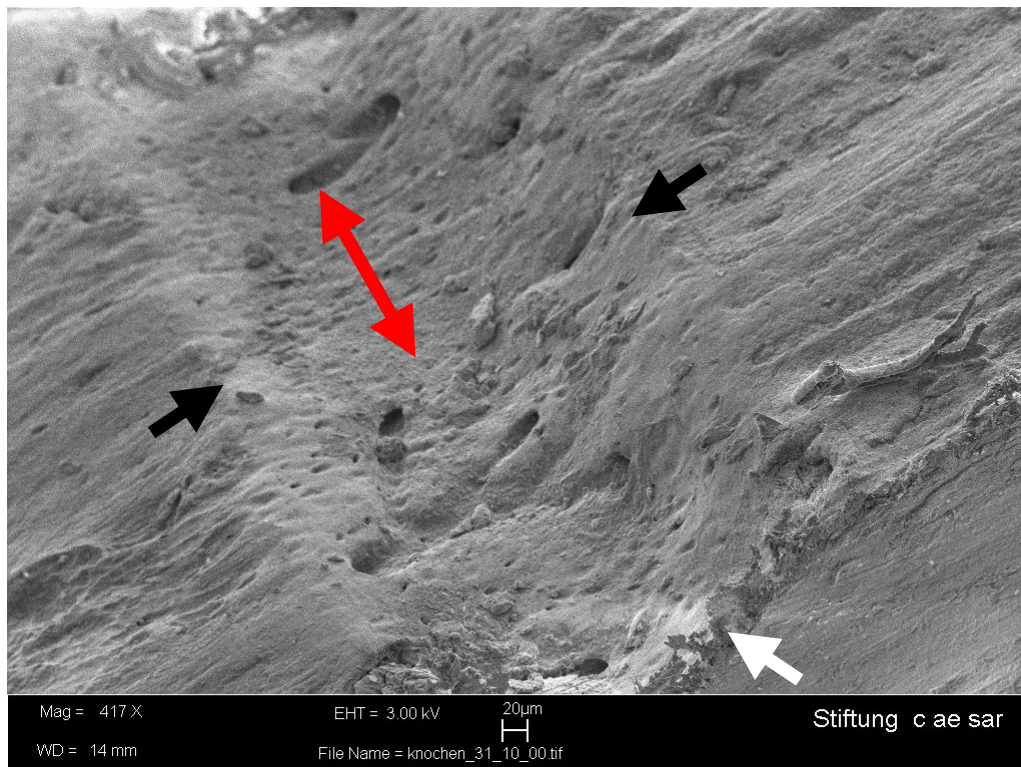
Figure 5.15: Shallow laser incision in fresh bone, 4 laser passes (N_{eq} = 4.5) (irradiation parameters as described in chapter 5.1), view into incision groove
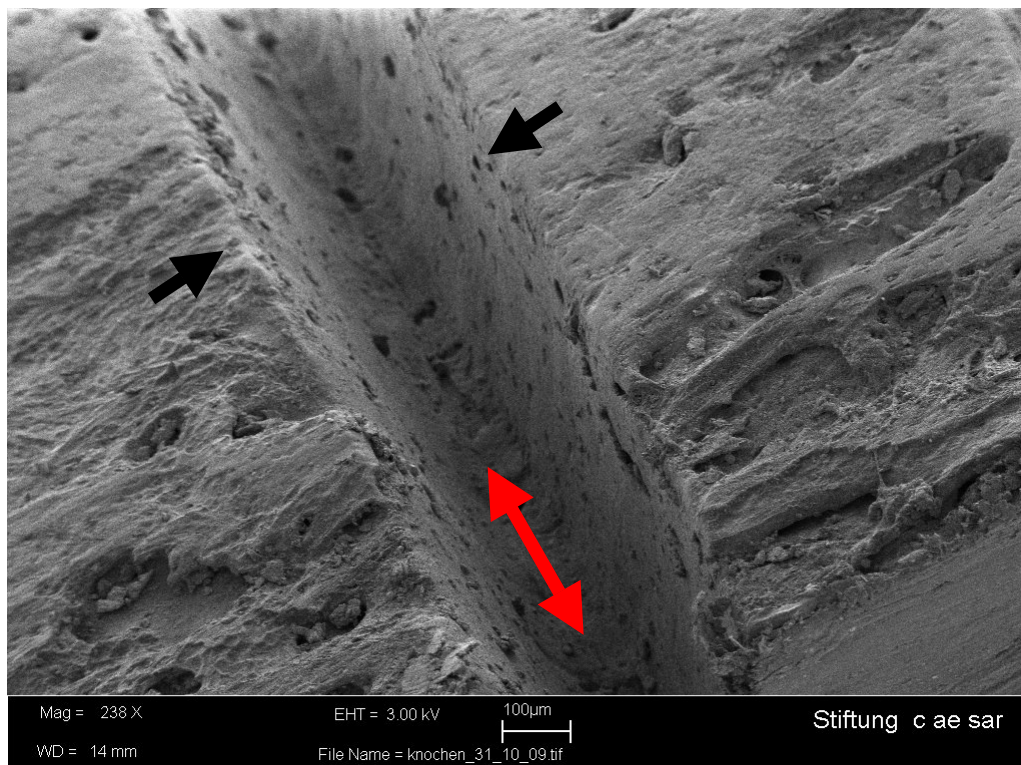
Figure 5.16.a: Laser incision in fresh bone, 32 laser passes (N_{eq} = 36.5) (irradiation parameters as described in chapter 5.1), view into incision groove
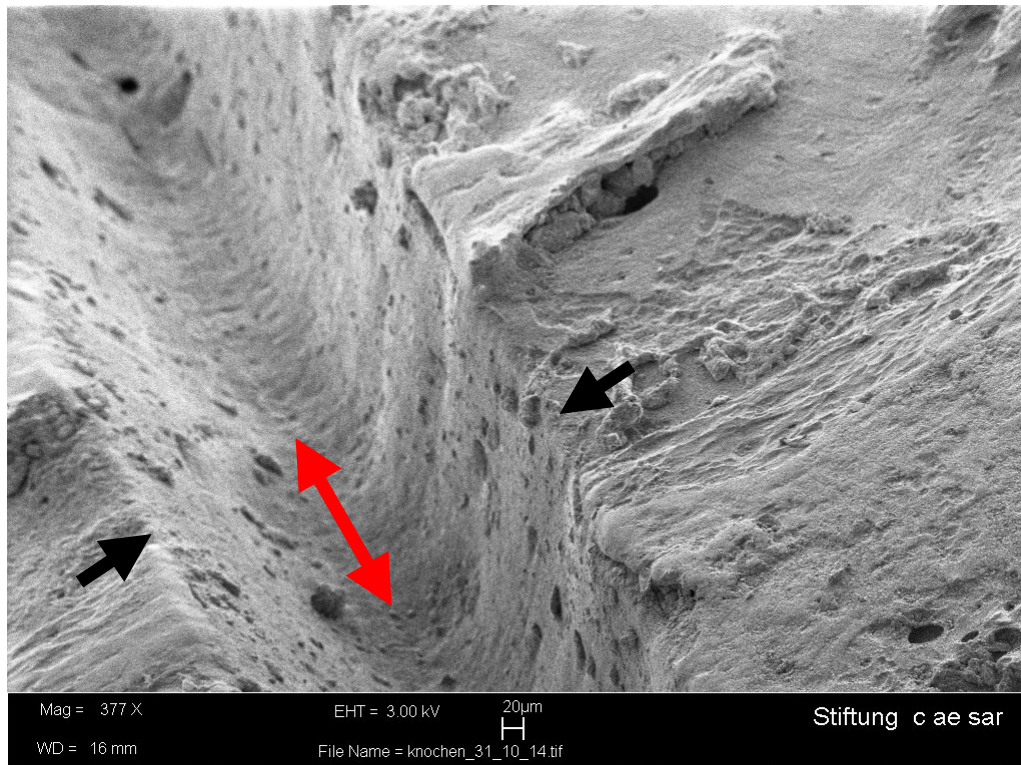
Figure 5.16.b: Laser incision in fresh bone, 32 laser passes (N_{eq} = 36.5) (irradiation parameters as described in chapter 5.1), view into incision groove
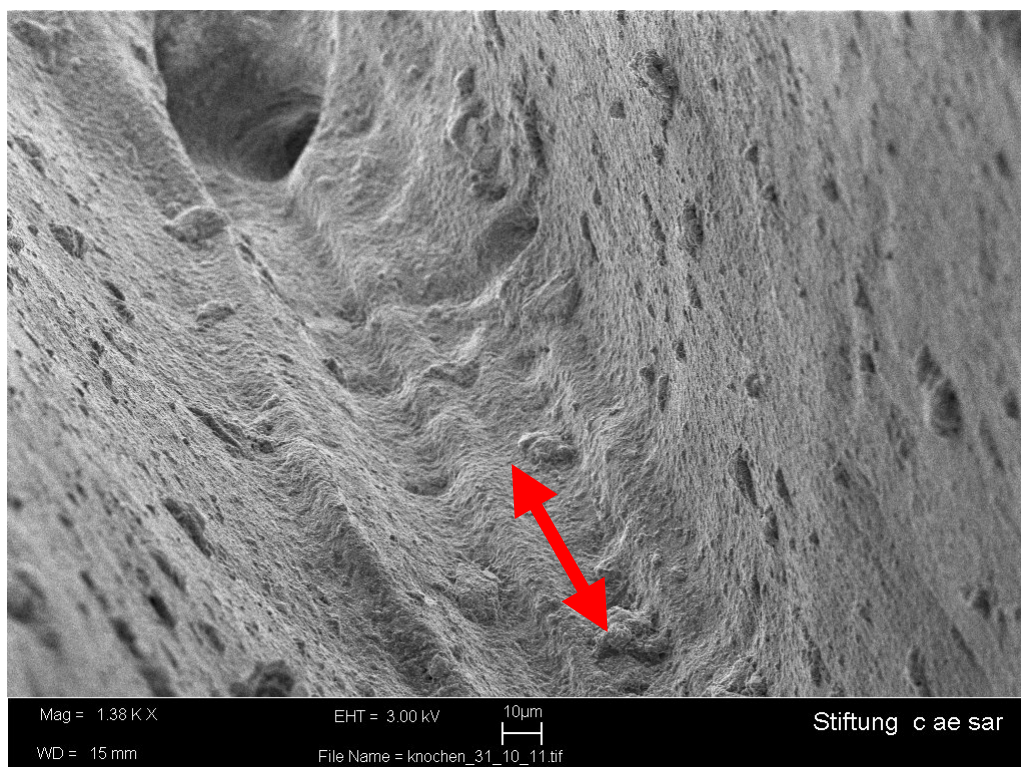
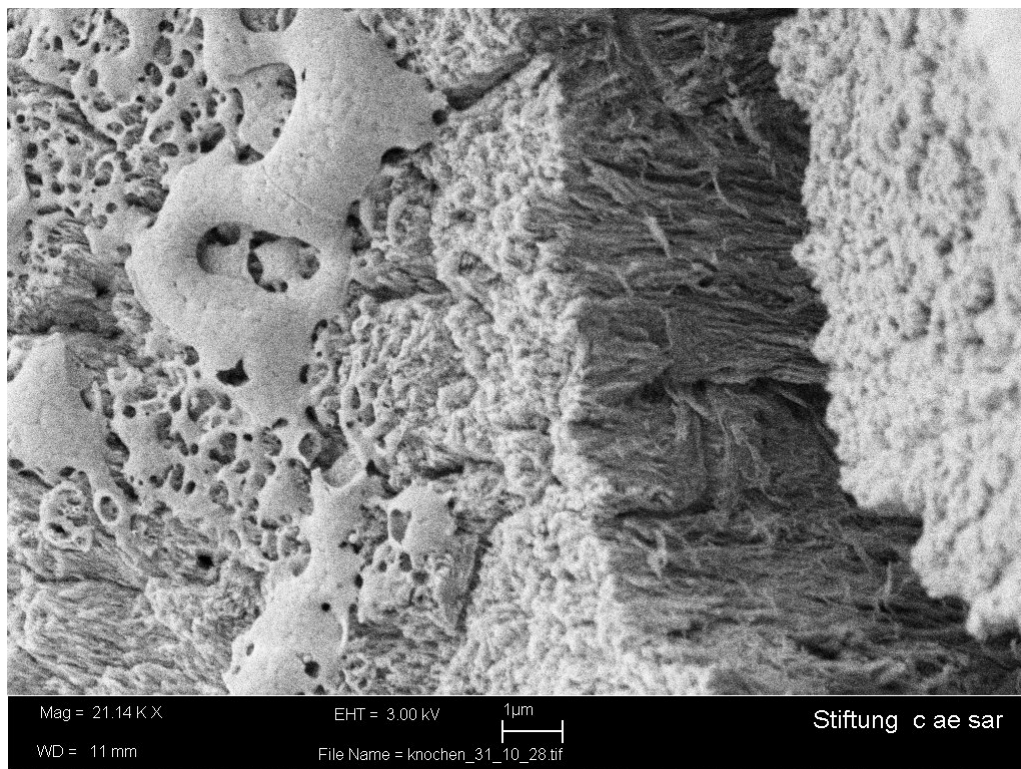**Figure 5.17:** Laser incision in fresh bone, 32 laser passes (N_{eq} = 36.5) (irradiation parameters as described in chapter 5.1), view of the bottom of the incision

Figure 5.17 shows the ground of an incision in fresh bone (laser beam movement along red double arrow). Traces of individual laser passes are visible. There is no molten material on the bottom. Neither are traces of molten material visible also at a higher magnification (figure 5.18). This is very different to, for example, figure 5.7, which shows a comparable section of an incision in a laser irradiated bone sample from the ethanol preparation.
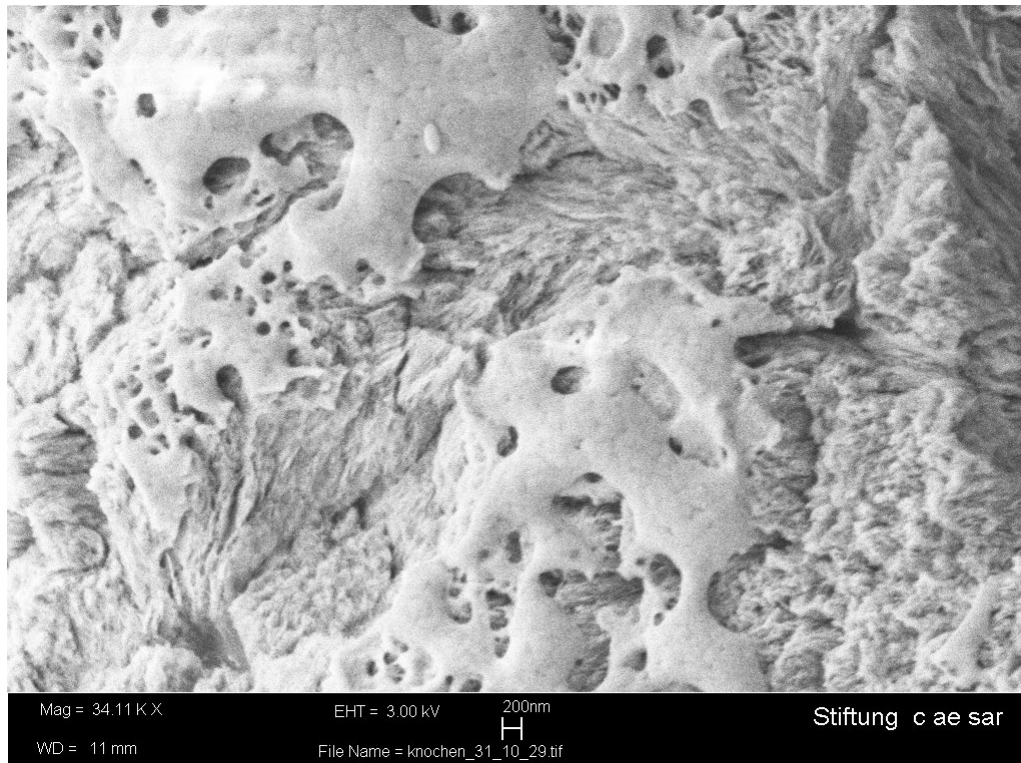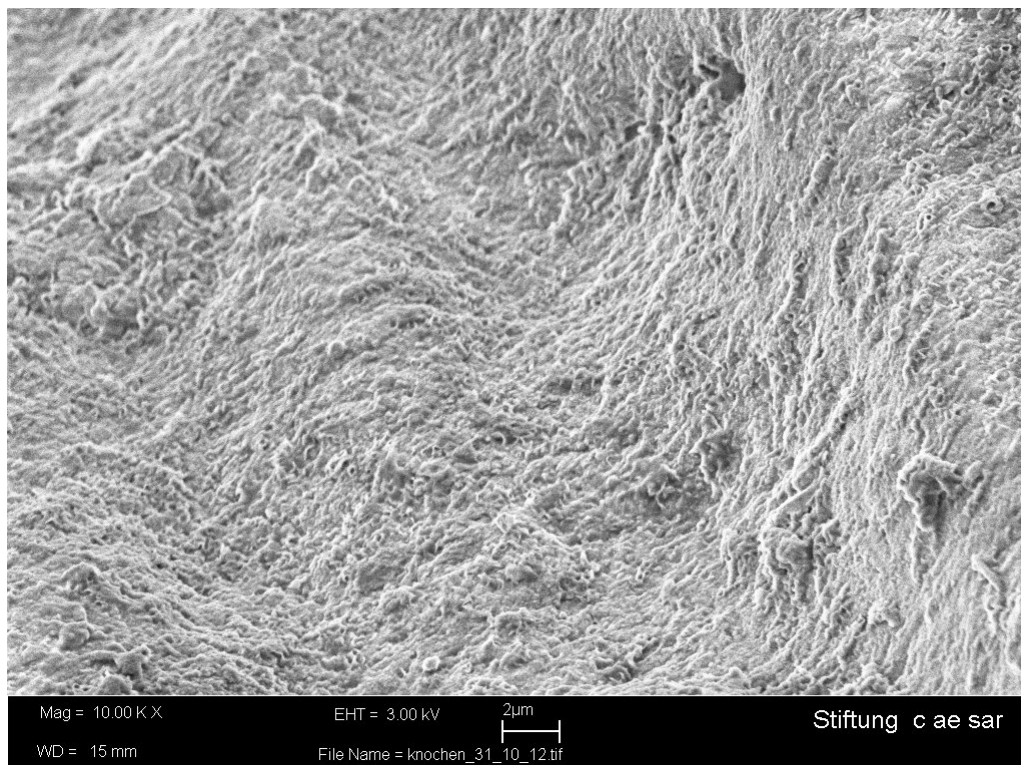

Figure 5.18: Laser incision in fresh bone, 32 laser passes (N_{eq} = 36.5) (irradiation parameters as described in chapter 5.1), view of the bottom of the incision with high magnification

5.1.2.5 Summary of Laser Cut Morphology

The scanning electron microscopy shows that in and around the laser incisions in pure hydroxyapatite and in the dehydrated bone samples molten and re-solidified material is present which was deposited there during or immediately after the ablation process. The signs of melting during the irradiation of pure hydroxyapatite indicate that the temperature during irradiation without water spray can reach at least 1100 - 1280°C, the melting temperature of hydroxyapatite. The same is

applicable to the dehydrated bone samples. The absence of the melting traces in the laser incision in fresh bone under the additional application of a water spray indicates much lower process temperatures. This proves that the ablation mechanism is based on a fast explosion-like evaporation of the water confined in the tissue [Iva98], as it has been postulated earlier for the Er:YAG laser [Wal89, Hib89]. The ablation process also has a higher efficiency under such conditions (see chapter 5.1). Due to this, more material is ablated per pulse. Thus, more heated material is removed from the bone, and less heat remains in the tissue. Moreover, the water has an additional cooling effect and absorbs excessive heat. The fact that the application of a water spray significantly reduces the process temperature is supported by the temperature measurements reported in chapter 5.2 of this thesis. Similar SEM pictures have previously been observed for a Q-switch CO_2 laser (pulse duration of 300 ns, wavelength of 9.6 µm) with water spray [Iva05, Sta01, OLE99].

5.1.3 Energy Dispersive X-Ray Spectroscopy (EDX)

Another way to analyse samples with the SEM, besides imaging, is the recording of energy dispersive X-ray fluorescence spectra (EDX spectra [Gar03]). Various interaction processes between the electrons and the atoms of the sample take place when accelerated electrons hit the sample. Among these are the emission of secondary (and re-emission of back scattered) electrons, which can be used for imaging purposes as shown in chapter 5.1.2, and the generation of X-ray radiation. The resulting X-ray emission consists of continuum X-ray radiation ("bremsstrahlung") and characteristic X-ray radiation. The characteristic X-ray radiation is generated when an electron with sufficient energy collides with an atom of the sample and knocks a bound electron out of an inner shell. As a result, electrons from higher energy levels then fill the vacancy and characteristic X-ray radiation is emitted. The characteristic part of the X-ray spectrum consists of discrete spectral lines with energies characteristic for the elements of the sample.

So, it is possible to determine the atomic composition of the sample material by the emitted X-ray radiation. The experiments were carried out with an energy sensitive semiconductor EDX detector (Oxford INCA X-sight) with an energy resolution of 0.133 keV that was attached to the scanning electron microscope. The accelerating voltage of the electrons was chosen to be 20 keV. The electrons only penetrate some micrometers into the sample, and the information received only reflects the condition of a sample surface layer. From the recorded X-ray spectra the atomic composition of the top layer of the sample can be estimated considering the individual X-ray yield for each spectral line and the chemical environment in which the atoms are situated.

X-ray spectra were recorded for different bone samples. The following elements were detected by their characteristic spectral lines carbon (C; Kα: 0.2774 keV), oxygen (O; Kα: 0.5249 keV), phosphor (P; Kα: 2.0134keV) calcium (Ca; Kα: 3.6905 keV, Lα: 0.3413 keV) [Oxford]. The peak in the spectra at 0.26 keV is a superposition of the Kα line of carbon and the Lα line of calcium. Calcium and phosphor are indicators for the mineral component of bone, since they are components of hydroxyapatite but not of collagen. Carbon is a component of collagen but not of hydroxyapatite, and oxygen is a component of both compounds. The collected information can be interpreted relatively by comparing the spectra from non-irradiated and laser irradiated parts of the same bone sample. A comparison between two different bone samples is only partly significant due to the natural variations in the bone composition.

X-ray fluorescence spectra were recorded for fresh bone which was irradiated in conjunction with water spray and dehydrated bone from the ethanol preparation which was irradiated in conjunction with a nitrogen gas jet. X-ray measurements were done at laser irradiated surfaces and at areas of the bone sample which were not laser irradiated. The five different EDX spectra presented in this chapter are summarised in table 5.2.

Table 5.2: Overview of presented EDX spectra

EDX Spectrum	Sample material	Area of sample	Measurement method
Figure 5.19	Fresh bone laser irradiated with additional water spray	Non irradiated surface	Average of 10 measurements each 30 s
Figure 5.20	Fresh bone laser irradiated with additional water spray	Laser irradiated surface	Long time measurement of ca. 40 minutes (2541 s)
Figure 5.21	Dehydrated bone laser irradiated with additional nitrogen gas jet	Non irradiated surface	Average of 5 measurements each 30 s
Figure 5.22a	Dehydrated bone laser irradiated with additional nitrogen gas jet	Laser irradiated surface	Long time measurement of ca. 150 minutes (9048 s)
Figure 5.22b	Dehydrated bone laser irradiated with additional nitrogen gas jet	Laser irradiated surface	Average of 5 measurements each 30 s

5.1.3.1 EDX Spectra of Fresh Bone

When comparing the spectra in figure 5.19 and 5.20 - two spectra of fresh bone, one spectrum from an untreated surface (5.19), the other spectrum from a surface of a laser incision (5.20) - it is only evident that the relative fraction of calcium and phosphor, as the indicators for hydroxyapatite, seems to have been reduced by the laser irradiation. The spectrum of the untreated surface displayed in figure 5.19 is an averaged spectrum calculated from 10 measured spectra with 30 s integration time each. The spectrum in figure 5.20 is a X-ray spectrum of the surface of the laser incision determined by one long time measurement with a duration of slightly over 40 minutes.
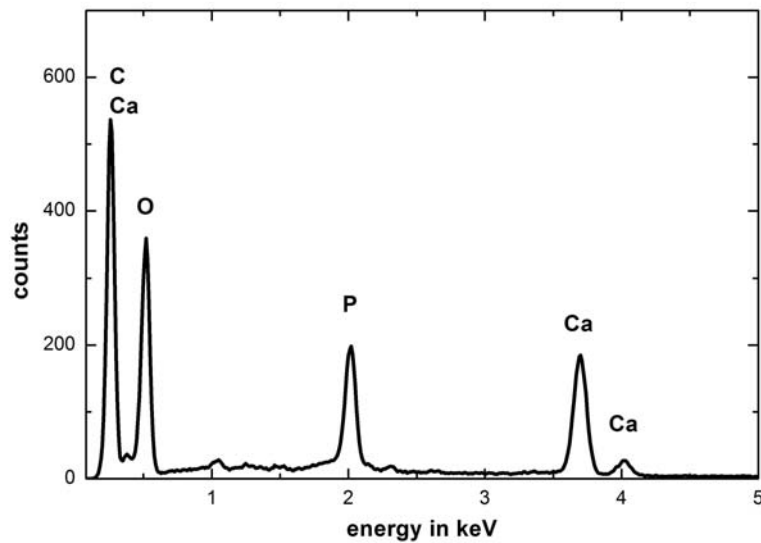
Figure 5.19: (EDX) X-ray fluorescence spectrum: untreated surface of fresh bone (average of 10 measurements; scanned area at 600 x magnification, each measurement 30 s integration time)
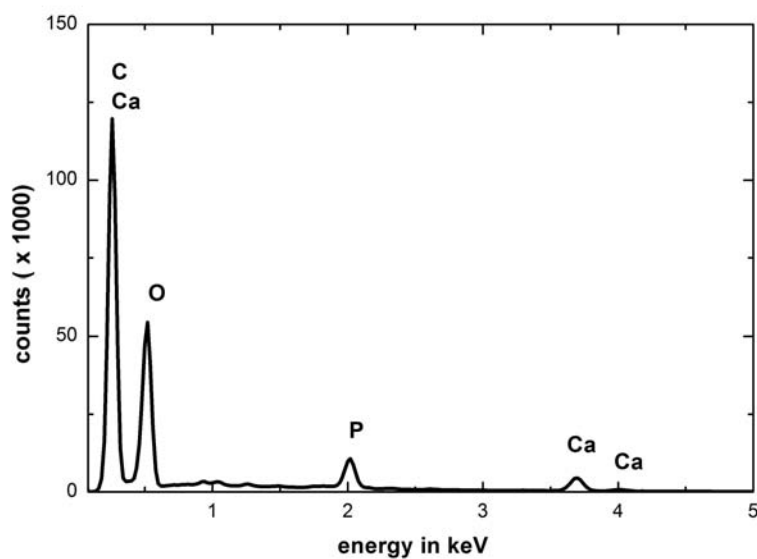
Figure 5.20: (EDX) X-ray fluorescence spectrum: surface of laser incision in fresh bone (one long-time measurement; scanned area at 2077x magnification, 2541 s integration time)

5.1.3.2 EDX Spectra of Dehydrated Bone (Ethanol Preparation)

Figures 5.21 and 5.22.a&b show EDX spectra of a sample dehydrated in ethanol prior to laser irradiation. While figure 5.21 depicts a spectrum of a non-irradiated area on the bone surface, figures 5.22.a&b display spectra from the surface of the laser incision (laser irradiated area). Spectra 5.21 and 5.22b show the average of five measurements of 30 s each, whereas spectrum 5.22a is a long-time measurement over 150 minutes.
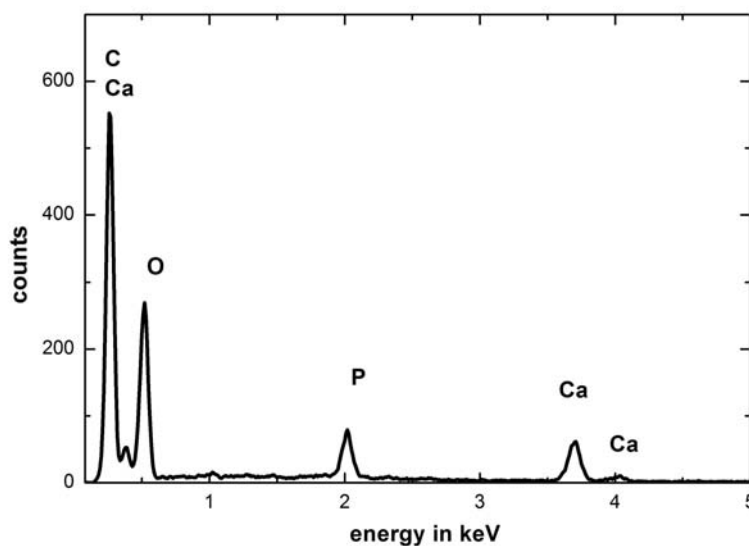
Figure 5.21: (EDX) X-ray fluorescence spectrum: non-irradiated surface of a bone from ethanol preparation (average of 5 measurements; scanned area at 600 x magnification each measurement 30 s integration time)

Figure 5.22a: (EDX) X-ray fluorescence spectrum: surface of laser incision in a bone from ethanol preparation (one long-time measurement) (scanned area at 3181x magnification, 9048 s integration time)
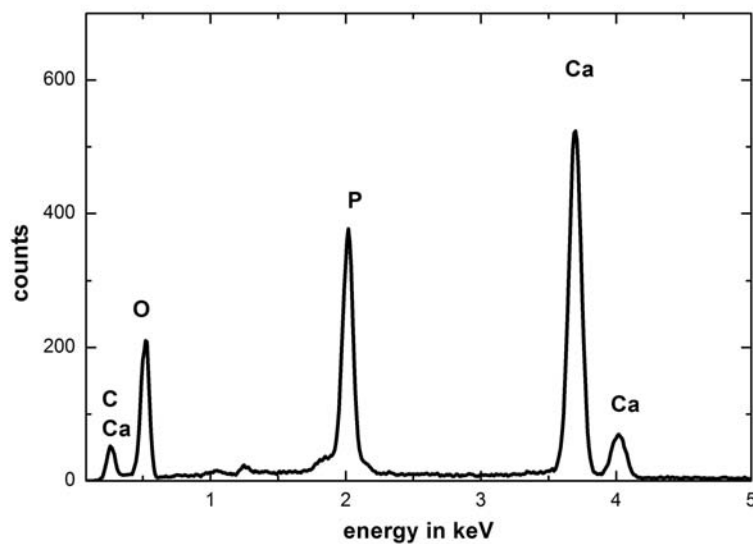
Figure 5.22b: (EDX) X-ray fluorescence spectrum: surface of laser incision in a bone from ethanol preparation (average of 5 measurements; scanned area at 1000 x magnification, each measurement 30 s integration time)

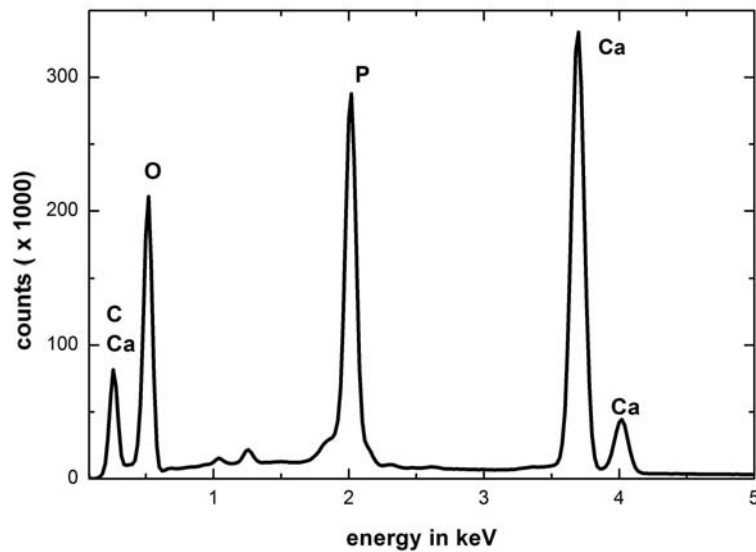The EDX spectra of the laser irradiated area (5.22.a&b) show a strong relative increase in the occurrence of the indicator elements for hydroxyapatite (phosphor and calcium) both in the long time measurement and the averaged spectrum compared to the non-laser irradiated surface of the bone sample from the ethanol preparation. With the included software package of the EDX detector (INCA), the relative atomic composition of the examined sample area can be calculated. The received data, when only including the four main detected elements, for the spectra 5.21 and 5.22.b is shown in table 5.3. The listed values show a distinct increase in the occurrence of all elements which are found in hydroxyapatite for the laser irradiated area of the dehydrated bone sample, especially of phosphor and calcium and less pronounced of oxygen, which however, is also found in collagen.

Table 5.3: Relative occurrence of the different elements in the examined area of the ethanol prepared bone sample (all values in atom-%, data retrieved from spectra in Fig. 5.21 and 5.22.b)

Measurement	Carbon	Oxygen	Phosphor	Calcium
Untreated surface 1	65,37	33,63	0,55	0,45
Untreated surface 2	63,71	33,95	1,12	1,22
Untreated surface 3	65,76	32,48	0,81	0,95
Untreated surface 4	62,18	35,56	1,07	1,18
Untreated surface 5	65,95	30,85	1,42	1,78
Average untreated surface	64,59	33,29	0,99	1,12
Laser incision surface 1	21,06	54,83	8,47	15,64
Laser incision surface 2	19,79	54,11	8,77	17,33
Laser incision surface 3	20,3	53,56	9,2	16,95
Laser incision surface 4	19,8	55,09	8,35	16,75
Laser incision surface 5	20,03	53,19	8,87	17,92
Average laser incision surface	20,19	54,16	8,73	16,92

The relative occurrence of the different atom species (table 5.3) derived from the EDX spectra in this chapter show an increase in the percentage of the indicator atom species for hydroxyapatite (phosphor and calcium) at the surface of the laser irradiated area of the bone sample dehydrated in ethanol.

5.1.3.3 Summary SEM Images and EDX Spectra

The recorded EDX spectra and the SEM images of the laser cuts in dehydrated bone show a layer of hydroxyapatite which was molten during the laser irradiation

and subsequently re-solidified at the end of the ablation process. During "dry" laser ablation temperatures are achieved which suffice to melt hydroxyapatite. All these signs - melting traces in SEM images and increase of calcium and phosphor signals in the EDX spectra – are absent for the "wet" laser ablation. This suggests much lower temperatures in this ablation regime.

5.1.4 Summary of the Dependence of the Ablation Process on the Tissue Water Content

The results of the incision depth and specific ablation energy presented in chapter 5.1.1 show that laser ablation of dehydrated compact bone without water spray is possible but far less effective compared to the ablation of fresh bone with the use of water spray. The ablation efficiency for pure hydroxyapatite is even clearly below the efficiency for dry bone. These findings support the process model of bone tissue ablation driven by micro-explosions caused by pressure build-up during the extremely fast evaporation of enclosed water in the bone tissue, which was introduced in chapter 3.2 for pulsed IR lasers. The fact that bone tissue can be removed from dehydrated bone samples implies that there is another - however less effective – ablation process channel. This competing ablation modus is based on the destruction, melting, and vaporisation of the bone matrix consisting of collagen and hydroxyapatite. Perhaps there is some kind of two component ablation process [Wil01] in which the collagen adopts the role of the water in normal (hydrated) bone, and its explosive decomposition drives the ablation of the bone tissue as a whole. Another possibility is the rapid melting of hydroxyapatite which creates large hydrodynamic forces due to the volume expansion of the material upon melting. This process was described by Fried et al. [Fri98] for the ablation of dental enamel with pulsed CO_2 lasers. It leads to the ejection of liquid droplets. Both possible ablation mechanisms need considerably higher temperatures and energy than the thermo-mechanical ablation due to water evaporation. That high temperatures are reached in the "dry" ablation of bone is documented in the re-solidified melting traces seen in the SEM images of the laser irradiations of dehydrated bone and

pure hydroxyapatite. These signs of melting are absent in the laser irradiated samples of fresh bone with additionally applied water spray.

The EDX spectra presented in chapter 5.1.3 imply that, in the case of laser irradiation of dehydrated bone, molten and re-solidified hydroxyapatite is deposited on the surface of the incision during the ablation process at temperatures above 1100°C to 1280°C. This explains the relative increase of the proportion of phosphor and calcium as markers for hydroxyapatite in the area of the laser incision in ethanol dehydrated bone. During the laser processing of fresh bone with a water spray the temperatures are much lower. The results presented in chapter 5.1 were partly reported in [Wer05].

5.2 Thermography

Bone tissue contains living cells which already get damaged by moderate temperature rises above 42 °C. Therefore it is important to know the temperature of a bone sample during laser irradiation. Measuring of the temperature at the actual ablation site is not a simple task because of the small volume of strongly heated material (beam diameter around 200 μm) and the short time scale of the laser induced heating (laser pulse duration between 1 and 80 μs in our experiments, time constant for thermal relaxation of bone tissue is around 25 μs for λ = 9.6 μm and 55 μs for λ = 10.6 μm). As a result, one can expect very steep temperature gradients and very fast temperature changes. To achieve reasonable spatial and temporal resolution, we used a fast IR camera "Flir SC 3000" with a quantum well infrared photo detector (QWIP). This work was done in cooperation with A. Brendemühl and Prof. Dr. T. Buzug from the RheinAhrCampus, a part of the University of Applied Science Koblenz. Prof. Dr. Buzug provided the SC 3000 IR camera for the thermal measurements. The results presented in this sub-chapter were also partly presented in [Bre05]. A short overview of thermal (black body) radiation and the working principle of the used QWIP detector of the IR camera is given in the Appendix.

5.2.1 IR Camera FLIR SC 3000

For the temperature measurements described in this sub-chapter, an IR camera (Flir SC 3000) with a QWIP GaASs/AlGaAa detector was used. The detector chip is cooled down to 70 K with a Stirling cooler. The spectral range of the camera is shown in figure 5.23 [SC3000]. The main sensitivity region lies between 8 and 9 µm. However, there is still some sensitivity at wavelengths above 10 µm. So, the camera was protected from stray light from the laser radiation (10.6 µm) with CaF_2 windows. The parameters of the camera are summarised in table 5.4.
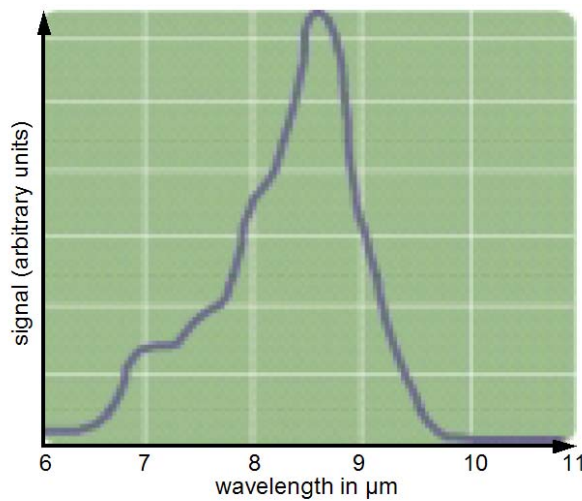
Figure 5.23: (Nominal) spectral sensitivity of the QWIP detector in the Flir SC 3000 camera (taken from [SC3000])

Table 5.4: Specifications of Flir SC 3000 IR thermal camera [SC3000]

Parameter	Value
Detector	GaAs QWIP detector
Resolution	320 x 240 Pixel with 14 bit
Spectral Range	7.5 – 11 µm (cut-off filter for λ < 7,5 µm) maximal sensitivity between λ= 8 – 9 µm
Frame Rate	50 Hz (for 320 x 240 pixel)
Temperature Ranges	a) -20 to 80°C; b) 10 to 150 °C c)100 to 500 °C, extendable to 1500°C
Accuracy	±1 % (or 1°C) for temperature range a) and b) ±2 % (or 2°C) for temperature range c)
Detector Integration Time	Range a) up to 80°C: 3 ms Range b) up to 150°C: 1.5 ms Range c) up to 500°C/1500°C : 0.5 ms
Thermal Sensitivity	< 0.02°C @ 30°C

The temperature scale of the camera is calibrated with an isothermal "cavity radiator" which is uniformly heated and resembles a black body radiator as good as practically possible. The emissivity ε can be adjusted in the measurement software (THERMA Cam Research) for different observed materials (surfaces).

5.2.2 Experimental Set-Up
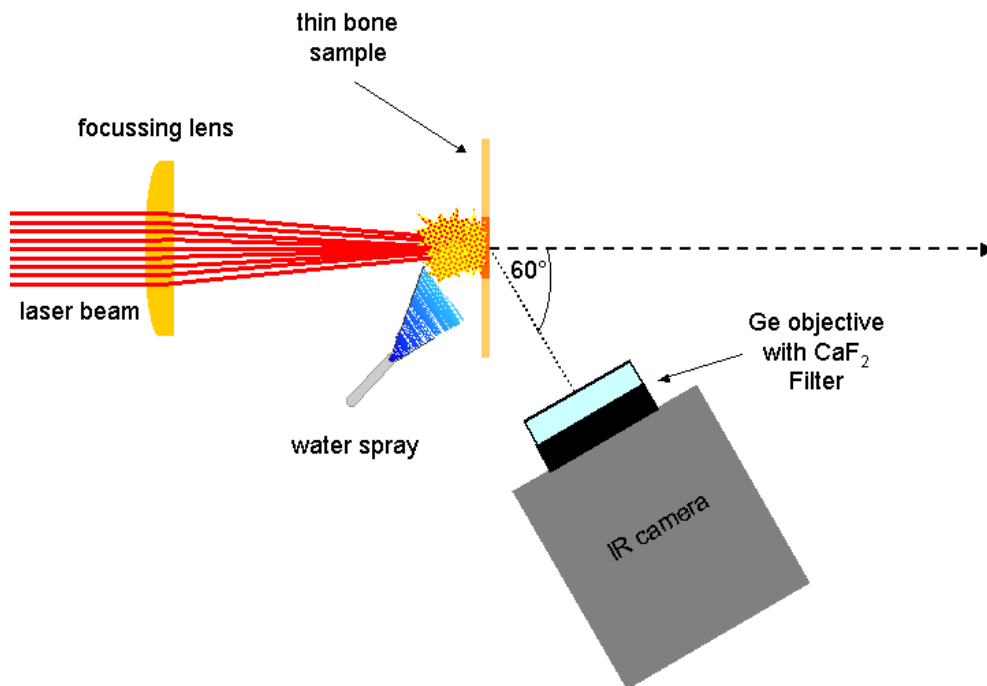
Figure 5.24: Experimental set-up for the temperature measurements during laser ablation

The experiments for the thermal measurements during the laser induced ablation of bone samples were conducted with the TEA CO_2 laser. The wavelength of the laser was tuned to 10.6 µm to minimise the response of the IR camera directly to the laser radiation. The laser beam focus diameter (@ $1/e^2$ level) was 225 µm, the pulse energy $E_{pulse} \approx 30$ mJ.

The measurements from which meaningful conclusions could be drawn were taken in the set-up shown in figure 5.24 where the camera monitored the backside of a thin bone sample, whereas laser pulses impinged on the front side of the bone

sample. When monitoring the front side of the bone during the laser ablation, it is not possible to clearly assign the temperature measured with the IR camera to the temperature of the bone itself. The measured temperature can originate from thermal radiation emitted from the overheated ablation plume in front of the bone. So, the temperatures measured by the monitoring of the front side of the bone sample may be overestimated. The temperature measured at the sample backside rose while the ablation depth increased with irradiation time. The maximal temperature was reached at the moment, when the laser broke through the bone sample. This temperature can be directly related to the ablation process. The difficulty in obtaining a meaningful measurement of the ablation temperature at the bone surface itself is also due to the short time scale of the ablation process compared to the detector integrating time. Moreover, the temporal temperature rise is very fast. For tissue water, which is "hermetically" enclosed in the bone matrix to 80%, the temperature at which the ultimate tensile strength of bone (100 MPa) is reached is about 320°C [Iva05]. The assumption of the pulse duration as a time scale for this temperature rise is rather conservative since the radiant exposure threshold is reached with the used pulse energy already during a fraction of the laser pulse. If one assumes, however, that the temperature rise time is 1 µs (full pulse duration for the TEA CO_2 laser), the resulting lower limit for the rate of temperature increase is $300 \cdot 10^6$ K/s. The shortest possible integration time for the QWIP detector of the used IR camera is, with 0.5 ms, much longer than the pulse duration and temperature relaxation time constant. As a result of this estimation, it is clear that even with this fast thermal camera only an average temperature can be measured. The same is valid for spatial resolution. It was about 177 $\times$ 105 µm in our experimental set-up. The spatial resolution is different for the horizontal and vertical axis since the bone sample was viewed from an angle in the horizontal axis (see figure 5.24).

The temperature evolution during the actual physical ablation process or temperature distribution in the ablation volume cannot be tracked with satisfying temporal and spatial resolution. However, the results reported below allow important

practical conclusions since the physiological temperature effects in the tissue adjacent to the laser interaction volume are of integrative character.

5.2.3 Results of Thermal Measurements

Figures 5.25.a and 5.26.a display typical spatial temperature distributions at the back side of thin bone samples directly before laser breakthrough during laser spot irradiation (drilling without beam movement). The laser worked at a 50 Hz repetition rate with pulse energies of about 30 mJ (1.5 W average power). For the temperature distribution shown in figure 5.25.a an air jet was directed at the front surface of the bone sample, and for figure 5.26.a a water spray was directed at the front surface of the bone sample. Figures 5.25.b and 5.26.b show the same temperature distributions in a colour-coded 2D view with cross-sections of the temperature distributions $T(x)$ and $T(y)$ as cross-sections through the temperature maximum.
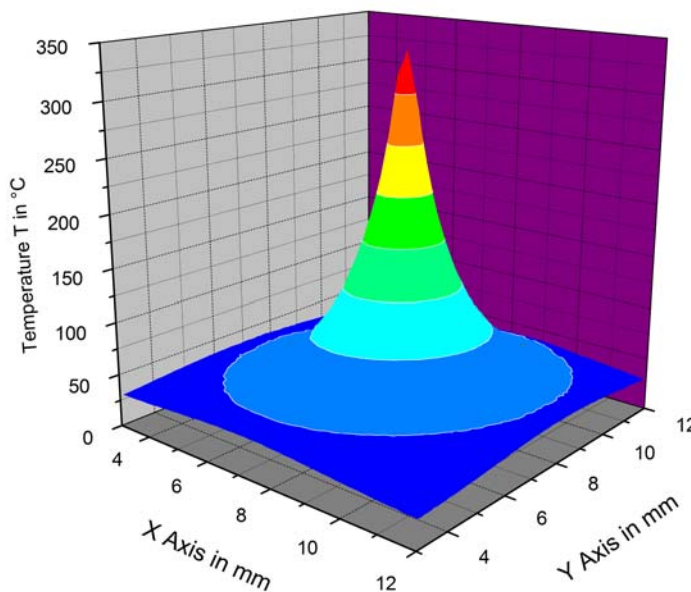
Figure 5.25.a: Temperature distribution $T(x,y)$ during laser drilling (no beam movement) at backside of bone sample (thickness 1 mm) directly before breakthrough (T_{max} = 344°C), air jet applied to irradiation spot on front side
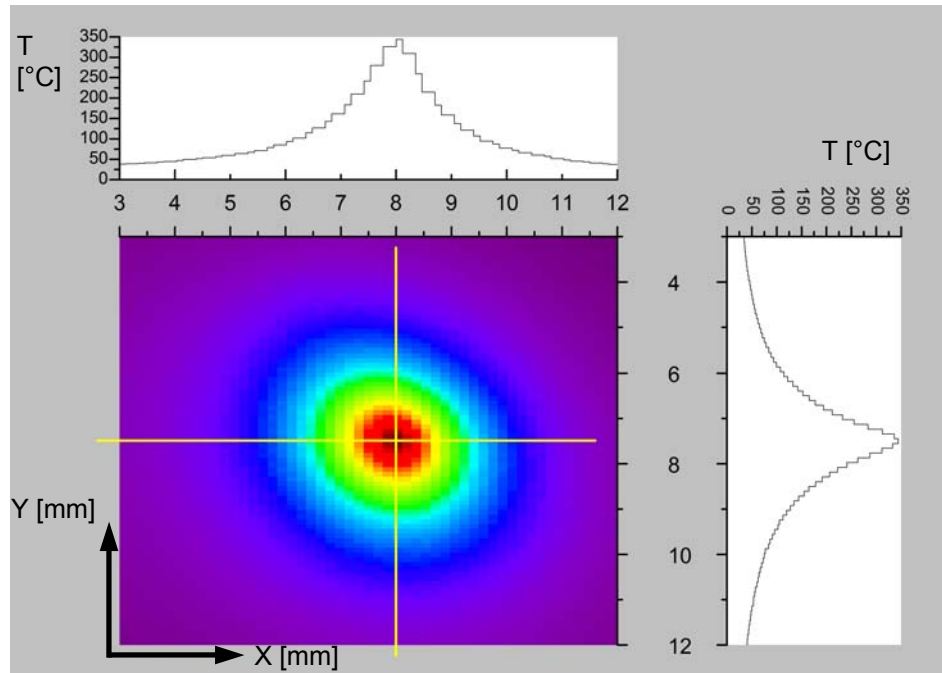
Figure 5.25.b: Colour-coded temperature distribution T(x,y) during laser drilling (no beam movement) at backside of bone sample (thickness 1 mm) directly before breakthrough (T_{max} = 344°C), air jet applied to irradiation spot on front side, temperature distributions along x and y axis (all spatial axes in mm)
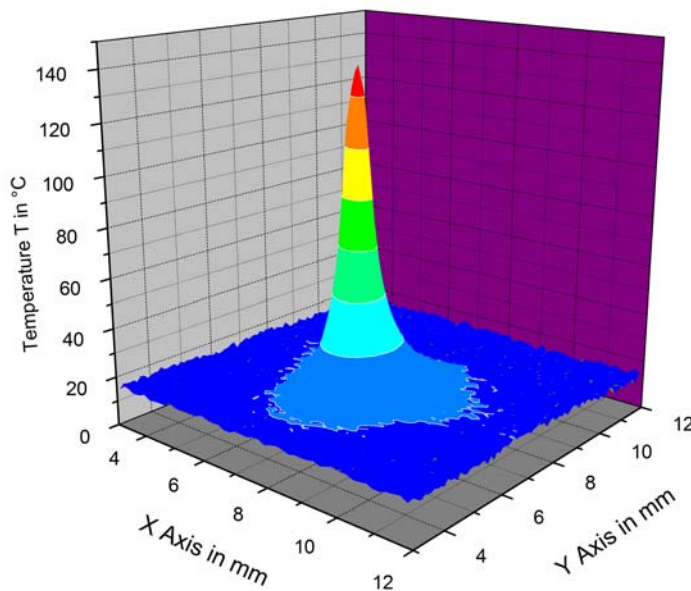
Figure 5.26.a: Temperature distribution T(x,y) during laser drilling (no beam movement) at backside of bone sample (thickness 1.3 mm) directly before breakthrough (T_{max}= 142°C), water spray applied to irradiation spot on front side
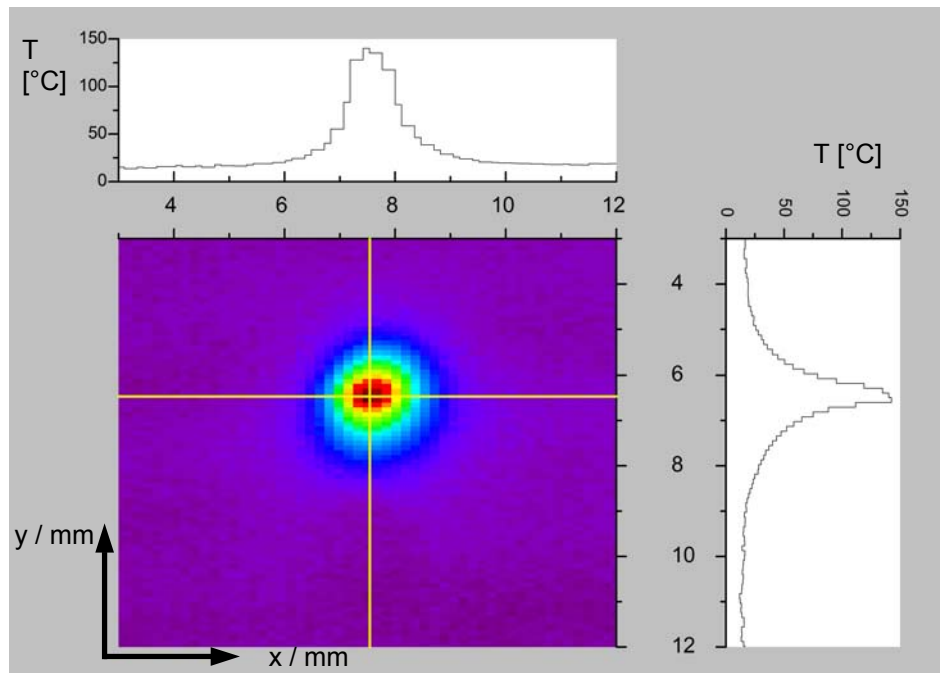
Figure 5.26.b: Colour-coded temperature distribution T(x,y) during laser drilling (no beam movement) at backside of bone sample (thickness 1.3 mm) directly before breakthrough (T_{max} = 142°C), water spray applied to irradiation spot on front side, temperature distributions along x and y axis (all spatial axes in mm)

As expected, the temperature distribution for the irradiation with an additional water spray has a clearly reduced maximum and the spatial distribution is considerably narrower.

The temperature distribution for the laser point irradiation with air jet usage has a maximum of 344 °C and a full width at half maximum (FWHM) of 1.63 mm in x-direction and 1.69 mm in y-direction. For the laser point irradiation with water spray usage the maximum is 142 °C, and the FWHM is 0.96 mm in x- and 0.83 mm in y-direction. According to these measurements, the temperature distributions have much larger dimensions than the laser beam profile with a diameter of 225 μm ($1/e^2$ level). This spread of the temperature distribution far beyond the laser beam distribution is expected due to thermal conductivity during the irradiation time. Both temperature distributions are recorded in the sensitivity range of 0° to 500°C (see table 5.4).

The detector integration time for this setting is 0.5 ms. The frame rate of the camera is 50 Hz, which corresponds to a time of 20 ms between measurements. No useful synchronisation of the camera and the laser repetition rate could be established. Thus, the data presented here indicate average temperatures during an interval of 0.5 ms with a temporal resolution of 20 ms. This means that the actual instantaneous temperature can be much higher than the values recorded by the QWIP detector that are presented here. The cell damage depends, however, not only on the temperature itself but also on the duration of the temperature rise. The damage occurrence can be approximated with Arrhenius' equation [Nie96].

$$\ln\left(\frac{C(t)}{C_0}\right) = -A\int_0^t \exp\left(-\frac{\Delta E}{RT(t')}\right)dt' \equiv -\Omega \qquad (5.1)$$

Here C_0 is the initial concentrations of the cells (or molecules), $C(t)$ the concentration of undamaged cells at the time t, A Arrhenius' constant, R the universal gas constant, and ΔE and Ω specific tissue constants. The local degree of tissue damage $C_d(t)$ is given by

$$C_d(t) = \frac{C_o - C(t)}{C_0} = 1 - \exp(-\Omega) \qquad (5.2)$$

With the knowledge of the value of the constant Ω, it is possible to predict the probable damage percentage $C_d(t)$ after a time t.

From this equation it may be concluded that a strong temperature increase on the time scale of µs is probably less damaging than a weaker long-term heating of the adjacent tissue. The results from laser spot irradiations presented above show a localised heat accumulation already at a 50 Hz laser pulse repetition rate. At 50 Hz, the time between two pulses is 20 ms, which is about 360 times longer than the (typically used) value for the thermal relaxation time of $\tau_T \approx 55$ µs for bone irradiated with laser pulses at 10.6 µm. This behaviour indicates a much longer effective thermal relaxation time like it is proposed for example by Choi and Welch [Cho01] and already mentioned in chapter 3.2 (see figure 3.1).

Further temperature measurements have shown that the temperature can be substantially reduced by scanning the laser beam over the bone sample during

irradiation. This is already done "by default" in the laser osteotomy technique developed in our group. For a set of temperature measurements during the scanning of the laser beam over the bone sample, a scanning speed of v = 2 mm/s was chosen. The corresponding overlap factor was n $\approx$ 2.8 (= 112.5 µm · 50 Hz / (2 mm/s)). This value is rather high compared to the usual overlap factors used with the TEA CO_2 laser, which are around n $\approx$ 1. The lengths of the scanning lines in the experiments were chosen to be at least 10 mm with a bi-directional movement. This means that the laser beam passes a point in the middle of the scanning line at an interval of 5 s. The thickness of the used bone samples were about 1 mm. The temperature measured during laser irradiation in combination with an air jet was about 120°C just at laser breakthrough and about 30°C for a laser irradiation combined with a water spray. Both experiments were conducted at room temperature (22°C). This equals a detected temperature rise of 8 K under optimised irradiation conditions.

Conclusions concerning the physiological effects of the laser induced heating of the bone tissue may be drawn qualitatively. Laser irradiations in fresh bone with fast multi-pass laser beam scanning and application of a water spray show no visual signs of thermal damage. Histological examinations and in-vivo healing studies of such laser incisions yield good biological results with only minimal damage to cells adjacent to the cut. The small rises of the measured temperature of about 8 K for an irradiation under these optimal conditions underline the good bio-compatibility of the procedure. (It has to be stated that the instantaneous temperature rise may actually be much higher due to the restricted temporal resolution of the camera. However, an increase of the temperature over such a short time will not have a pronounced effect due to the considerations in connection with Arrhenius' equation.)

Although the temporal resolution of the camera is insufficient to examine the actual physical ablation process or for a meaningful measurement of the thermal relaxation time, the temporal resolution, i.e. the time scale in which a temperature drop after an impact of a laser pulse can be monitored with the camera, was tried to be estimated. Figure 5.27.a shows the temperature response after 8 laser pulses on

a bone sample without water spray. This time the sample was observed from the front side (irradiation side). The laser pulse repetition rate was 1 Hz. Here only the temporal development should be regarded. One can see eight temperature peaks resulting from eight individual laser pulses with a very steep rise and significantly slower decline of the temperature.
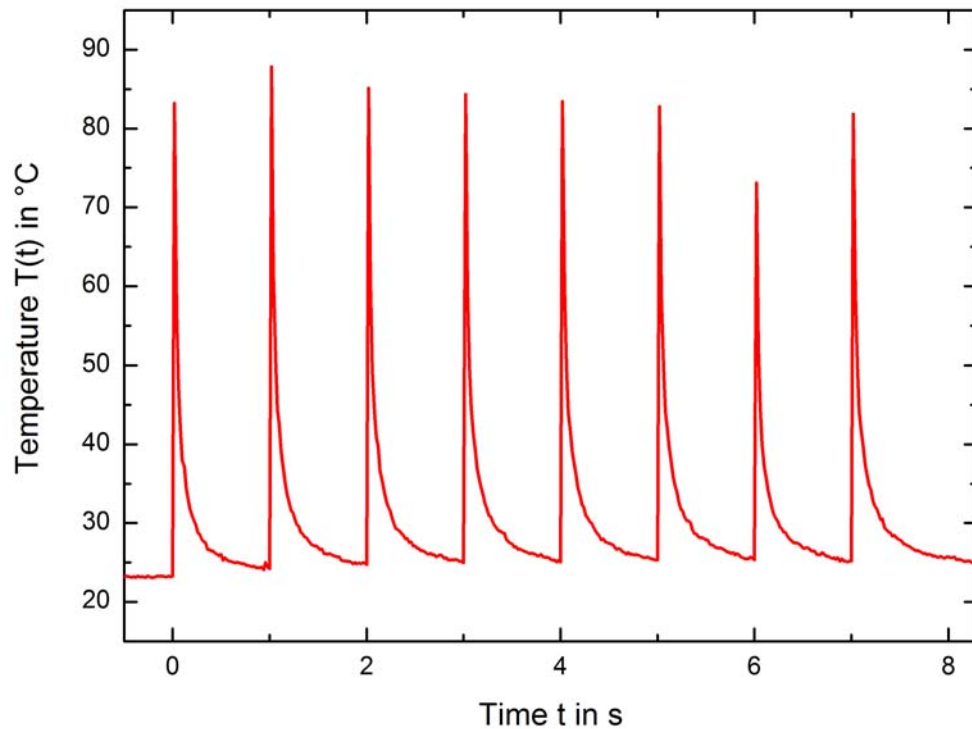
Figure 5.27.a: Temporal temperature distribution from eight laser pulses on a bone sample at a laser repetition rate of 1 Hz, the sample was observed from the front side, no water spray applied

Figure 5.27.b depicts the normalised and averaged temperature decline of the eight laser induced temperature peaks against time.

The measured temperature decline in figure 5.27.b can be fitted quite well with a second order exponential decay. The two exponential functions $\exp(-t/t_i)$ have decay constants of $t_1 = 174$ ms and $t_2 = 22$ ms. These values are quite large and cannot be interpreted in relation to the physical ablation process and probably are dominated by the time constants of the detector and data processing system.
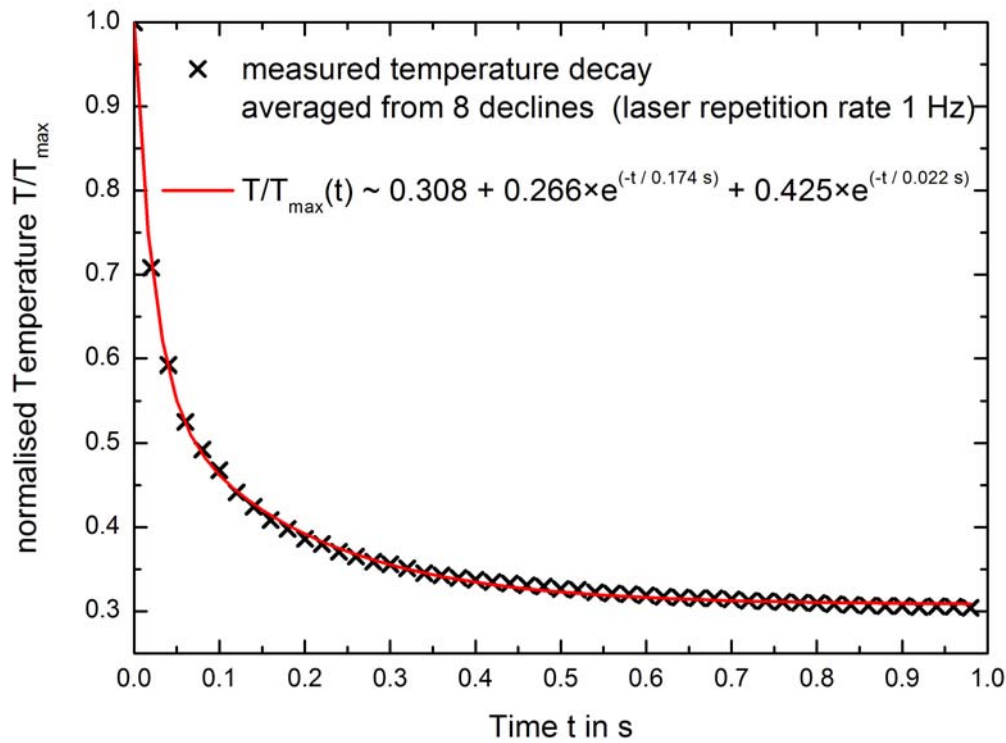
Figure 5.27.b: (×) Averaged and normalised temperature decline of the eight temperature peaks visible in figure 5.27.a; (()) fitted with a second order exponential decay

5.2.4 Summary of Thermal Measurements

The following conclusions can be drawn from the thermal measurements. With the use of a fine water spray and the "fast" laser beam scanning technique, physiologically damaging "long-lasting" temperature rises of the surrounding bone tissue can be avoided during the ablation process. The measurements indicate that the cooling of the bone after heating with the laser pulses is much slower than indicated by the usually applied thermal relaxation time constant. This confirms the results of the theoretical considerations by Choi et al. [Cho01]. A significant estimate (measurement) of the thermal relaxation time constant of bone irradiated with a CO_2 laser cannot be made due to the insufficient temporal resolution of the available detector system.

5.3 Summary Chapter 5

The first part of chapter 5 presented experiments on the verification of the thermo-mechanical ablation model. The results of the analysis of laser irradiated bone samples with different water contents done with optical measurements, SEM imaging, and EDX analysis supported the thermo-mechanical process model for ablation of bone tissue with pulsed CO_2 lasers. In the second part of this chapter, thermal measurements during the laser ablation of bone samples with a pulsed TEA CO_2 laser recorded with an IR camera were presented. The obtained data showed a distinct local heating even at pulse repetition rates of only 50 Hz. This indicates that the time scale for the complete cooling of the bone tissue is much longer than the conventionally used thermal relaxation time. The maximal recorded temperature and the area of heating could be significantly reduced by the use of a fine water spray and the scanning of the laser beam over the bone sample. It could be shown that with the use of the multi-pass beam scanning technique, combined with a fine water spray, bone can be laser processed at temperatures which are biologically compliant for the sensitive biological structures in the bone.

6. Different Laser Types and Scanning Techniques

In the first part of this chapter (6.1), experiments carried out with alternative laser sources for hard tissue ablation are presented. A XeCl excimer and an electro-optically q-switched CO_2 laser are utilised for ablation experiments with compact bovine bone samples. The results are compared with the two "standard" laser systems used in this thesis (MTL 3 TEA and the SC x 30 slab CO_2 laser). The results will be discussed with regard to the ablation efficiency, ablation depth and cutting rate.

The second part of this chapter (6.2) deals with the comparison of different beam scanning techniques and the influence of a dilatation of the incision on the ablation efficiency for irradiations with the SC x 30 slab CO_2 laser.

6.1 Ablation of Bone with Different Laser Types

In this sub-chapter, experiments with two additional alternative laser systems for hard tissue processing are presented. The experiments with the XeCl excimer laser (TUI laser Excistar S) were done to evaluate the possibility and efficiency of bone ablation with a UV laser in general. The measurements with the q-switch CO_2 laser were necessary to evaluate the use of a short pulsed CO_2 laser system with small pulse energies and high repetition rates in contrast to the TEA CO_2 laser system with relatively high pulse energies and low repetition rates. The used q-switched CO_2 laser (Deos Gem Q 3000) is a sealed system without gas consumption and

easier to handle than the TEA CO_2 laser. The results obtained with the two alternative laser systems will be compared with the results of the two "standard" laser systems introduced in chapter 4 (Rofin Sinar SC x 30 and Edinburgh Instruments MTL3-GT). The parameters for all four laser sources are summarised in table 6.1.

Bovine bone samples were irradiated in the manner described in chapter 4.1 with the drive-stage set-up. Fresh bone samples and a water spray during the irradiation were used to obtain optimal ablation results. With both alternative laser systems, it was possible to obtain visually clean cuts in compact bovine bone if a water spray was applied during the irradiation.

Table 6.1 Laser parameter used in the described experiments

Laser System	TUI Excistar S XeCl-excimer laser	Deos Gem Q 3000 q-switch CO_2 laser	Rofin-Sinar SC 30 CO_2 slab laser	Edinburgh Instr. MTL 3 GT TEA CO_2 laser
Wavelength	0.308 µm	9.25 µm	10.6 µm	9.6 µm
Pulse Duration	60 – 80 ns	150 ns (FWHM) + tail; $\tau_{complete} \approx 1$ µs	80 µs (FWHM)	45 ns (FWHM) + tail $\tau_{complete} < 1$ µs
Pulse Rep. Rate	500 Hz	1000 Hz *	100Hz	35 Hz
Average Power	3.2 W	8.3 W	6.85 W	1.44 W
Pulse Energy	6.4 mJ	8.3 mJ *	68.5 mJ	41 mJ
Focus Radius	170 µm ** (estimated)	34 µm (@1/e^2) (calculated)	60 µm (@1/e^2) (calculated)	130 µm (@1/e^2) (calculated)
Rad. Exposure	7.05 J/cm^2	229 J/cm^2	600 J/cm^2	78 J/cm^2
Irradiance	100 MW/cm^2	848 MW/cm^2 ***	7.5 MW/cm^2	780 MW/cm^2 ****

*The effective repetition rate for the Gem Q3000 can be calculated from the RF-gate frequency 1 kHz and the q-switch frequency 20 kHz. The RF-gate duty cycle was set to 10 %. This means that the RF-discharge for excitation of the laser medium with a frequency of 1 kHz is repeatedly "on" for 100 µs and then "off" for 900 µs, which equals an "on" time of 10 %. During this 100 µs RF-gate "on" window, two laser pulses (temporal distance of 50 µs) were emitted since the q-switch frequency was set to 20 kHz. The bone sample was moved with a velocity of 40 mm/s transversely to the laser beam. In 50 µs, which was the time between the two pulses emitted in one RF-gate "on" window, the sample was only moved about 2 µm. This means that the two pulses virtually impinge on the same spot of the sample (focus radius $w_f = 34$ mm). Thus, the two pulses in one RF-gate "on" window are counted as one "effective" pulse with double pulse energy. The resulting "effective" repetition rate was 1 kHz, which is equivalent to the frequency of the RF-gate (one whole cycle takes 100 µs "on" +900 µs "off" = 1 ms = (1 kHz)$^{-1}$.

** The focus radius is quite large due to low quality multimode beam. The focus radius was estimated based on comparisons of the cut widths to CO_2 laser induced cut widths.

*** calculated with time scale $\tau_{effective} = 0.270$ µs; in this time, 50 % of the pulse energy is concentrated

**** calculated with time scale $\tau_{effective} = 0.100$ µs; in this time, 50 % of the pulse energy is concentrated

In figure 6.1, the average ablation depth δD per pulse for the four compared laser systems is plotted against the incision depth D. In figure 6.2 the average cut rate R $(= D \cdot L_{cut} / N_{pulse})$ is presented. Although the average ablation depth δD per pulse seems to be the obvious parameter for a comparison of the ablation potential of different laser sources, the large variation of focal diameters (from 68 to ca. 340 µm) of the laser systems used in the study has to be taken into account. The average cut rate R per pulse (defined in equation 4.4) offers a better comparison parameter for different laser set-ups with different focal sizes.
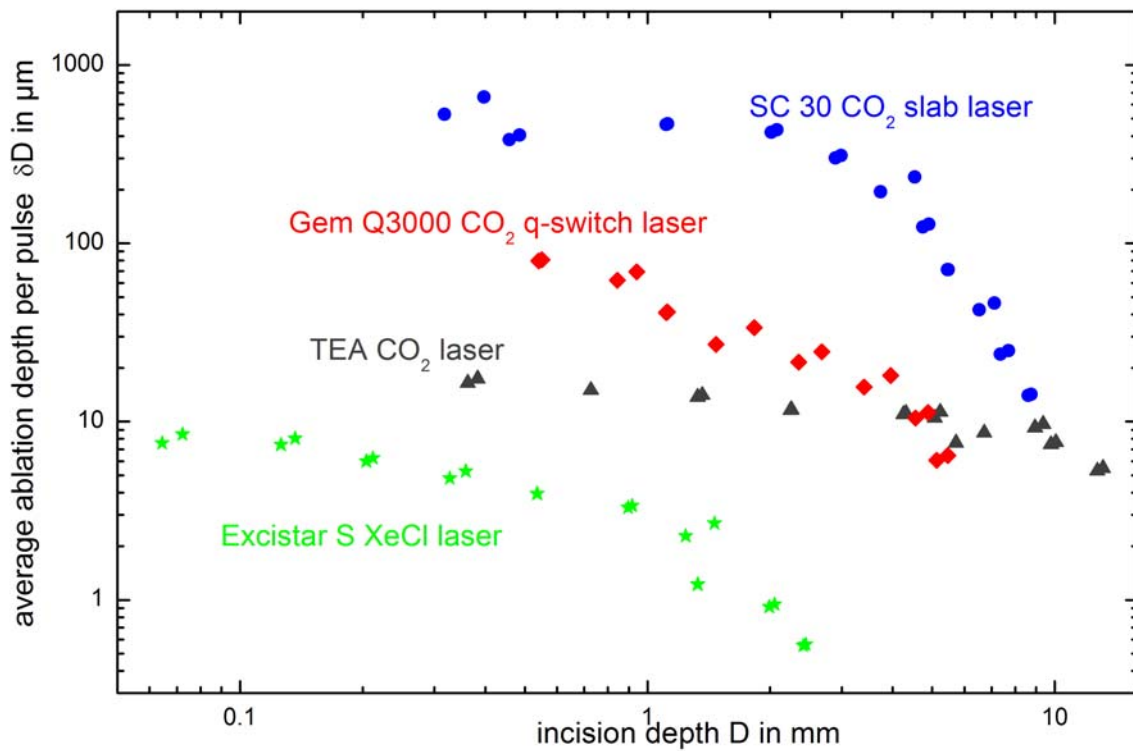
Figure 6.1: Average ablation depth per pulse δD/pulse in µm against incision depth D in mm for the four investigated laser types
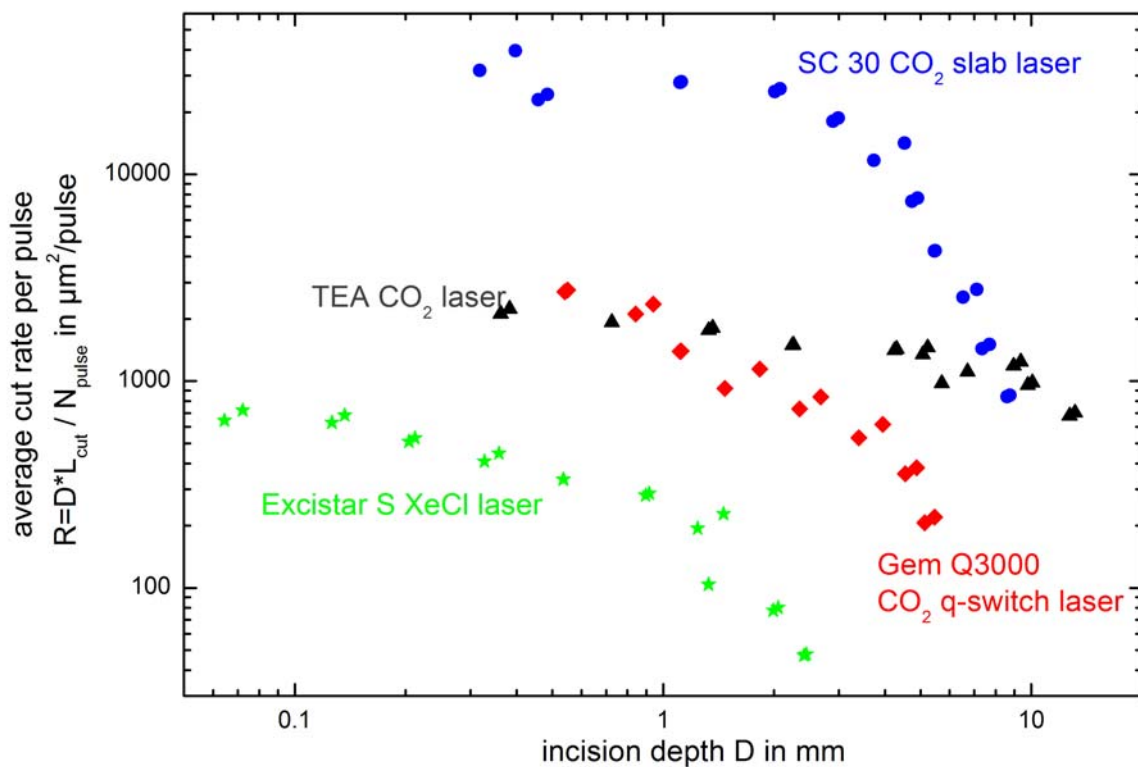
Figure 6.2: Average in cut rate R in μm^2/pulse against incision depth D in mm for the four investigated laser types

The ablation depth per pulse for the q-switch CO_2 laser lies between the ablation depth per pulse of the slab- and the TEA CO_2 laser. For the slab and q-switch CO_2 laser as well as the excimer laser, the ablation depth per pulse exhibits an especially distinct reduction with increasing incision depth. For the excimer and the q-switch CO_2 laser this behaviour already starts at low incision depths of about 1 mm, whereas for the slab CO_2 laser the sharp decrease in ablation efficiency starts around 4 mm. For a cut depth of up to 4 to 5 mm, the ablation depth per pulse for the q-switch CO_2 laser is superior to the TEA CO_2 laser. When looking at the average cut rate R per pulse the situation is different. For incision depths of up to 1 mm, the TEA and the q-switch CO_2 lasers have the same average rate, while the TEA laser system is superior for deeper cut. The difference in the behaviour of the two parameters for the two laser systems is due to the small focus diameter of the q-switch CO_2 laser (68 μm @ $1/e^2$ level). This creates a high radiant exposure and so high ablation depth per pulse despite the small pulse energy of 8.3 mJ, but it

does not achieve high cut rates. For incisions beyond 4 to 5 mm depth the TEA laser becomes superior in both assessed parameters. The ablation with the slab CO_2 laser is much more efficient initially but also becomes less effective compared to the ablation with the $TEAcCO_2$ laser at around 7 mm cut depth.

Furthermore, it is interesting to compare the specific ablation energy against the incision depth for the four systems (figure 6.3). The slab CO_2 laser is superior (i.e. lower specific ablation energy) to the other systems up to an incision depth of about 6 mm. For the deeper incisions, the TEA CO_2 laser needs less energy.
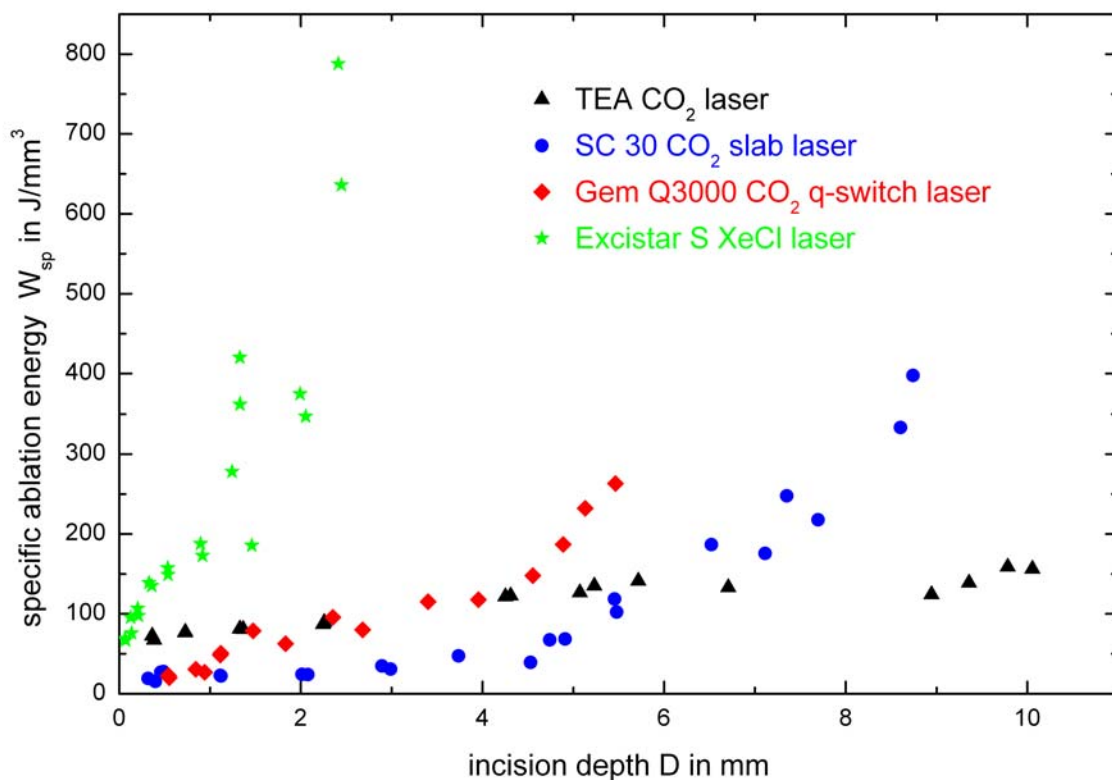
Figure 6.3: Specific ablation energy in J/mm³ against incision depth D in mm for the four investigated laser types

The XeCl laser ablates less efficiently than the other three lasers examined, irrelevant if one looks at the ablation depth per pulse, cut rate, or the specific ablation energy. A sharp reduction of ablation efficiency with depth can be seen in figures 6.1, 6.2, and 6.3. It is possible that an excimer laser system with a better

beam quality i.e. better focusability and higher pulse energies could achieve somewhat higher ablation rates. However, such a system was not available for the tests. And the data from the literature [e.g. Mur04, Jah92] indicate that excimer laser systems are generally much less effective for bone processing than CO_2 lasers.

To summarise the results, it can be said that, from the four laser systems investigated in these experiments, the slab ($\tau_{FWHM} \approx 80$ µs) and the TEA CO_2 laser ($\tau_{complete}$ <1 µs) are the laser systems that are suited best for the ablation of bone tissue. The slab system ablates more effectively than the TEA laser system up to incision depths of about 6-7 mm. With increasing incision depth the TEA laser system is clearly the most efficient laser system tested here. The qualitative physical explanation for this behaviour was given in previous publications of our group [Iva05, Afi04]. The slab CO_2 laser is very convenient and offers the highest average power. With a cut dilating scanning technique, which will be described in the following sub-chapter, much deeper cuts can be achieved with the slab CO_2 laser, i.e. with CO_2 laser pulses with durations of about 80 µs. The introduced q-switch system could possibly be used for micro-surgery interventions due to its fine cuts and the small laser head size.

6.2 Ablation of Bone with Different Scanning Techniques

One of the drawbacks of the laser osteotomy is the limitation in incision depth. There are two main energy loss mechanisms which limit the achievable depth. The first is the growing heat diffusion from the increasing surface area of the incision [Iva00]. The second is the increasing absorption in the ablation debris which is confined in deeper cuts [Iva05, Mit02, Maj98]. The limitation of the incision depth can be partly bypassed by artificially increasing the width (dilatation) of the incision with a technique called "wobble". This concept has been introduced to laser osteotomy by our group [Her01, Mit02, Afi04]. In this scanning technique an additional fine and fast circular movement of the laser beam focus is superimposed

to the "regular" trajectory of the laser beam. This produces a spiral-like movement of the laser focus on the bone tissue sample and with that a broader cut and an increased maximal incision depth.

6.2.1 Wobble vs. Line Cuts

In this section, laser incisions with an optimised set of wobble parameters, are compared to standard line cuts with simple linear movement of the laser beam over the sample. For this experiment the SC 30 slab CO_2 laser was used in combination with the Arges Elefant 20 laser beam scanner. The following laser parameters were applied: pulse duration τ_{FWHM} = 80 µs, pulse energy E_{pulse}= 70 mJ, pulse repetition rate f = 200 Hz (average laser power <P> ≈ 14 W). The beam was focussed after the scanning mirrors with a F = 163 mm flat field lens down to a focus radius w_f ≈ 80 µm (@1/e^2 level). The linear scanning velocity was v_{linear} = 40 mm/s. For the circular wobble movement a radius R_{wobble} = 0.4 mm and a wobble frequency f_{wobble} =135 Hz were chosen. These wobble parameters were empirically determined in series of systematic optimisation measurements, which will not be described here for the sake of shortness. They yield the deepest cuts when combined with our "standard" bone cutting parameters.

In one experimental sub-series presented here, the beam focus was situated on the surface of the bone sample; in another sub-series, the focus was positioned 5 mm beneath the surface. The positioning of the beam waist under the surface of the material is a known technique in material processing. It is advantageous to adjust the focus position in a way that the radiation exposure is reduced at the surface where the ablation process is most effective anyway but increases at a depth where the ablation efficiency drops. For the used set-up, the focus radius was w_f ≈ 80 µm and the Rayleigh length is z_R ≈1.44 mm. With a pulse energy of about 70 mJ, the radiant exposure in the focus was Φ(focus) ≈ 348 J/cm^2 and 5 mm from the focus (at the bone surface for Δz = 5 mm) $\Phi(\Delta z$ = 5 mm) ≈ 27 J/cm^2. The radiant exposure 5 mm from the focus was still well above the threshold, so effective ablation did take place.

Altogether, four series of experiments were carried out (wobble cuts with *Δfocus* = 5 and 0 mm and line cuts with *Δfocus* = 5 and 0 mm). Each series included a set of at least eight incisions with increasing depth *D* (i.e. increasing number of passes N_{pass}). Cortical bone samples from one piece of bovine femur bone, prepared as explained in chapter 4.1, were used for all experiments.

In figure 6.4, the grey trace shows the beam trajectory (only one pass) on the bone sample by application of the wobble technique. The black dots correspond to the places where laser pulses impinge.
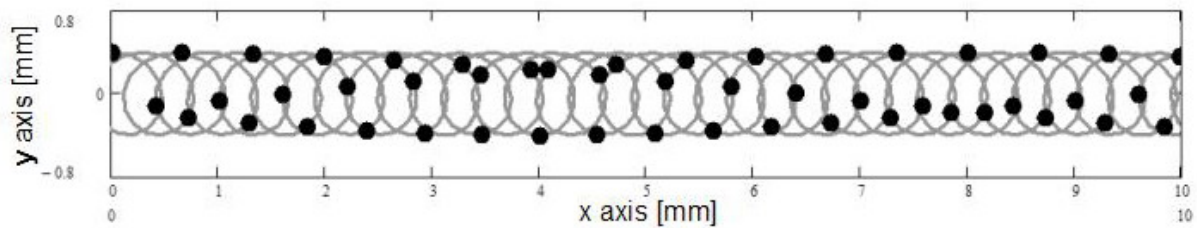
Figure 6.4: Wobble trace with v_{linear} = 40 mm/s; R_{wobble} = 0.4 mm; f_{wobble} = 135 Hz, laser repetition rate *f* = 200 Hz, beam spot radius $w_f \approx$ 80 µm, $w(\Delta z = 5\ mm) \approx$ 289 µm (black dots represent position of laser pulses)

The triggering of the laser was not synchronised with the scanning movement. Therefore, at each pass a slight offset between the laser pulse positions occurred. This was desired since a continuous filling of the whole cut area after many passes over the bone sample was finally produced.

In the following two figures (6.5 and 6.7) the average cut rate per pulse *R* and the specific ablation energy W_{sp} are shown for the four different sets of experimental parameters.
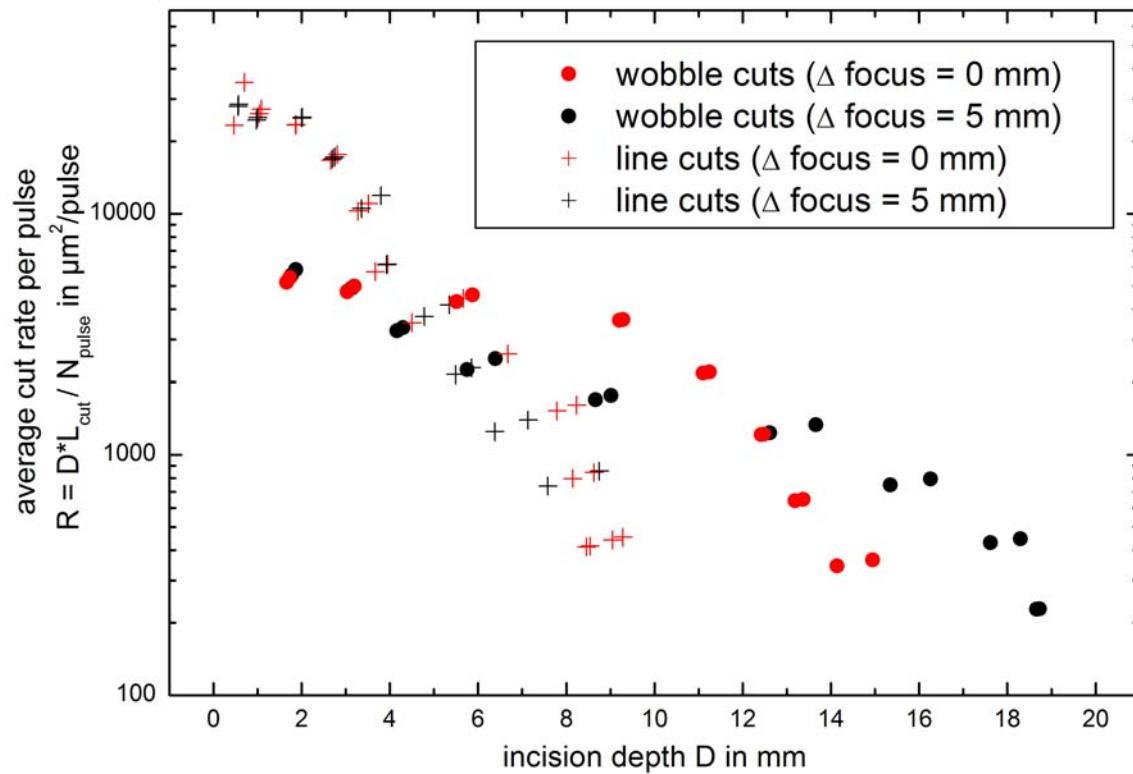
Figure 6.5: Average cut rate $R = D*L_{cut}/ N_{pulse}$ in μm^2/pulse for four sets of irradiation parameters; wobble cuts v_{linear} = 40mm/s, R_{wobble} = 0.4 mm and f_{wobble} = 135 Hz: (•) focus on the sample surface, (•) focus 5 mm deep in the bone tissue; irradiation with line cuts v_{linear} = 40mm/s (+) focus on the sample surface, (+) focus 5 mm deep in the bone tissue

The average cut rate *R,* plotted in figure 6.5, is the product of the cut length *L_{cut}* and the cut depth *D* divided by the number of applied pulses N_{pulse}. The ablation depth per pulse is not a useful measure to compare wobble with line cuts since in the wobble cuts the pulses are distributed in two dimensions. In figure 6.5, it can be seen that for a cut depth below ca. 5 mm, the cut rate is higher for simple linear cuts. The advantage of the wobble technique is, however, very pronounced (logarithmic scale in figure 6.5) at depths above 8 mm. Due to the widened incisions in the wobble technique more volume has to be ablated for the same incision depth. This slows down the cutting initially. However at incision depths above 8 mm this disadvantage is overcompensated by the improved energy transmission to the bottom of the incision in the widened cuts. Due to the broadening of the laser cut the loss mechanisms which are responsible for the limitation of the ablation depth are reduced and the maximal achievable cut depth is increased.

There are two dominant mechanisms for the limitation of the cut depth [Iva98, Iva00, Iva05]. One is the absorption of a part of the laser pulse energy by the ablation debris, which is already released at the beginning of the laser pulse. The debris is confined in the incision gap, and an especially high amount of energy gets lost in narrow deep cuts (see also [Afi04, Maj98]). In the second mechanism, the Gaussian beam creates a wedge shaped incision profile when the cut depth exceeds the cut width at the tissue surface. The ablation efficiency at the borders gets smaller. Though the deposited energy density (J/mm^3) is not influenced by the changed cut geometry, the thickness of the absorption layer perpendicular to the incision border decreases with increasing cut depth (see figure 6.6 cut profile geometry is approximated as an isosceles triangle). The thermal relaxation time is proportional to the square of the optical penetration depth, i.e. the layer thickness of energy deposition (see eq. 3.1). This means that the effective thermal relaxation time τ'_T decreases with increasing cut depth (see figure 6.6).
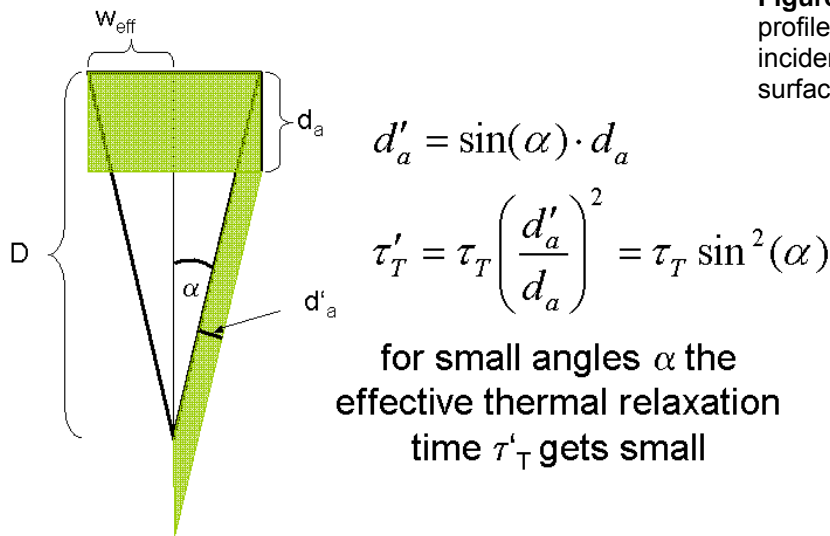
Figure 6.6: Approximated typical cut profile, with light absorption layer, laser incidence normal to original bone surface (after [Iva00])

$$d'_a = \sin(\alpha) \cdot d_a$$

$$\tau'_T = \tau_T \left(\frac{d'_a}{d_a}\right)^2 = \tau_T \sin^2(\alpha)$$

for small angles α the effective thermal relaxation time τ'_T gets small

Heat diffusion becomes faster and faster with rising incision depth since the layer of energy deposition gets thinner and thinner in the direction of the heat flow. In a descriptive consideration, this means that the temperature gradient gets steeper, so that the heat diffusion gets faster. The result of the faster heat diffusion is that, finally, the irradiance of the tissue by the laser pulse falls below the

irradiance threshold, and the ablation comes to a halt since at no time there is enough energy accumulated in the absorption volume to start the ablation process [Iva00].

The two different focus positions do not show significant changes in the ablation rate for the narrow linear cuts, whereas the 5 mm shift of the focus position into the bone sample increases the cut rate notably for the wobble cuts which are deeper than 12 mm. The reason why the repositioning of the focus 5 mm below the sample surface is much more advantageous for the wobble cuts compared to the narrow line cuts is probably that the repositioning distance was larger than optimal for the narrow line cuts. The beam diameter in the focus is about 160 µm (@$1/e^2$ level); 5 mm before the focus, the beam diameter is 580 µm (@$1/e^2$ level), the average effective cut width of the narrow line incisions with the focus on the sample surface is $w_{eff} = A / D \approx 160$ µm. So, the displacement of 5 mm, which is about 3.5 times the Rayleigh length, is obviously too large to improve the results. The cuts are basically to narrow for such a "large" displacement of the focus position and, so, no real advantageous effects can be measured. A smaller focus displacement for the narrow line cuts could give improved results. For the widened wobble cuts, the displacement of 5 mm improves the results significantly as already mentioned and explained above.

In figure 6.7 the specific ablation energy for the four series is plotted against the incision depth.

The behaviour of the specific ablation energy corresponds to the characteristics for the four irradiation modalities seen in the cut rate with increasing cut depth. At shallow incisions of up to 4 mm the specific ablation energy for all four ablation modalities was virtually identical. For increasing incision depths from 4 to 9 mm, the specific ablation energies for both narrow line cuts have a very steep rise, and the ablation does not proceed further than to incision depths of 9 mm. With the wobble technique, deeper incisions can be produced. For the focal position at the tissue surface, the steep increase in the specific ablation energy indicating the

saturation of the incision depth begins at approximately 13 mm cut depth, and a maximal incision depth of about 15 mm can be reached. In the wobble experiment with the focal position 5 mm inside the tissue, the steep increase starts at approximately 15 - 16 mm, and a cut depth of 19 mm can be reached with these parameters.
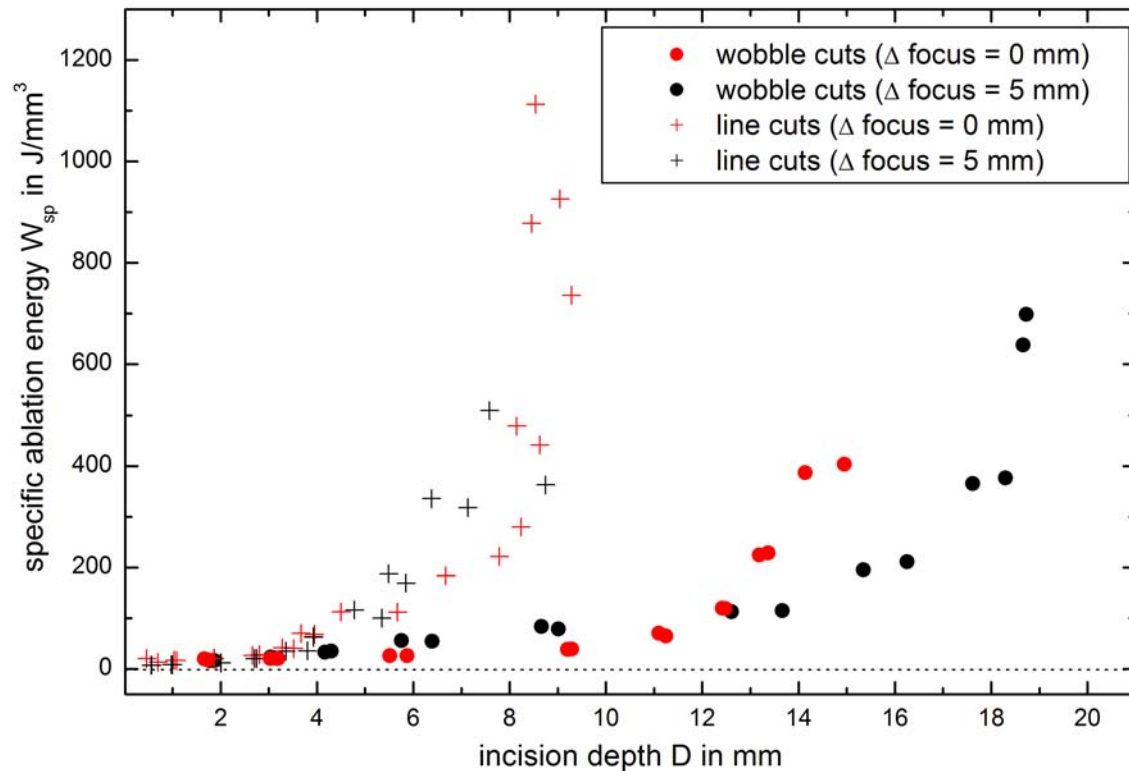
Figure 6.7: Specific ablation energy W_{sp} J/mm^3 against incision depth for four sets of irradiation parameters; (parameters as in figure 6.5)

With the wobble technique, one can reach incision depths which are high enough to dissect most human bones. This technique combined with a step-wise repositioning of the focal position during the irradiation was used during the animal trials described in appendix A.

6.3 Summary Chapter 6

In chapter 6 the ablation rate and specific ablation energy of four different laser systems for the ablation of bone tissue were compared. The slab CO_2 laser gave

the best all-round results, however the short pulsed TEA CO_2 laser was most effective for deep laser incision in bone tissue. In the second part of this chapter a technique for increasing the maximal achievable depth of a laser incision in bone was established and compared to simple linear cuts. By artificially broadening the cut width with the so-called "wobble" technique incisions, which were sufficient deep to be used for virtually any possibly medical intervention in bone, could be created.

7 Summary

7.1 Ablation Process

The purpose of this thesis is the detailed examination of the ablation process of hard tissue, mainly compact bone, with pulsed CO_2 lasers, and the verification of the thermo-mechanical process model for pulsed CO_2 lasers.

First, the composition and the physical properties of bone as the main representative of hard tissue were introduced, to explain the choice of a laser system used for laser ablation of hard biological tissue. Additionally, an overview of the present theoretical and experimental situation of laser processing of hard tissue was given. In this section, the advantages of pulsed CO_2 laser use for osteotomy were elaborated and the model of thermo-mechanical ablation, which is the basis for effective and gentle hard tissue processing, was introduced.

The data received from the various measurements (ablation depth, morphology, and chemical composition of the incision surface) described in chapter 5 support the thermo-mechanical character of bone tissue ablation with pulsed CO_2 lasers. The dependence of the ablation efficiency on the water content of the samples corresponds with the idea of hard tissue removal by "micro explosions" driven by high pressure build-up from extremely fast evaporation of tissue water.

Together with the increase of the relative occurrence of hydroxyapatite on the incision surface, the appearance of melting traces on the incision surfaces and borders in dehydrated bone samples, seen in the SEM analysis, indicates temperatures of at least 1100 to 1280°C during "dry" laser ablation. The less effective ablation process without water is probably driven by thermal decomposition

of collagen and vaporisation of the secondary products as well as thermo-mechanical forces by thermal expansion and melting of hydroxyapatite. That is why the cut surface is covered with a layer of re-solidified hydroxyapatite.

With the use of a water spray on fresh bones during the laser irradiation, the melting traces and relative increase of hydroxyapatite concentration on the incision surface are not observed.

The temperature reduction that occurs due to the application of a water spray is also seen in the conducted temperature measurements. Physiologically harmless temperatures during CO_2 laser ablation of bone tissue can be achieved by a combination of laser beam scanning and water spray application as verified by thermal measurements. These conclusions are supported by positive histological results and successful undelayed healing of sheep tibia dissected by the laser (see Appendix).

Based on the results from optical measurements, SEM, EDX, and thermal analysis, which were presented in this thesis, it can be concluded that the ablation process for hard tissue with pulsed CO_2 lasers combined with sufficient tissue water is clearly thermo-mechanical ablation as postulated.

7.2 Application of Laser Osteotomy

The bio-compatibility of the developed laser osteotomy procedure is shown in the results of the physical investigations presented in chapter 5, as well as by the histological and medical results introduced in appendix A. For the practical applicability, a suitable laser source had to be found and an optimised scanning technique had to be established. In chapter 6, it was realised that the slab CO_2 laser is a very convenient light source for the osteotomy. In combination with artificially induced cut dilation (wobble technique), most human bones can be dissected with the developed laser osteotome prototype consisting of a slab CO_2 laser and a fast

galvanic laser beam scanner. Some possible surgical applications are mentioned in the appendices B and C.

Based on the achievements presented in this thesis, a practical usability of a laser technique for osteotomy is shown for the first time. The successful animal experiments support these findings. An efficiently running prototype laser osteotome on the basis of a slab CO_2 laser was developed in our group and introduced in this thesis.

7.3 Outlook

The processing of hard biological tissue with lasers offers multiple advantages for several medical disciplines. Especially pulsed CO_2 lasers can be effective and biologically compliant tools to cut bone. To introduce laser osteotomy in medical practice, some advantageous medical applications have to be named first and appropriate set-ups and application-optimised irradiation techniques have to be established. In order to do so, it may be necessary to leave the well-established routines in operation planning. Moreover, the use of lasers in hard tissue surgery offers the possibility to define completely new operation techniques, e.g. self stabilising connections after bone dissection (figure 7.1), non-circular burs adopted to the jaw bone shape for (dental) implants, and precisely planned and computer-guided osteotomies for exactly fitting bone grafts or repositioning of bone parts.

For the practical medical adoption of the laser osteotomy, an online control system for the cut progression is indispensable. In this area, experiments with various acoustical and optical detector systems are currently being conducted in our group. For the application on human patients, it is necessary to establish a feedback procedure between local incision depth and the scanning procedure. One current project is the laser assisted implantation of a neuro-prosthetic cochlea implant as a hearing aid.
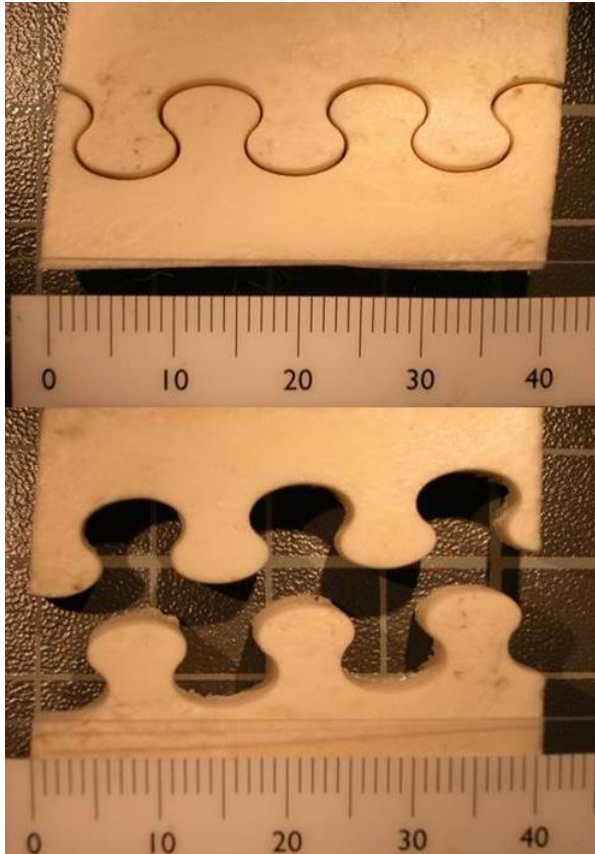
Figure 7.1: In vitro laser dissection of bovine compact bone sample executed in form of a self-stabilising connection

Appendix - Medical Applications

In this part of the appendix the possibilities of a medical application of the introduced laser ablation technique for hard tissue will be discussed. In the first part A, animal experiments, which were done with the prototype CO_2 laser osteotome developed in our group, are presented. The parts B and C consider the possibilities of a laser treatment for two well-defined medical indications. In contrast to the topics introduced until now, in these cases not bone but dentin and spinal ligament tissue were ablated with the CO_2 laser in ex-vivo laboratory experiments with human tissue samples.

A. Histological Examinations and Animal Experiments

In this sub-chapter animal experiments that have been done with the prototype laser osteotomy system "osteoLAS", which was developed in our group, are introduced. The laser osteotome system is based on the Rofin-Sinar SC x 30 slab CO_2 laser in combination with a fast laser beam scanner with galvanic drives (Raylase Turboscan C17). The beam is guided with a seven joint articulated mirror arm from the laser head to the beam scanner.

Four series of animal experiments have been carried out with this laser system so far. Two series, in which the tibiae of sheep were intersected with the CO_2 laser system, will be discussed in detail here. Several histological studies with laser irradiated ex-vivo bone samples have been conducted with different pulsed CO_2 laser systems in our group [Fre03, Iva02, Iva00] before the animal trials. The ex-vivo examinations revealed only minimal thermal damage to the surrounding tissue, if the multi-pass laser irradiation technique in combination with a fine water

spray was used. Two narrow damage zones were found along the incision border: first an amorphous intensively stained zone of 1-3 μm width and a second sharply confined however only weakly stained zone of 7-10 μm width. In a zone of ca. 50 μm width empty lacunae and damaged osteocytes were found. Intact osteocytes were however also found very near to the incision border [Fre03]. Promising histological results like this legitimated in-vivo investigations on the progress of healing after laser induced osteotomy in comparison to the conventional mechanical incisions.

There has been a comparative in-vivo study on the mandibles of seven dogs, which was conducted at the Klinikum rechts der Isar in Munich. The healing progress has been examined for 22 days after the intervention and the results of the laser incisions were compared with the results of incisions with a conventional bone saw. Dogs were chosen as an animal model because their jaw bone is arranged in a similar way like the human mandible. Narrow line cuts and widened wobble cuts were conducted with the laser. It could be verified that a complete healing through a whole bony rearrangement of the osteotomy gap with newly build lamellar bone was observed after 22 days in the case of optimal irradiation conditions [Iva05b]. The results of this series of animal trials are also reported with all details in the Dr.vet. thesis of C. von Hänisch [v.Hän03].

Another series of animal experiments was conducted at the University of Cologne in co-operation with Dr. Dr. R. Mischkowski from the Maxillofacial Hospital. In this series blocks of an approximate size of 20 x 10 mm were dissected with the prototype laser system from the mandible of four pigs. The healing process was controlled during three months and compared with the results of similar mechanical dissections. These trials are still not completely evaluated at the moment and will not be presented in this thesis.

In two most recent series of animal experiments the diaphysis of the sheep tibia was separated in the middle (at the position of the narrowest width) with the laser system. The operations were conducted at the animal hospital (Hospital for

Horses) of the University Zurich (Dr. B. v. Rechenberg) in co-operation with the department of maxillofacial surgery at the university hospital Basle (Prof. Dr. Dr. R. Sader, Dr. S. Stübinger, Prof. Dr. Dr. H.-F. Zeilhofer) as well as the department of maxillofacial surgery of the canton hospital Lucerne (Dr. Dr. J. Kuttenberger). The laser parameter, which were used during the animal trials are summarised in table A.1.

Two series of operations were conducted on 24 sheep in total. In the first series with 12 sheep the healing progress was histologically controlled for four weeks and in the second group for 12 weeks healing time. In each group six sheep tibiae were dissected with the laser system and six tibiae with a mechanical surgical saw. In each series three left and three right hind legs were cut with the laser and the saw respectively. For the experiments an oscillating saw (Synthes, Stratek) with blade thicknesses of 0.4 and 0.6 mm was used. The saw was guided manually. The aim of this study was the analysis of the bone healing under strong functional load. The two important topics were the clarification of possible influences of the laser osteotomy on fracture healing, bony regeneration and osteosynthesis on the one hand and the comparison of the bone healing after laser versus saw osteotomy on the other hand.

Table A.1: parameters of the prototype laser osteotome "osteoLAS" used during the in-vivo trials on the tibiae of sheep (* the last two tibias of the first group were irradiated with slightly different wobble parameters and focus positions, see table A.2)

Laser	Rofin-Sinar SC x 30 slab CO_2 laser
Beam Scanner	Raylase Turbo Scan C 17
Laser pulse duration	80 µs (FWHM)
Pulse repetition rate	200 Hz
Average Power	15 -17 W (depending on mirror arm adjustment)
Focussing optic	Plane field lens F = 300 mm
Focus radius	230 µm
Linear scan velocity	40 mm/s
Focus position relative to bone surface	Focus position initially 5 mm below the surface, position moved in 2 steps to 7 mm respectively 8 mm below the bone surface*
Wobble diameter	1.2 mm / 0.6 mm / 0 mm reduced corresponding with the repositioning of the focus position*
Wobble frequency	139 Hz*
Working distance	280 mm (at the initial stage, focus 5 mm beneath the bone surface))

For the animal experiments the laser osteotomy procedure was especially matched to the dissection of big "hollow" long bones like sheep tibia. Due to the structure of the cross section of a long bone (see Figure A.1 below) the manner the laser beam was moved across the bone is adapted to the bone structure. In the outer part of the bone essentially more compact bone has to be removed. Thus the laser beam is not simply moving perpendicular to the bone's long axis, but is moving along the two outer segments of the cut geometry twice as often as along the inner segment (outer segments red lines, inner segments black lines in Figure A.1). After several tests with different ratios of segment lengths, it was found out that for optimal adjustment to the bone geometry the three cut segments should have the same length. The difficulty in cutting long bones like the tibia, which can have diameters of up to 20 to 25 mm for sheep, is the layered structure of the bone. The outer layer of compact bone with a thickness of up to 5 mm can be cut quite easily with our technique. However the problem is that after the laser has cut the upper layer of compact bone and the bone marrow quite easily, the difficulty arises by cutting the compact bone layer at the backside of the long bone. In the layer of the bone marrow the laser beam propagates essentially as in free space so the beam is defocused on the posterior wall of the tibia. This problem can be tackled by widening the incision gap and lower the focus inside the tissue during the laser osteotomy. This technique will be described in the following. Also the access to the bone itself is limited and the laser cannot irradiate the tibia from all sides, which would make the operation much faster and more efficient but cause severe additional damage to the blood supply and disturb the healing process significantly. So the access to the bone is limited to about 90 to 120° of the circumference.

However it has to be stated that the task of dissecting a tibia bone has brought the laser osteotomy to its limits. The separating of long bones in straight cuts will never be a standard application for the use of lasers in osteotomies, since in this case the advantages of the laser osteotomy in comparison to the mechanical saw do not surface.

To achieve complete osteotomy of the tibia bone, two further techniques were additionally combined in the procedure. First the cut was artificially widened by adding a transversal wobble movement of the laser beam. With that more laser energy could reach the lower section especially in deep cuts (see chapter 6.2). The resulting movement of the laser beam was a superposition of a small circular movement (diameter maximal 1.2 mm) and the linear movement across the tibia, so a spiral movement was the result. The frequency of the circular movement was empirically chosen to be 139 Hz after extensive ex-vivo testing. As a second measure to increase the ablation efficiency the laser focus was positioned about 5 mm under the bone surface initially and was moved stepwise further under the bone surface. These two techniques were combined so that with each movement of the laser focus position deeper under the bone surface the diameter of the wobble movement was also reduced.

This was done in three steps:

1.stage: focus 5 mm beneath surface, $\emptyset_{wobble}$=1.2 mm, f_{wobble}=139 Hz

2.stage: first adjustment: focus 7 mm below surface, $\emptyset_{wobble}$=0.6 mm, f_{wobble}=139 Hz

3.stage: second adjustment: focus 8 mm below surface, no wobble movement.

For especially thick bones a fourth step, with a larger wobble diameter to start with, can be used. This was done in the last two cases of the first series. The time for each step was individually adjusted depending on the progress of the laser cut in the bone. In general approximately 2/3 of the bone was cut at the first stage and 1/6 each after the first and second adjustment.
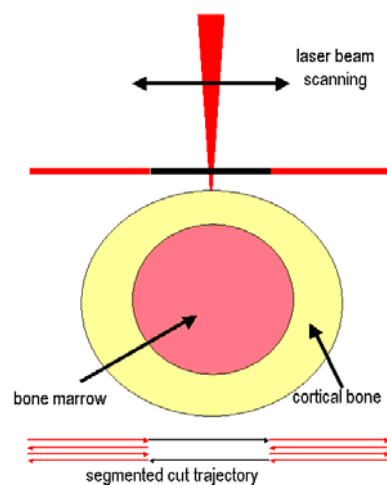

Figure A.1: schematic cross section of the diaphysis of a long bone and segmented laser cut[0]

These optimal settings for the long bones were combined with our standard laser parameters: 200 Hz pulse repetition rate, 80 µs pulse duration, which corresponds to an average power of 15 to 17 W. Different focusing optics (F = 150 – 300 mm) were tried and it was found, that the longest available focal length provides best results for the long bones, because of a high Rayleigh length, which is beneficial for deep cuts and makes the handling easier due to an increased working distance. The used plane field optic of 300 mm focal length gave a laser spot diameter of about 460 µm (@1/e^2-level) and a Rayleigh length of 12 mm in the used set up.

Two water sprays were aimed into the cut groove from each side of the bone. A relatively high flow (12.5 ml/min/spray) of sterile isotonic sodium chloride water solution was used with the sprays. To prevent the damaging of the underlying soft tissue two metallic surgical spatulas were positioned under the rear side of the tibia bone. In the following tables A.2 and A.3 all operations of the two series are listed. After the dissection of the tibia the two bone parts were connected with an osteosythesis slint (3.5 mm thick dynamic compression plate), which was screwed directly on the periosteum and bone. The two cut surfaces were placed in direct contact to each other under moderate pressure to ensure optimal healing conditions. The leg was additionally stabilised with an external cast.

The average tibia thickness in the second series was smaller than in the first series. The thickness during the second series was essentially the same as in the ex-vivo experiments previously done in the laboratory with tissue samples. So the established parameters for wobble adjustment and focus repositioning worked well in the second series. The healing progress after the osteotomies was carefully monitored in the hospital. Immediately after the operation two X-ray radiographs (medial-lateral and anterior-posterior view) were taken of each osteomised leg. For the second group (12 weeks healing time) every 4 weeks two additional radiographs were taken from each dissected leg. Of all sheep one set of radiographs was recorded post-mortem at the end of the healing time. So the healing progress was well documented radio-graphically. Additionally a fluorescence dye was administered to the sheep during the healing phase. This dye is deposited mainly in new fast reproducing tissue just like the newly grown and remodelled bone tissue in

the area of the incision. The healing progress could be visualised with fluorescence microscopy of fine sections of the area of the osteotomy, taken from the grafted bone samples after the sheep were sacrificed. Also conventional histological examinations techniques (Toluidin-blue-staining and Fuchsin-vital-staining) were used to analyse the healing progress of the osteotomies at the end of the healing phase.

A.1 Results and Conclusions

The osteotomy of long bones like sheep tibia is possible with pulsed CO_2 laser multi pass scanning and application of a water spray with only minor thermal damage to the bone tissue (even at tibia diameters over 20 mm). For a complete osteotomy an artificial widening of the laser cut with the wobble technique and stepwise repositioning of the focus position is necessary. The technique results in wedge-shaped osteotomy gaps (entrance incision width corresponds to the maximal wobble amplitude of 1.2 mm). Clinically uneventful healing was observed after the laser osteotomy, similarly to saw osteotomy in the control groups. None of the animals had to be excluded from the study due to osteotomy-related complications. The histological control indicates undisturbed bone vitality and normal remodelling within the compact bone during the healing, undisturbed endosteal and periostal callus formation as well as less micro-fracturing compared to the saw osteotomy. The medical and histological results concerning the laser osteotomy of the tibia of sheep were reported in detail by Dr. Dr. J. Kuttenberger [Kut05, Kut05b].

First series of animal trials: sheep tibia, healing time 4 weeks

Table A.2: Overview over the first series of in-vivo laser osteotomy of tibia of sheep

sheep	irradiation time	wobble diameter / frequency	focus position relative to bone surface	length of cut geometry	remarks
1.1 left hind leg	a) 9' 20" b) 6' 00" c) 4' 00" _____ 19' 20"	all 139 Hz a) 1.2mm b) 0.6 mm c) no wobble	a) 5 mm b) 7 mm c) 8 mm	22 mm	The bone is almost completely laser dissected. The remaining very fine connecting ridge is broken manually under very low pressure.
1.2 left hind leg	a) 9' 00" b) 6' 00" c) 4' 00" _____ 19' 00"	all 139 Hz a) 1.2mm b) 0.6 mm c) no wobble	a) 5 mm b) 7 mm c) 8 mm	24 mm	The bone is almost completely laser dissected. The remaining ridge is broken manually under slightly increased pressure. The bone does not break exactly along the prolongation of the laser incision, so that a kind of breaking spike appears.
1.3 right hind leg	a) 9' 00" b) 7' 30" c) 4' 00" _____ 20' 30"	all 139 Hz a) 1.2mm b) 0.6 mm c) no wobble	a) 5 mm b) 7 mm c) 8 mm	25 mm	The complete bone thickness is about 22 mm. About 2 mm of bone thickness remains after the laser irradiation. This bony bridge is cut manually with a band-saw after the laser irradiation.
1.4 right hind leg	a) 10' 00" b) 10' 50" c) 7' 30" _____ 28' 20"	all 139 Hz a) 1.2mm b) 0.6 mm c) no wobble	a) 5 mm b) 7 mm c) 8 mm	25 mm	The thickness of the bone is approximately 22 mm. The bone is dissected to only about 50 – 60 % after the laser irradiation. The rest is cut mechanically.
1.5 right hind leg	a) 10' 00" b) 8' 30" c1) 2' 06" c2) 3' 08" d) 2' 00" _____ 25' 44"	all 139 Hz a) 1.5 mm b) 1.0 mm c) 0.5 mm d)no wobble	a) 5 mm b) 7 mm c) 9 mm d) 9 mm	25 mm	Because the last two tibiae have not completely been dissected by the laser irradiation the initial wobble width is increased and an additional adjustment step for the focus position and wobble amplitude is introduced. (It has to be said that the thickness of the tibia in the in-vivo experiments is considerably larger than for the tibia used in the ex-vivo laboratory experiments. So the parameters established in the ex-vivo experiments have to be adapted to the new situation.) After the irradiation the bone is virtually completely dissected and could be broken with only very small manually applied pressure. tibia measures: complete thickness: 22 mm thickness of compact bone layer: medial 5 mm lateral 4,5 mm anterior and posterior 4 mm After the irradiation phase c1) the position of the laser movement was corrected by 0.7 mm transversely to the laser movement to match the incision groove, since the leg or the beam scanner had moved; the focus position was not changed any further after that.
1.6 left hind leg	a1) 5' 00" a2) 5' 00" b1) 4' 00" b2) 4' 30" c1) 4' 30" c2) 1' 30" d) 5' 50" _____ 30' 40"	a1) 1,5 mm / 143 Hz a2) 1,5 mm / 139 Hz b1) 1,0 mm / 139 Hz b2) 1,0 mm / 143 Hz c) 0,5 mm / 139 Hz d)no wobble	a) 5 mm b) 7 mm c1) 9 mm c2)10 mm d) 11 mm	25 mm	After phase b1) the position of the laser movement was newly aligned (by 0.2 mm transversely). Since the transverse movement was very small in relation to the initial wobble width of 1.5 mm, the focus was further moved into the bone. tibia measures: complete thickness: 22 mm complete width: 18 mm thickness of compact bone layer: medial 5 mm lateral 6 mm anterior and posterior 4 mm

Second series of animal trials: sheep tibia, healing time 12 weeks

Table A.3: Overview over the second series of in-vivo laser osteotomy of tibia of sheep

sheep	irradiation time	wobble diameter / frequency	focus position relative to bone surface	length of cut geometry	remarks
2.1 left hind leg	a) 9' 00" b) 7' 00" c) 3' 10" _____ **19' 10''**	All 139 Hz a) 1,2mm b) 0,6 mm c) no wobble	a) 5 mm b) 7 mm c) 8 mm	19 mm	The bone is virtually completely laser dissected. The last connecting ridge is broken manually under minimal pressure. Tibia measures: complete thickness: 20 mm complete width: 14 mm thickness of compact bone layer: medial and lateral 5 mm anterior and posterior 4.5 mm
2.2 left hind leg	a) 7' 40" b) 5' 00" c) 4' 13" _____ **16' 43' '**	All 139 Hz a) 1,2mm b) 0,6 mm c) no wobble	a) 5 mm b) 7 mm c) 8 mm	19 mm	complications during initial phase of narcosis The bone is virtually completely laser dissected. The last connecting ridge is broken manually under minimal pressure. Tibia measures: complete thickness: 17 mm complete width: 14 mm thickness of compact bone layer: medial and lateral 4 mm anterior and posterior 3.5 mm
2.3 right hind leg	a) 9' 00" b) 4' 30" c) ---' _____ **13' 30' '**	All 139 Hz a) 1,2mm b) 0,6 mm c) no wobble	a) 5 mm b) 7 mm c) 8 mm	18 mm	The bone is completely laser dissected already during phase Tibia measures: complete thickness: 17 mm complete width: 15 mm thickness of compact bone layer: medial and lateral 6 mm anterior and posterior 5 mm
2.4 right hind leg	a) 7' 00" b) 3' 20" c) 3' 50" _____ **14' 10''**	All 139 Hz a) 1,2mm b) 0,6 mm c) no wobble	a) 5 mm b) 7 mm c) 8 mm	18 mm	The bone is virtually completely laser dissected. The last connecting ridge is broken manually under minimal pressure. Tibia measures: complete thickness: 18 mm complete width: 15 mm thickness of compact bone layer medial 7 mm, lateral 5 mm anterior and posterior 4 mm
2.5 right hind leg	a) 9' 00" b) 9' 00" c) 1' 10" _____ **19' 10''**	All 139 Hz a) 1,2mm b) 0,6 mm c) no wobble	a) 5 mm b) 7 mm c) 8 mm	18 mm	The bone is virtually completely laser dissected. The last connecting ridge is broken manually under minimal pressure. Tibia measures: complete thickness: 17 mm complete width: 14.5 mm thickness of compact bone layer: medial 5 mm, lateral 4 mm anterior 5mm, posterior 5 mm
2.6 left hind leg	a) 10' 00" b) 6' 00" c) 5' 12" _____ **21' 12''**	All 139 Hz a) 1,2mm b) 0,6 mm c) no wobble	a) 5 mm b) 7 mm c) 8 mm	18 mm	The bone is virtually completely laser dissected. The last connecting ridge is broken manually under minimal pressure. Tibia measures: complete thickness: 18 mm complete width: 15 mm thickness of compact bone layer: medial 7 mm, lateral 5 mm anterior 6.5 mm, posterior 5 mm

B. Laser Ablation of Dentin

In this paragraph a study concerning the laser ablation of human dentin is described. It was done in co-operation with Dr. S. Stübinger from the maxillofacial department of the University Hospital Basle [Stü05].

Dentin is a dental hard tissue which takes up most of the tooth volume and lies between the very hard dental enamel and the soft pulp in which the tooth nerve is situated. The composition of dentin is essentially identical with that of compact bone. The principal structure of a human tooth is shown in figure B.1.
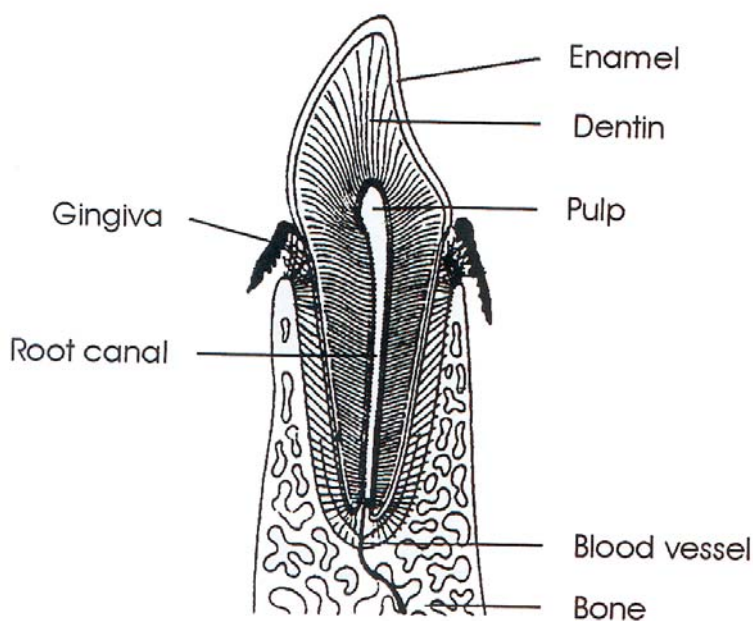

Figure B.1: Structure of a human tooth (taken from [Nie96])

The aim of this study was to evaluate the possibility of a practical use of a pulsed CO_2 laser for the treatment of a tooth avulsion (loss of complete tooth). After the avulsion - e.g. as result of a trauma - it is possible to replant the complete tooth if the root and the periodontal ligament which covers the root and provides the attachment to the alveolar bone of the mandible are still intact. The apex of the root of the avulsed tooth is usually dissected at about 3 mm from the end with a mechanical saw. With mechanical burs a hole is drilled in the tooth from the reverse

direction along the root and a titanium post is adapted. With the bur mainly dentin is removed from the bone as well as the complete dental pulp. The titanium post is then fixed in the hollowed root. The diameter of the bore hole has to be adapted to the tooth size; the whole dental pulp has to be removed and enough tooth material has to remain around the bore to prevent the tooth from breaking. The whole tooth with the titan post can be replanted if the periodontal ligament is still viable. In this case the tooth could regain its natural fixation to the alveolar bone and no artificial implant would be needed.

One disadvantage of this procedure is that only circular bores are possible with mechanical tools. The frontal teeth, which are affected most often from trauma-induced avulsion, are however not round shaped, so that the possibility of an elliptical or even more complicated bore shape would be advantageous. The use of a pulsed CO_2 to drill in the tooth root would offer arbitrary bore geometries specially adapted to the individual tooth geometry.

The apex of the root (about 3 mm) of 15 human teeth was removed with a diamond saw. After wards the prepared teeth were fixed with the crown in a special holder. The bores in the dentin of the root were made with a Rofin Sinar SC x 30 slab CO_2 laser in combination with a galvanic beam scanner (Arges Elefant 20). With the use of a scanner, bores with arbitrary geometries and suitable sizes could be realised in the tooth roots. Temperature changes during the laser irradiation were monitored with thermocouples (K-type) positioned on the root surface, at the position of the periodontal ligaments, which must not be damaged for successful replantation of the teeth. The teeth were irradiated with a pulse duration of τ_{FWHM} = 80 µs and a pulse energy of E_{pulse} = 72 mJ, resulting in an average power of 3.6 W at a repetition rate of f = 50 Hz. With a focus radius of $w_f \approx$ 80 µm (@1/e^2 level) a radiant exposure of 360 J/cm^2/pulse was achieved. To create the bores a special irradiation pattern was applied. The desired bore outline geometry adapted to the tooth shape was filled by a grid of lines with a spacing of 150 µm as shown in figure B.2 (screenshot from the scanner software INSCRIPT) for a circular bore. The filling grid consisted out of three sets of parallel lines scanning lines with a rotation of 60°

relatively to each other. To counteract the conical shape of the bore the outline of the geometry was more often scanned than the filling grid. The best results could be achieved with the following irradiation sequence. First the outline was scanned 100 times and after that the outline and the filling grid was scanned 10 times in turn. The grid lines are scanned bi-directional. Afterwards the whole cycle was repeated again. The scanning speed was v = 50 mm/s. The resulting geometrical pulse overlap was only n = $w_f \cdot f/v$ = 0.07.
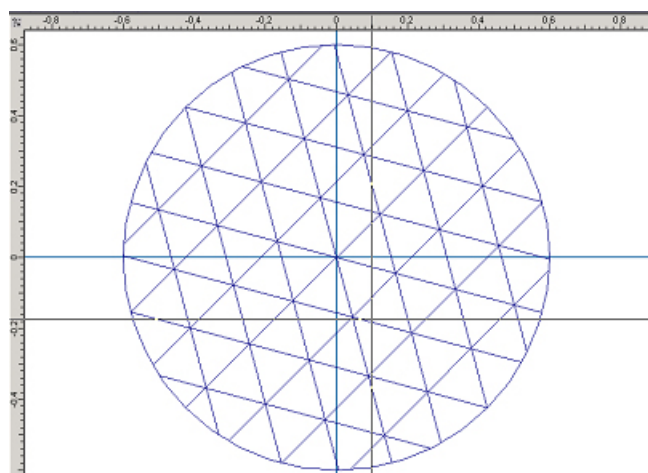

Figure B.2: Scanning geometry, bore outline was filled with a grid of three sets of scanning lines with a rotation of 60° relatively to each other; the spacing of the lines was 150 µm

The samples were irradiated with the pattern described above for 6 to 8 minutes. A water spray was applied during the irradiation which was directed into the bore. No temperature rise higher than 2 K was recorded at the tooth root surface. So a thermal damage to the periodontal ligament can be excluded in this procedure. Visually clean bores with no signs of carbonisation were achieved.
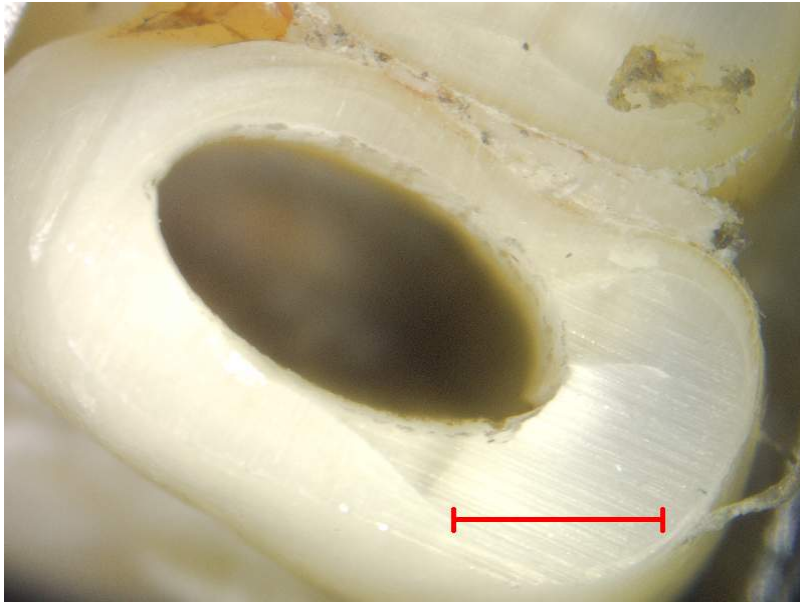
Figure B.3: Elliptical bore in human tooth,
scale length 2 mm
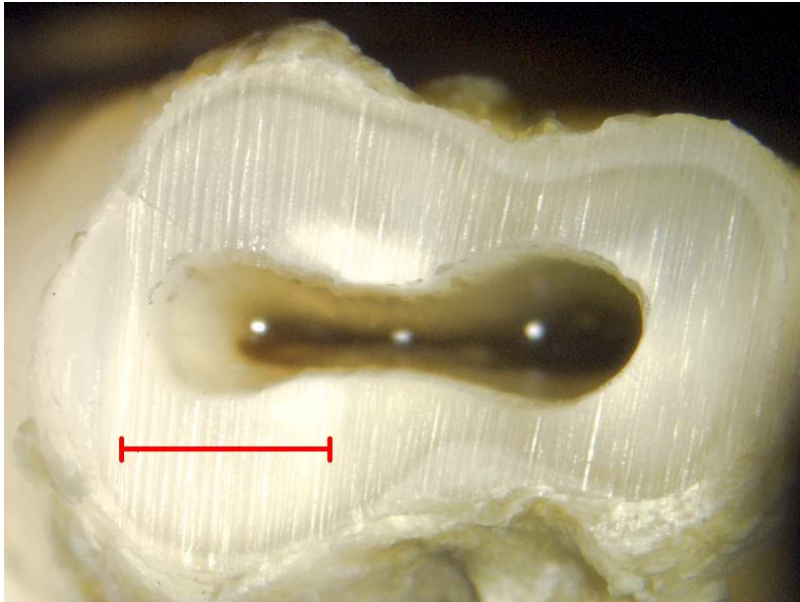
Figure B.4: root shape adapted bore in human tooth, scale length 2 mm

In figures B.3 and B.4 two bores in teeth are shown. After the irradiations the bores were filled carefully with water with an Eppendorf pipette. This was done under optical control and the filling of the bore was stopped when the upper brink was reached. In that way the volume of the bores was estimated and the specific ablation energy was calculated as the average applied laser power multiplied with the irradiation time and divided by the ablated volume. The values for the ablated volume presented here are average values from two separate measurements. The specific ablation energy could be calculated for eleven of the fifteen experiments. The estimated volume V_{abl}, the applied energies E_{total} and the calculated specific

ablation energy W_{sp} are summarised in table B.1. The values for irradiation 3 and 9 are outliers and are not used for calculating the average value.

Table B.1: overview over laser bores in teeth

Sample number	V_{abl} [mm³]	$T_{irradiation}$ [s]	<P> [W]	E_{total} [J]	W_{sp} [J/mm³]
2	48	420	3.8	1596	33.23
3	8.5	360	3.8	1368	160.94
5	n.a.	496	3.6	1786	n.a.
6	63.5	360	3.6	1296	20.41
7	50	520	3.6	1872	37.44
8	42.5	496	3.6	1786	42.01
9	12.5	402	3.6	1447	115.78
10	27.5	380	3.6	1368	49.75
11	30	360	3.6	1296	43.20
16	51.5	424	3.45	1463	28.40
17	22.5	360	3.45	1242	55.20
19	67.5	360	3.45	1242	18.40
(average value ± standard deviation)					36.43 ± 12.57

The average value for the specific ablation energy for the laser ablation of dentin is 36.4 J/mm³. It has to be taken into account that the ablated bone tissue was not completely occupied by dentin alone. The ablated volume of the teeth contained also the dental pulp. In some samples the tooth was already severely damaged by caries. These teeth have been treated by a dentist previously, the pulp had been taken out and the cavity was filled with cement or gradually with calcified tissue. Therefore the measured value for the specific ablation energy is probably higher than the value for a healthy avulsed tooth, which contains a viable soft tissue pulp, would be.

The bore walls of two of the samples were inspected afterwards with the scanning electron microscope (LEO Supra 55, see chapter 5.1). The SEM technique allows examining the microscopic structure of the surface and evaluating possible damages. The images of the first SEM sample (No. 5 in table B.1) are shown in figures B.5 and B.6. The images from the second SEM sample (No. 2 in table B.1) are shown in figure B.7 to B.10. Figure B.11 shows the surface of a saw cut in

dentin of the second sample at the apex of the root which was dissected. Table B.2 gives an overview over the SEM images of the two samples.

Table B.2: overview over SEM images of laser irradiated teeth

SEM image	Sample	Sample preparation	Short description
Figure B.5	5	No coating	Area of laser bore wall without melting traces
Figure B.6	5	No coating	Area of laser bore wall without melting traces
Figure B.7	2	40 nm gold coating	Area of laser bore wall with isolated melting traces
Figure B.8	2	40 nm gold coating	Area of laser bore wall with isolated melting traces
Figure B.9	2	40 nm gold coating	Area of laser bore wall with isolated melting traces, dentin canals visible (perpendicular to image plane)
Figure B.10	2	40 nm gold coating	Area of laser bore wall with isolated melting traces, truncated dentin canals visible (parallel to image plane)
Figure B.11	2	40 nm gold coating	Surface of saw cut in dentin

Figures B.5 and B.6 show the surface of the wall of the laser induced bores in tooth sample number 5. In these images areas are depicted that show no traces of molten material. A "rough" uneven fibrous structure is visible. In figure B.7 and B.8 comparable sections of the laser bore wall of sample 2 are shown. In these areas small isolated traces of molten material are visible (white arrows). The surface structure of the sample is still rough and uneven. Figure B.9 depicts an area of the laser bore wall of sample 2, where the entrances of dentin canals are visible (black arrows). These canals lead from the pulp into the dentin. The canals visible in image B.9 are open.
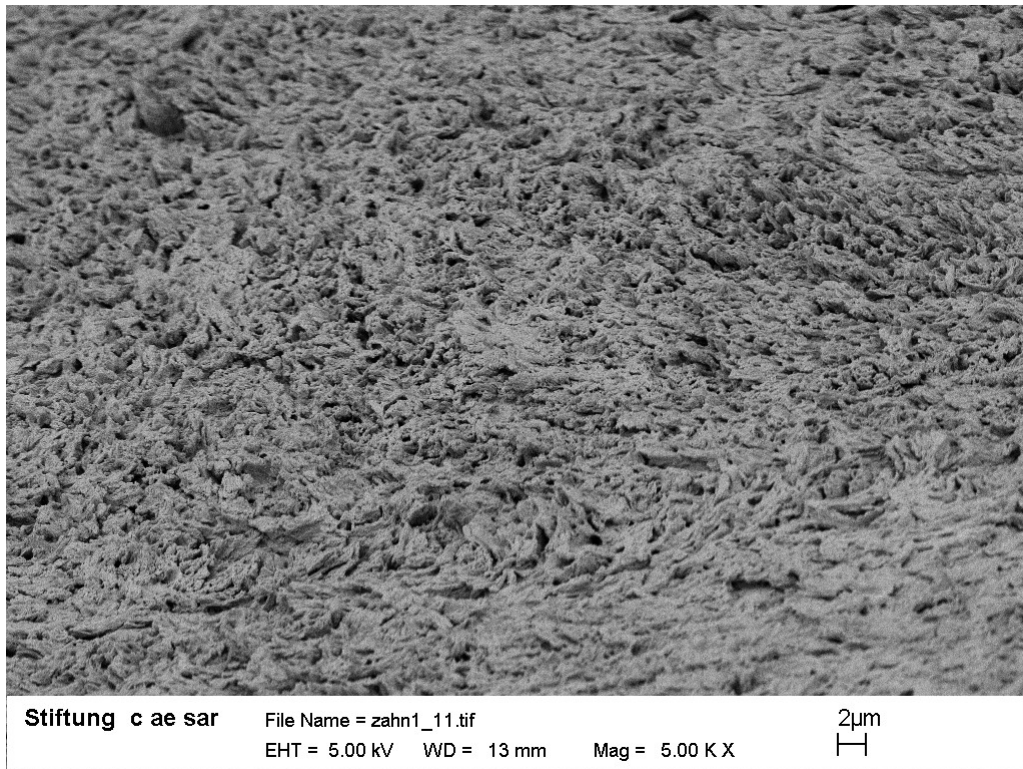
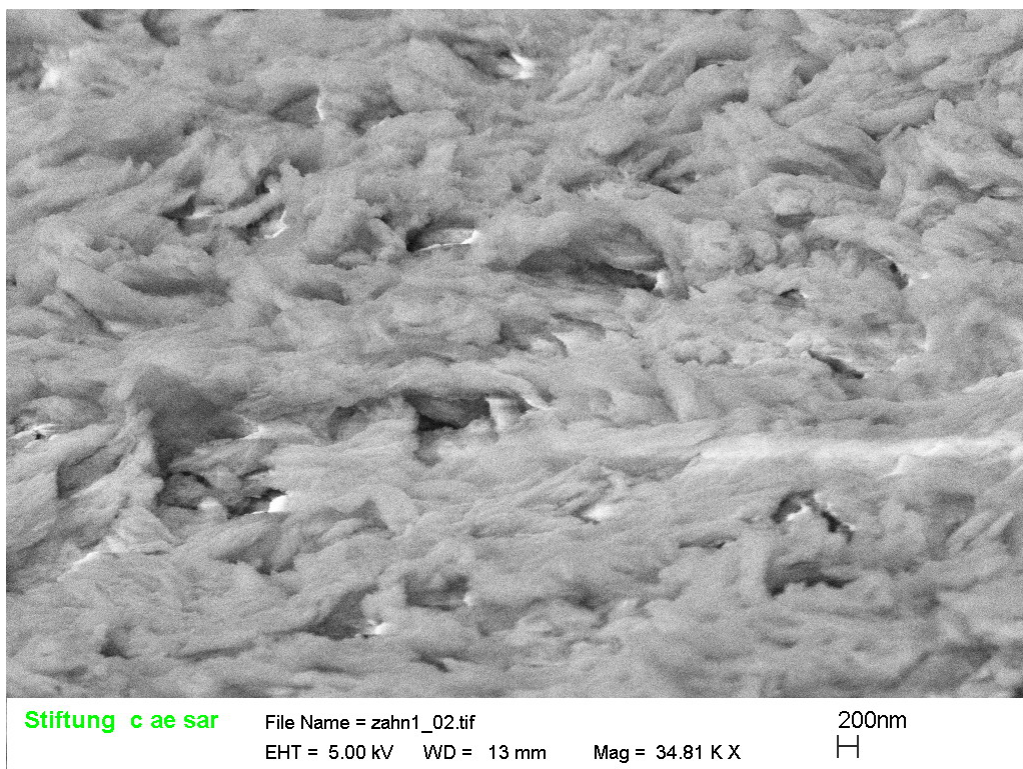**Figure B.5:** SEM image laser bore wall in tooth root (sample 5)

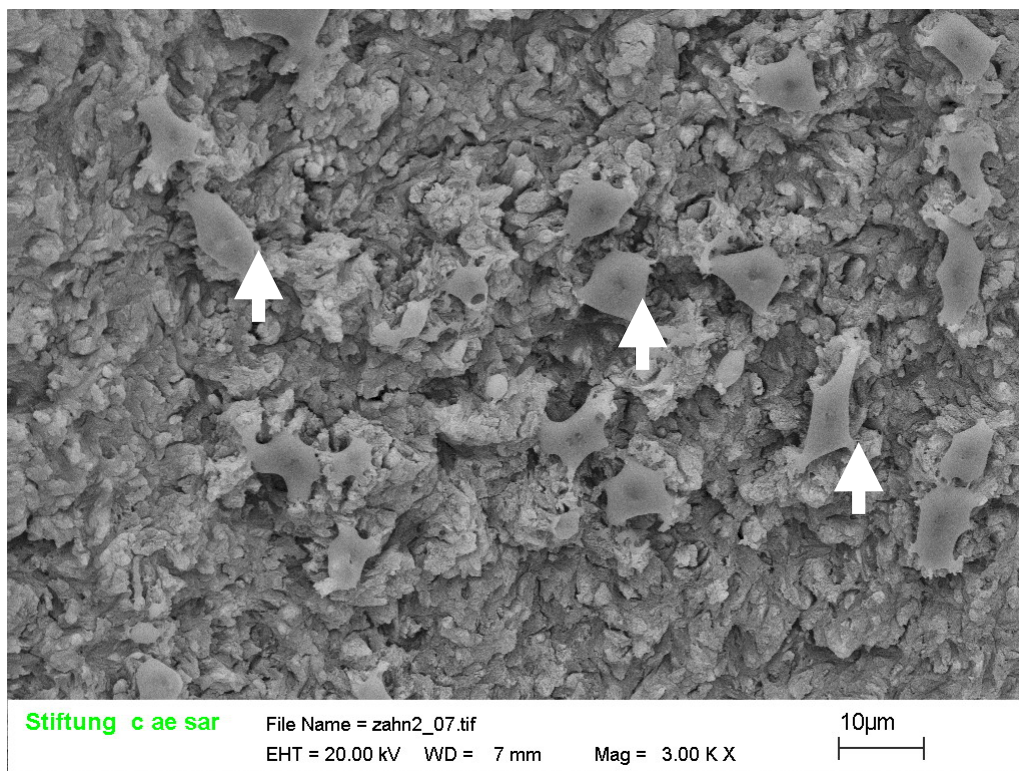**Figure B.6:** SEM image laser bore wall in tooth root (sample 5)

Figure B.7: SEM image laser bore wall in tooth root (sample 2)
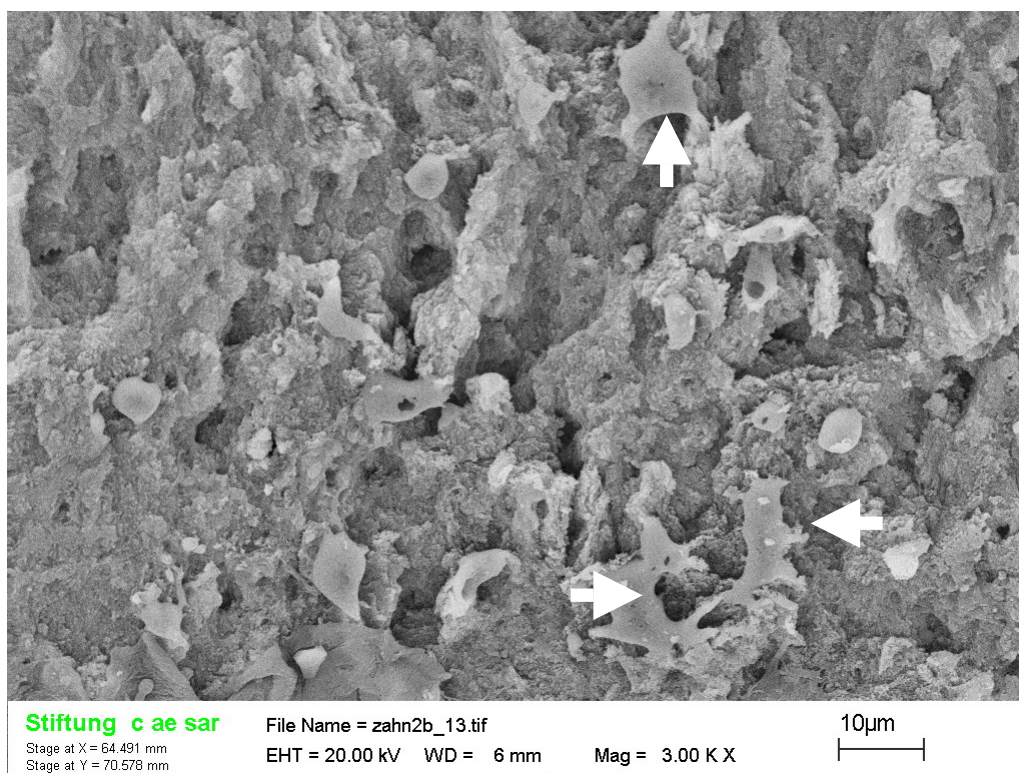
Figure B.8: SEM image laser bore wall in tooth root (sample 2)
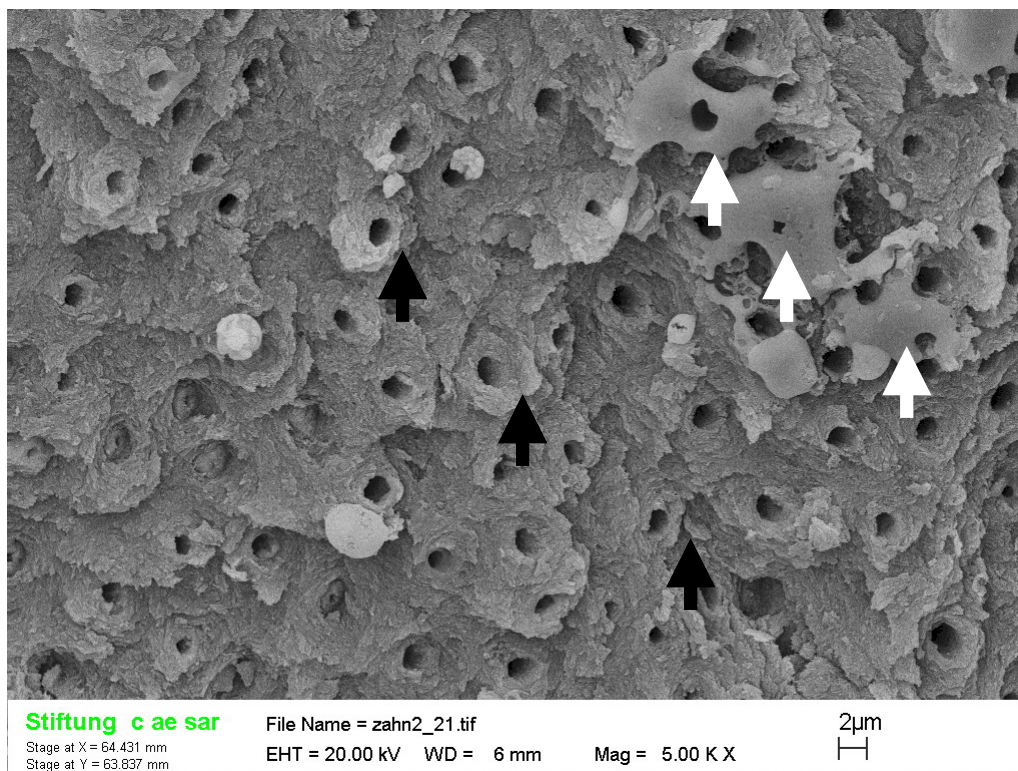
Figure B.9: SEM image laser bore wall in tooth root (sample 2)

In the figure B.10 the dentin canals run parallel to the image plane and are truncated. The direction of the dentin canals is indicated by the black double arrow. Here are also some melting traces visible (labelled by white arrows). Figure B.11 displays the surface of a saw cut, with which the apex of the root was removed. Here the uneven structure of the dentin surface as seen in the previous images is not visible. The surface seems to be coated with a smear layer. Multiple cracks are visible which cover the whole surface relatively homogeneous. The extensive cracking is not visible at the surface of the laser bore walls.

Figure B.10: SEM image laser bore wall in tooth root

Figure B.11: SEM image saw cut in dentin

It has to be stated that at the wall of the laser bores isolated traces of molten dentin can be found. This indicates high temperatures in the ablation zone. This may be the result from the limited irradi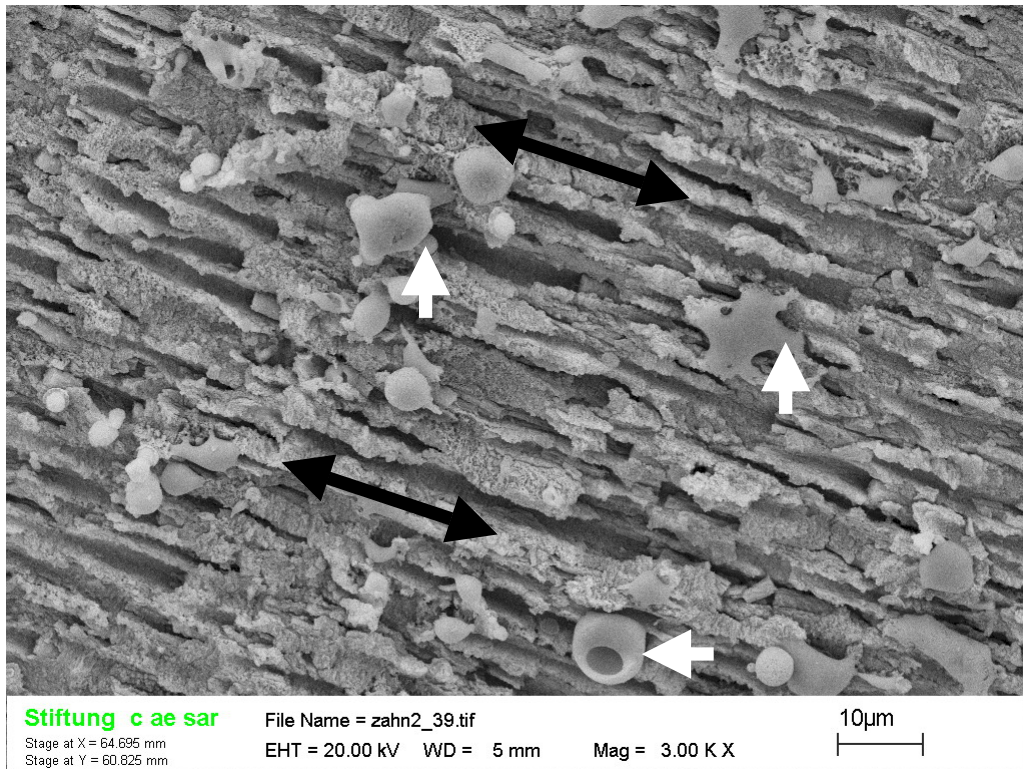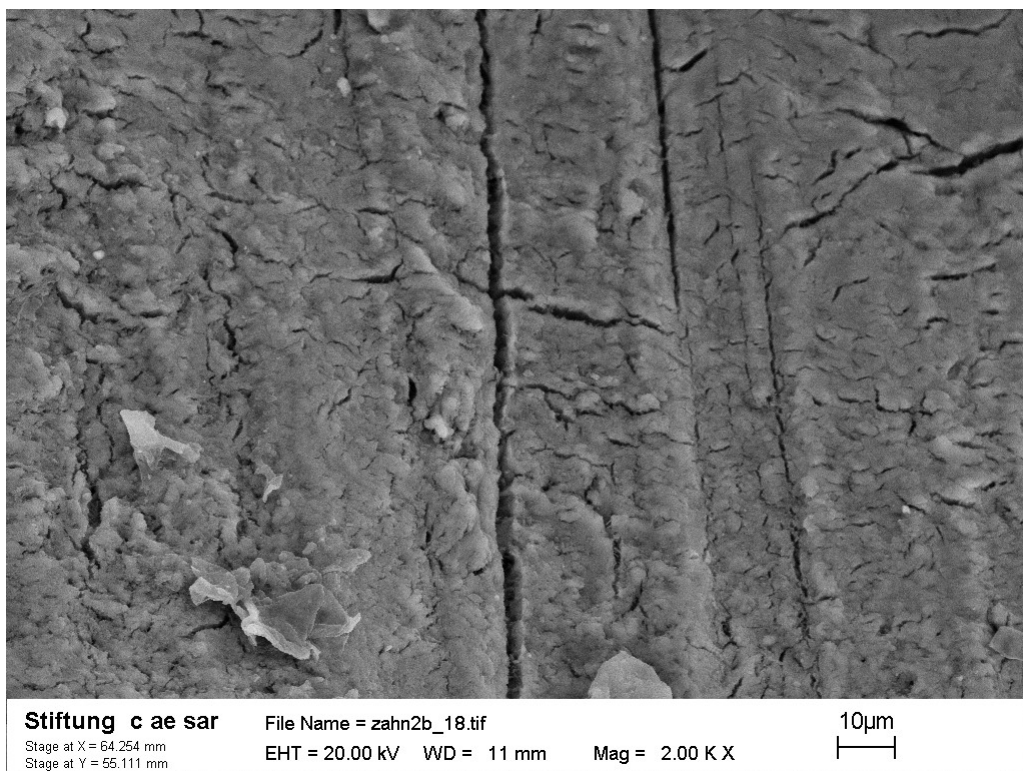ation area i.e. the short scanning lines which were used for creating the bores. Each point of the scanning pattern is passed in short intervals by the laser beam which leads to higher temperature accumulation. Additionally it is also possible that ablation debris, which was heated up and molten by the later part of the laser pulse after being ablated and ejected, has fallen back into the bore and was deposited on the bore walls and re-solidified there.

However it is questionable if a small thermal damage on the inside of the bore wall would influence the outcome of a treatment with a laser bore negatively, since the viable tissue of the pulp in the centre of the tooth is removed completely anyway and a titanium post is cemented into the bore. The periodontal ligament which is important for the natural attachment to the alveolar bone will not be damaged since the temperature rise recorded at this area is negligible. Final clarification could be achieved in histological examinations of viable teeth in ex-vivo experiments. In the scope of this study only teeth pulled out for regular therapeutic reasons at an unknown time interval before the irradiation experiments were used and not freshly extracted teeth from which histological conclusions could be drawn. The study demonstrates the possibility of the use of a new laser technique in the treatment of avulsed teeth. The option of matching the bore geometry to the specific tooth root shape which has to be replanted in the laser treatment would be especially useful for frontal teeth, which are most often affected by avulsion and are not nearly circular.

C. Laser Ablation of Flavum Ligament

In this section the ablation of a soft tissue is discussed. The yellow ligament (flavum ligament) is the inner lining tissue of the spinal canal in which the spinal cord is covered.
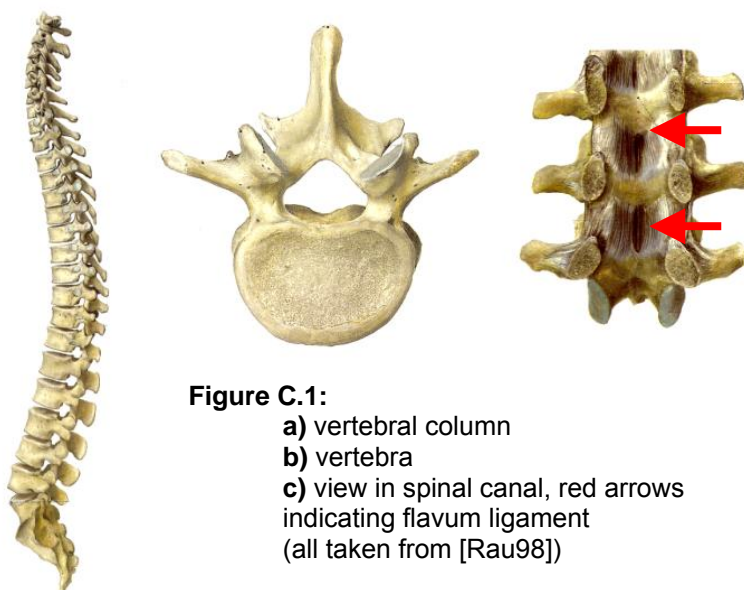
Figure C.1:
a) vertebral column
b) vertebra
c) view in spinal canal, red arrows
indicating flavum ligament
(all taken from [Rau98])

A quite common disease of old age is lumbar spinal stenosis, where a hyperthrophy of the lining tissue in the spinal canal causes pressure on the spinal cord. Usually this disease is treated with a massive surgical intervention. During this intervention the vertebral arch of one or more vertebra is removed partly (lumbar laminectomy) to achieve decompression of the spinal cord. The operation results in extended trauma to the spinal muscles, bones and ligaments, which can lead to destabilisation of the spinal vertebral column [Dat04]. It would be very advantageous to find a minimal invasive technique for the treatment of this disease. A laser treatment could be well suited to ablate the tissue (flavum ligament) inside the spinal canal without removing much of the bony tissue of the vertebral arch. In the study presented in this sub-chapter the laser ablation of flavum ligament with a pulsed CO_2 slab laser (Rofin - Sinar SC x 30) was examined. The study described in this sub-chapter was done in co-operation with Dr. F. Rommel of the neuro-surgical department of the University Hospital Düsseldorf.

Samples of human flavum ligament attached to the laminae of spinal segments from the lumbar spine were used for this study. The samples were stored at -20°C and were allowed to reach room temperature again before laser irradiation and were irradiated within one hour. Almost 30 irradiations were conducted. Finally 13 irradiated samples could be used for analysis. The irradiations were done with the Rofin-Sinar SC x 30 slab CO_2 laser in combination with the Arges Elefant 20

laser beam scanner. With a flat field focussing lens (focal length 163 mm) of the laser beam scanner a focal radius of about 100 μm (@$1/e^2$ level) was achieved. The sample surface was aligned perpendicular to the beam axis as good as possible. A special multi-pass scanning pattern was designed to achieve optimal volumetric ablation. A set of 50 perpendicular lines of 5 mm length with a spacing of 0.1 mm was scanned with a scanning speed of 5 mm/s. The pulse repetition rate was 50 Hz; so 2500 pulses were applied during one set of lines. Some irradiations were done with two sets of lines which were orientated perpendicularly to each other. Two different pulse durations were used 44 μs with a pulse energy of 36 mJ and 56 μs with a pulse energy of 62 mJ. The scanning pattern is shown schematically in figure C.2.
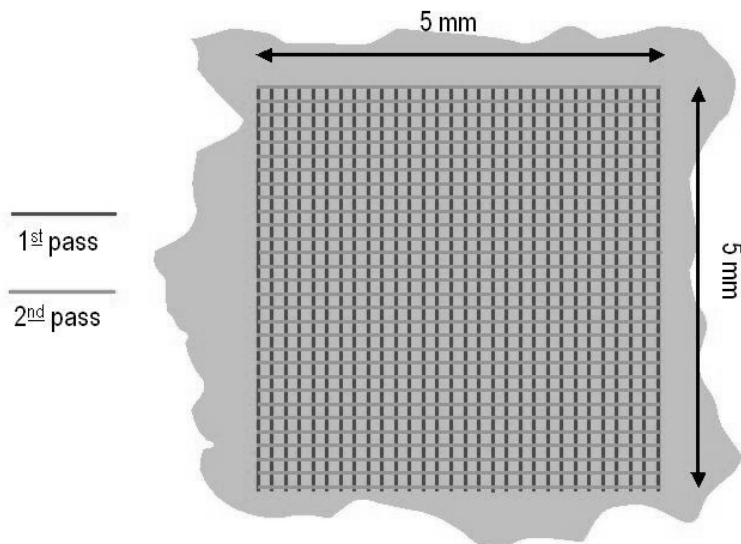
Figure C.2:
Laser beam scanning pattern for ablation of flavum ligament

Irradiations with and without water spray were conducted (in experiments without water spray an air jet was applied instead). Thus eight different combinations of irradiation parameters were used in these experiments altogether. With this irradiation pattern a rectangular ablation crater with a side length of about 5 mm was created. One ablation crater is shown in figure C.3.a.
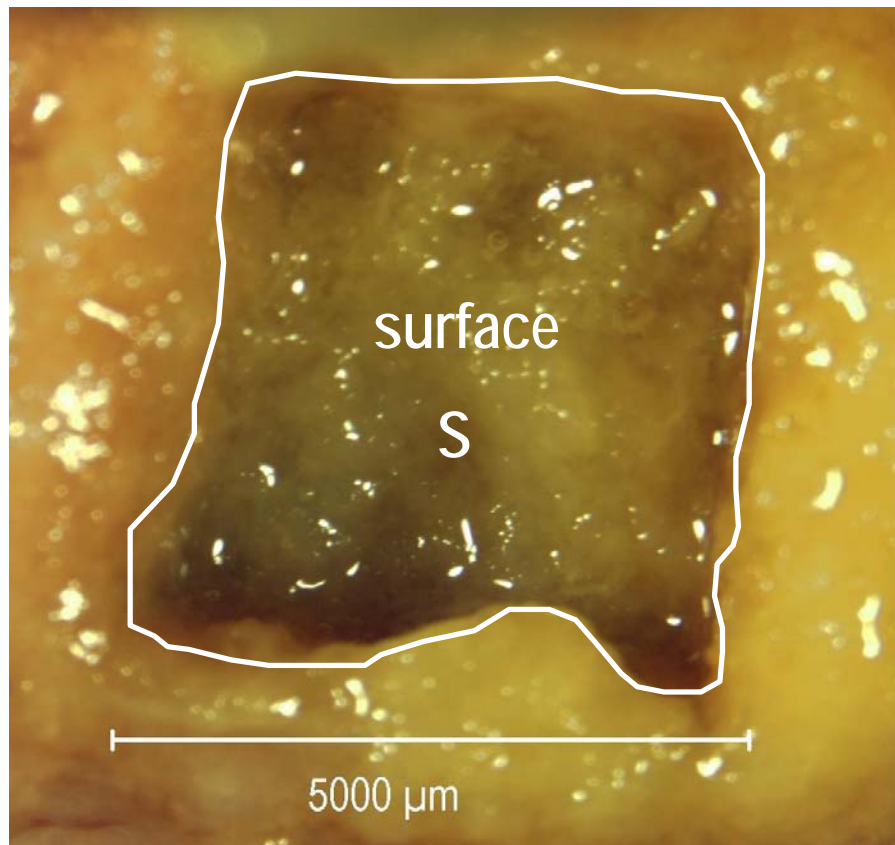
Figure C.3.a: ablation crater after irradiation with two sets of lines; (5000 pulses @ 56 µs and 62 mJ); irradiation with water spray
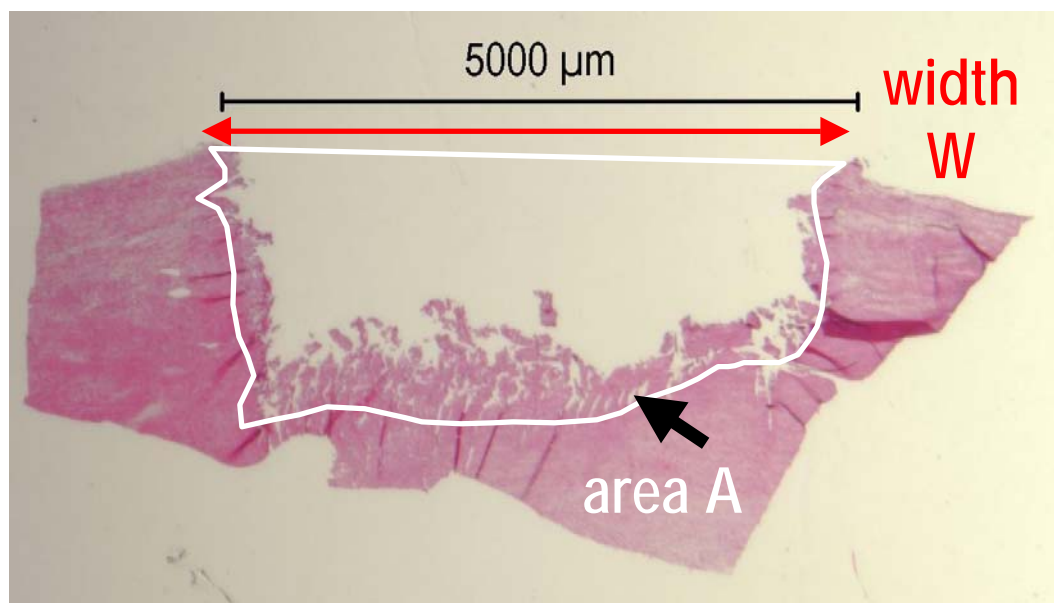
Figure C.3.b: Histological slice through the ablation crater of the same sample (two sets of lines; 5000 pulses @ 56 µs and 62 mJ; irradiation with water spray)

The volume of the ablation craters had to be determined for quantitative analysis. Since flavum ligament is a soft tissue the method of estimating the ablation volume by filling a known amount of water into the crater - as used for the teeth in appendix

B - was not used. It is not accurate enough; because the soft tissue soaked a part of the water filled in the crater into the tissue and is partly leaking out of the crater through tears in the tissue. Instead the volume was estimated by geometrical measurements. From photographs taken with the help of an optical microscope (Olympus SZX 12) of the ablation crater directly after the irradiation the "surface" area S was measured with an image processing software (Adobe Photoshop). From slices cut out of the samples parallel to the sides of the ablated rectangle for histological examination the cross-section area A can be measured (see figure C.3.b). The slices were also photographed under the microscope and the photos were analysed with the image processing software. From the square root of the measured surface area S the average side length of the ablation crater $L = \sqrt{S}$ was calculated. With the measured area of the crater cross-section and the calculated side length the ablated volume $V = L \cdot A$ could be calculated. Since the surface area S and with this the side length L of the ablation crater is measured on the native sample after the irradiation and the cross-section area A is measured from the histological slices after the corresponding preparation a scaling factor F was introduced. The scaling factor was calculated from $F = \left(L/W\right)^2$, where L is the calculated average side length in the native sample and W is the width (side length) of the ablation crater measured in the image of the histological slice. For the evaluation of the data an average scaling factor for all used samples was calculated and used for further calculations. When introducing the sacling factor F in the following way in the calculation of the ablated volume $V = L \cdot A \cdot F = \sqrt{S} \cdot A \cdot F$ the shrinking of the sample during the histological treatment was compensated.

Effective ablation of flavum ligament was possible with all parameter combinations. Visual inspection of the samples showed tissue parching and carbonisation of the tissue indicating thermal damage to the tissue in samples irradiated without additional water spray. There was no visible thermal damage in samples irradiated with additional water spray. Furthermore the water spray seemed to have a rinsing effect which removed tissue debris from the ablation crater. As expected, tissue damage revealed in histological examinations was more severe in

samples lased without water spray. Detailed histological results and further conclusions drawn from the histological slices will be found in [Rom0X].

In figure C.4 the ablated volume is plotted against the total applied energy. The total applied energy is the energy which is applied in total during the scanning process; this means 2500 times the pulse energy for one set of scanning lines and 5000 times the pulse energy for two sets of scanning lines. Due to the two different pulse durations i.e. two pulse energies there are four energy "steps". It is visible that - as expected - the ablated volume is increasing with rising applied energy over all. The filled symbols indicate the average values in the ablated volume for the different parameter settings. The behaviour of the average values show signs of a saturation in the ablation volume with increasing energy. This could be the result of the ragged structure of the bottom of the ablation crater, where filaments of cut but not removed tissue are emerging from the impact of single laser pulses. This filament layer (black arrow in figure C.3.b) will grow with increasing number of laser passes and reduce the ablation efficiency. A corresponding behaviour is visible in the plot of the specific ablation energy against the total applied energy in figure C.5. Here an increase in the specific ablation energy with rising total applied energy is visible. However it has to be said that the measured values for the ablated volume vary quite considerably due to the nature of the soft tissue. Moreover, the volumetric measurement procedure is problematic due to the fact that one measurement is taken from the native sample after irradiation and the other is taken from the histological slices. So the obtained values should only be taken as estimates for the specific ablation energy. What can be concluded is that the CO_2 laser can be used as an effective ablation tool for flavum ligament tissue. It should preferably be used in combination with a water spray to minimise thermal damage to the surrounding tissue.
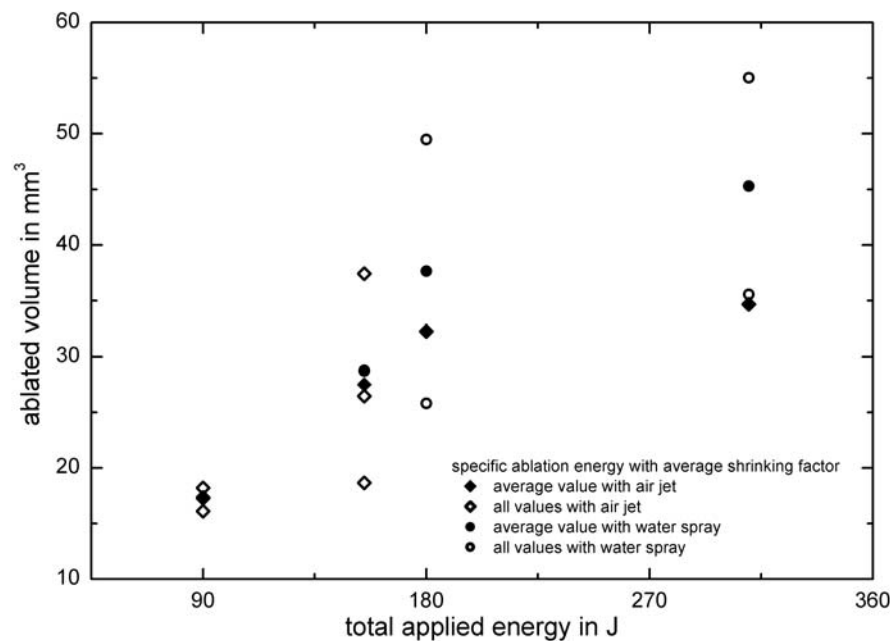
Figure C.4: ablated volume plotted against total applied energy, filled circles (●) average and open circles (O) individual ablated volume for irradiations with water spray, filled diamonds (◆) average and open diamonds (◇) individual ablated volume for irradiations with air jet
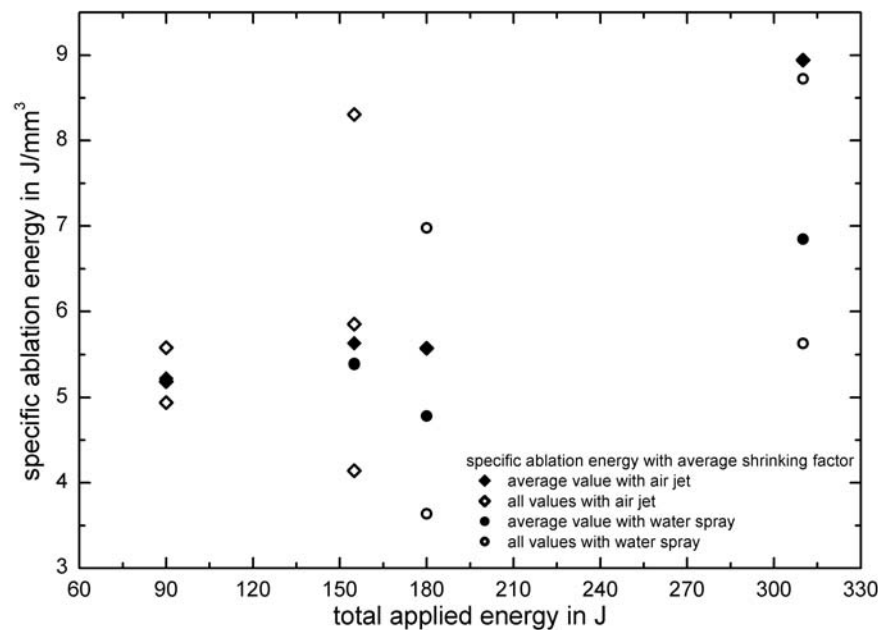
Figure C.5: specific ablation energy plotted against total applied energy, filled circles (●) average and open circles (O) individual specific ablation energy for irradiations with water spray, filled diamonds (◆) average and open diamonds (◇) individual specific ablation energy for irradiations with air jet

The described study about CO_2 laser induced ablation of yellow ligament was planned and realised as an experimental study. The final aim of the research would be the establishment of a minimal invasive laser procedure to remove yellow

ligament and decompress the spinal cord. A procedure involving the CO_2 laser could be only "partly minimal" invasive, since there are no usable commercially available bendable optical fibres for these wavelengths. One could use a short hollow waveguide though. However the flexibility and length of such a waveguide is limited because of the inherent loss mechanism of hollow waveguides.

Further experiments with a Holmium YAG laser (λ = 2.1 mm), which can be transmitted with a flexible standard optical fibre, yielded promising results. The specific ablation energy of yellow ligament for the Holmium YAG laser (Dornier medilas H) in contact ablation (with a 400 µm diameter fibre) at a pulse energy of 1.35 J at 10 Hz with 250 µs laser pulses is estimated to (21.2 $\pm$ 8.1) J/mm^3. The detailed results of this study will be reported later elsewhere.

D. Summary Medical Applications

The two laser applications introduced here (appendix B and C) together with the laser osteotomy of bone (described in chapter 4, 5 + appendix A) offer the possibility of an extended usability of the described laser ablation technique with short pulsed CO_2 lasers, additional water spray and fast multi-pass laser beam scanning in various fields of medicine. The contact less procedure with free cut geometries and easy integration in conventional operation planning and navigation systems in combination with medical imaging (CT, NMR, Holography etc.) could lead to fundamentally new operation techniques with increased accuracy as well as precision.

Appendix - Thermography

T.1 Black Body Radiation

A black body is defined as an object that absorbs all electromagnetic radiation which impinges on it at all wavelengths. Heated to a uniform temperature a black body emits electromagnetic radiation (black body radiation) whose characteristic is only determined by the temperature of the black body temperature. The emitted spectrum is described by Planck's law of black body radiation (expressed as a function of the wavelength). [Ger93]:

$$M_{bb}(\lambda,T) = \frac{2\pi hc^2}{\lambda^5} \frac{1}{e^{\frac{hc}{\lambda kT}} - 1} \qquad \text{(T.1)}$$

With $M_{bb}(\lambda,T)$: black body spectral radiant emittance at wavelength λ (in W/(m^2·m))

c velocity of light (2.998·10^{8}m/s)

h Planck's constant (6.625·10^{-34} Js)

k Boltzmann's constant (1.381·10^{-23}J/K)

T absolute temperature of the black body (in K)

λ wavelength of emitted radiation (in m)

When integrating the spectral radiant emittance (equation T.1) over the whole wavelength range one receives the Stefan-Boltzmann law for the total thermally emitted radiant power P of a black body with the surface area A [Ger93]:

$$P = A \cdot \sigma \cdot T^4 \qquad \text{(T.2)}$$

With P total thermally emitted radiant power (in W)

A surface area of the black body (in m^2)

σ Stefan-Boltzmann constant $\sigma = \dfrac{2\pi^5 k^4}{15c^2 h^3} = 5{,}67 \cdot 10^{-8} \dfrac{W}{m^2 K^4}$

T absolute temperature of the black body (in K)

However, real objects almost never comply with the conditions for a black body over the whole range of wavelengths. There are three processes which take place and prevent a real object from being a black body. A fraction a_λ of the incident radiation will be absorbed, a fraction r_λ will be reflected and another fraction will be transmitted t_λ. As already mentioned these factors add up to 1 (equation 2.1, discarding scattering in this case). A factor, the spectral emissivity $\varepsilon(\lambda,T)$ is needed to describe the fraction of the radiant emittance of a black body produced by an object at a specific temperature. The spectral emissivity is defined as the ratio of the spectral radiant emittance from an object to that from a black body at the same temperature and the same wavelength.

$$\varepsilon(\lambda,T) = \frac{M_{real}(\lambda,T)}{M_{bb}(\lambda,T)} \qquad\qquad (T.3)$$

$\varepsilon(\lambda,T)$ =1 for a black body radiator and $\varepsilon(\lambda,T) < 1$ for any real object. For a real object with an emissivity which is below 1 but constant for all wavelengths $\varepsilon(\lambda,T)$ = ε ("grey body") the Stefan-Boltzmann Law can be rewritten as:

$$P = \varepsilon \cdot A \cdot \sigma \cdot T^4 \qquad\qquad (T.4)$$
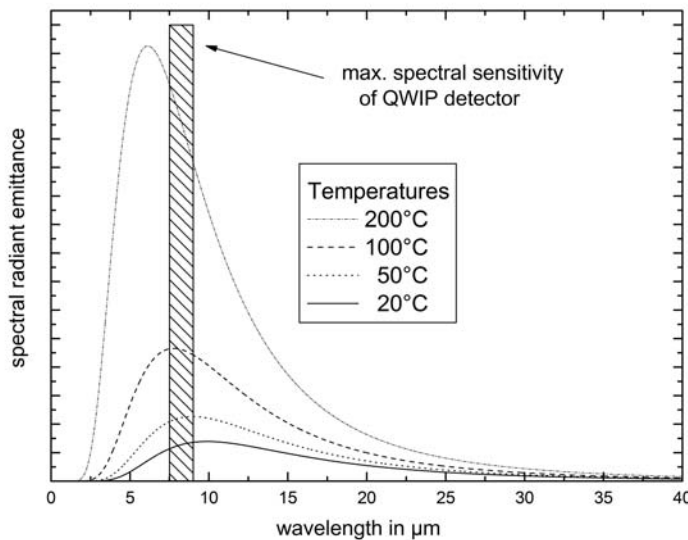

Figure T.1: spectral radiant emittance for a black body according to Planck's law (equation 9.1) for four temperatures

T.2 QWIP Detector

A QWIP (quantum well infrared photo detector) is a quantum well designed to detect infrared radiation by using inter sub-band transitions in the conduction band of GaAs/AlGaAs. Depending on the design these devices allow the detection of photons in the range of 3 to 16 µm [Gun03]. QWIP detectors are very attractive for the use in infrared cameras for thermal measurements in the long wavelength atmospheric window between 8 and 12 µm [Sch00]. The camera used in the experiments described in chapter 5.2 (Flir SC 3000) is based on these principles. A possible way to realise a QWIP detector is the square quantum well [Gun03]. A quantum well which is sufficiently deep and narrow has discrete quantised energy states. When the potential depth and width is well adjusted there are only two discrete states in the quantum well, a ground state near the well bottom and an excited state near the well top. An incident IR photon will excite an electron from the ground state to the excited state in the quantum well. An externally applied voltage will sweep the electrons out of the well and create a photocurrent which is proportional to the number of incident IR photons (see figure T.2).
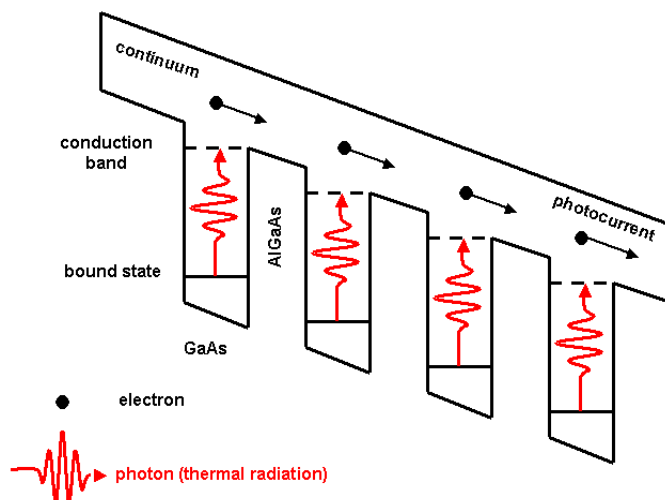

Figure T.2: Schematic diagram of the conduction band in a bound-to-quasibound QWIP in an externally applied electric field. Absorption of IR photons photo-excite electrons from the ground state of the quantum well into the continuum, causing a photocurrent. (graphic according to [Gun03])

Only photons having an energy corresponding to the energy separation of the two states in the quantum well will be able to excite the electrons and creating a photo current. This makes the construction of IR photo detectors with sharp absorption spectra possible, by tailoring the potential depth and width of the GaAS/AlGaAs semiconductor system [Gun03, Sch00].

T.3 Emissivity ε of Bone

As mentioned above the QWIP detector is still sensitive to stray light from the laser, so the camera was protected with a filter. This was done with one or two 5 mm thick CaF_2 windows, which absorbed each 87.5 % of the incident 10.6 μm radiation. The temperature scale of the camera could be calibrated by adjusting the emissivity of the sample in the software ("TCAM Researcher"). The change in the sensitivity of the camera caused by the absorption in the filter was corrected by adjustment of the emissivity factor in the camera software for the corresponding filtering. For this calibration samples of bone were heated uniformly in an oven over a temperature range from 100°C to 210°C (however the bone condition significantly changed at temperatures above 160 °C, when the bone blackened due to collagen carbonisation). The temperature of the bone sample was monitored with the IR camera and a K-type thermocouple. The emissivity value of the camera software was adjusted so that the temperature detected matched the temperature indicated by the thermocouple, which was taken as the real temperature of the sample. The emissivity ε of the bone sample was found to be constant over the measured temperature range for each filtering set-up. The values found for ε for the different filtering are summarised in table T.1. It was assumed that bone behaves as a grey body radiator which means that the emissivity ε is independent of the wavelength.

Table T.1: Estimations of the emissivity ε of compact bone dependent on the filtering of the camera

Filtering	Emissivity ε
Without filter	0.94
With 5 mm CaF_2	0.79
With 10 mm CaF_2	0.68

Bibliography

[Afi03]   Afilal S., Ivanenko M., Werner M., Hering P.; Osteotomie mit 80 µs CO_2-Laserpulsen; Fortschritt-Berichte VDI, 17. Biotechnik / Medizintechnik 231 (2003); pp. 164-169; (2003)

[Afi04]   Afilal S.; Ablationsmechanismen von biologischem Hartgewebe bei Bestrahlung mit kurzgepulsten CO_2 -Lasern; PhD Thesis; Institute of Laser Medicine; Heinrich-Heine-University; Düsseldorf; (2004) http://www.ub.uni-duesseldorf.de/home/etexte/diss/show?dissid=905

[Alb79]   Albright J.A.; Bone: Physical Properties; Scientific Basis of Orthopaedics; edt. Albright J.A., Brand R. A.; Appleton Century Crofts; New York; (1979)

[Alt97]   Alt K.W., Jeunesse C., Buitago-Tellez C.H., Wächter R., Boes E., Pichler S.L.; Evidence for stone age cranial surgery; Nature; 387; pp. 360 (scientific correspondence); (1997)

[Ape02]   Apel C., Meister J., Ioana R.S., Franzen R., Hering P., Gutknecht N.; The Ablation Threshold of Er:YAG and Er:YSGG Laser Radiation in Dental Enamel; Lasers in Medical Science; 17; pp. 246-252; (2002)

[Arm02]   Armstrong W.B., Neev J.A., Da Silva L.B., Rubenchik A.M., Stuart B.C.; Ultra-short Pulse Laser Ossicular Ablation and Stapedotomy in Cadaveric Bone; Lasers in Surgery and Medicine; 30; pp. 216-220; (2002)

[Ash01]   Ashouri N., Shori R., Cheung J.M., Fried D.; Infrared laser Ablation of Dental Enamel: Influence of an Applied Water Layer on Ablation Rate and Peripheral Damage; SPIE Proc. Lasers in Dentistry VII; Vol. 4249; pp. 72-78; (2001)

[Bar97]   Barton T.G., Foth H.-J., Christ M., Hörmann K.; Interaction of holmium laser radiation and cortical bone: ablation and thermal damage in a turbid medium; Applied Optics; 36(1); pp. 32-43; (1997)

[Biy86]   Biyikli S., Modest M.F., Tarr R.; Measurements of Thermal Properties for Human Femora; Journal of Biomed. Materials Research; 20; pp. 1335-1345; (1986)

[Bre05]   Brendemühl A., Werner M., Ivanenko M., Hering P., Buzug T.;
            Temperature Measurements with an IR Camera During Drilling and
            cutting of bone with a pulsed CO_2 Laser; Biomedizinische Technik; 50
            Suppl. Vol.1, Part 2; pp. 1264-1265; (2005)

[Car59]   Carslaw H.S., Jaeger J.C.; Conduction of heat in solids; Claredon
            Press; Oxford; (1959)

[Cho01]   Choi B., Welch A.J.; Analysis of Thermal Relaxation during Laser
            Irradiation of Tissue; Lasers in Surgery and Medicine; 29; pp. 351-359;
            (2001)

[Cla89]   Clauser C., Clayman L.; Effects of Exposure Time and Pulse
            Parameters on CO_2 Laser Osteotomies; Lasers in Surgery and
            Medicine; 9; pp. 22-29; (1989)

[Cop06]   Coppa A., Bondiolo L., Cucina A., Frayer D.W., Jarrige C., Jarrige
            J.-F., Quivron G., Rossi M., Vidale M., Macchiarelli R.; Early Neolithic
            tradition of dentistry; Nature; 440; pp. 755 (brief communications);
            (2006)

[Cor74]   Corcia J.T., Moody W.E.; Thermal analysis of human dental enamel;
            J Dental Res; 53; 3; pp. 571-580; (1974)

[Dat04]   Datta G., Gnanalingham K.K., Peterson D., Mendoza N., O'Neill K.,
            Van Dellen J., McGregor A., Hughes S.; Back Pain and Disability after
            Lumbar Laminectomy: Is there a Relationship to Muscle Retraction ?;
            Neurosurgery; 54; 6; pp. 1413-1420; (2004)

[Del04]   Dela Rosa A., Sarma A.V., Le C.Q., Jones R.S., Fried D.; Peripheral
            thermal and mechanical damage to dentin with microsecond and sub-
            microsecond 9.6 µm, 2.79 µm and 0.355 mm laser pulses;
            Lasers in Surgery and Medicine; 35; pp. 214-228; (2004)

[Dre91]   Dressel M., Jahn R., Neu W., Jungbluth K.H.; Studies in fiber guided
            laser surgery for cutting and drilling bone and meniscus;
            Lasers in Surgery and Medicine; 11; pp. 569-579; (1991)

[Duc90]   Duck F.A.; Physical Properties of Tissue;
            Academic Press; San Diego; (1990)

[El M97]   El Montaser M.A., Devlin H., Sloan P., Dickinson M.R.; Pattern of
            Healing of Calvarial Bone in the Rat Following Application of the
            Erbium-YAG Laser;
            Lasers in Surgery and Medicine; 21; pp. 255-261; (1997)

[Ert93]   Ertl T., Müller G.; Hard tissue ablation with pulsed CO_2 Lasers;
            Proc. of SPIE Vol.1880; pp. 176-181; (1993)

[Fea87]   Featherstone J.D.B., Nelson D.G.A.; Laser effects on dental hard tissue; Advanced Dental Research; 1; pp. 21-26; (1987)

[Fer04]   Fernandez-Seara M.A., Wehrli S.L., Takahashi M., Wehrli F.W.; Water Content Measured by Proton-Deuteron Exchange NMR Predicts Bone Mineral Density and Mechanical Properties; Journal of Bone and Mineral Research; 19; 2; pp. 289-295; (2004)

[For93]   Forrer M., Frenz M., Romano V., Altermatt H.J., Weber H.P., Silenok A., Istomyn M., Konov V.I.; Bone-Ablation Mechanism Using CO_2 Lasers of Different Pulse Duration and Wavelength; Applied Physics B; 56; pp. 104-112; (1993)

[Fow66]   Fowler B.O., Moreno E.C., Brown W.E.; Infra-red Spectra of Hydroxyapatite, octacalcium phosphate and pyrolysed octacalcium phosphate; Arch Oral Biol; 11; pp. 477; (1966)

[Fow86]   Fowler B.O., Kuroda S.; Changes in heated and in laser irradiated human tooth enamel and their probable effects on solubility; Calcif Tissue Int; 38; pp. 197-208; (1986)

[Fra95]   Fratzl P., Schreiber S., Klaushofer K.; Bone Mineralization as Studied by Small-Angle X-ray Scattering; Connective Tissue Research; 34; 4; pp. 247-254; (1995)

[Fre03]   Frentzen M., Götz W., Ivanenko M., Afilal S., Werner M., Hering P.; Osteotomy with 80-µs CO_2 laser pulses - histological results; Lasers in Medical Science; 18; pp. 119-124; (2003)

[Fre05]   Frey S.; Three-dimensional facial measurement by portrait holography and texture-based focus detection; PhD Thesis; Institute of Laser Medicine; Heinrich-Heine-University; Düsseldorf; (2005) http://www.ub.uni-duesseldorf.de/home/etexte/diss/show?dissid=1166

[Fri97]   Fried D., Glena R.E., Featherstone J.D.B., Seka W.,; Permanent and Transient Changes in the Reflectance of CO2 Laser-Irradiated Dental Hard Tissues at lamda = 9.3, 9.6, 10.3, and 10.6 µm and at Fluences of 1-20 J/cm^2; Lasers in Surgery and Medicine; 20; pp. 22-31; (1997)

[Fri98]   Fried D, Zuerlein M., Featherstone J.D.B., Seka W., Duhn C., McCormack S.; IR laser ablation of dental enamel: mechanistic dependence on the primary absorber; Applied Surface Science; 127-129; pp. 852-856; (1998)

[Fri01]   Fried D., Ragadio J., Akrivou M., Featherstone J.D., Murray M.W., Dickenson K.M.; Dental hard tissue modification and removal using sealed transverse excited atmospheric-pressure lasers operating at λ = 9.6 and 10.6 µm; J. of Biomedical Optics; 6(2); pp. 231-238; (2001)

[Fri02]   Fried D., Ashouri N., Breunig T., Shori R.; Mechanism of Water
              Augmentation During IR Laser Ablation of Dental Enamel; Lasers in
              Surgery and Medicine; 31; pp. 186-193; (2002)

[Fun93]   Fung Y.C.; Chapter 12: Bone and Cartilage; Biomechanics -
              Mechanical properties of Living Tissue; Springer-Verlag; New York,
              Berlin, Heidelberg; (1993)

[Gar03]   Garratt-Reed A.J., Bell D.C.; Energy-dispersive X-Ray Analysis in the
              Electron Microscope; Chapter 2: Principles; Microscopy Handbooks;
              edt. Rainforth M.; BIOS Scientific Publishers Limited; Oxford; (2003)

[Ger81]   Gertzbein S.D., deDemeter D., Cruickshank B., Kapasouri A.;
              The Effect of Laser Osteotomy on Bone Healing;
              Lasers in Surgery and Medicine; 1; pp. 361-373; (1981)

[Ger93]   Gerthsen C., Vogel H.; Physik; Chapter 11.2: Strahlungsgesetze;
              Springer Verlag; Berlin, Heidelberg; (1993)

[Gun03]   Gunapala S.D., Bandara S.V., Liu J.K., Rafol S.B., Mumolo J.M.,Shott
              C.A., Jones R., Woolaway J. II., Fastenau J.M., Liu A.K., Jhabvala M.,
              Choi K.K.; 640 x 512 pixel narrow-band, four-band, and broad-band
              quantum well infrared photodetector focal plane array; Infrared Physics
              and Technology; 44; pp. 411-425; (2003)

[Her01]   Hering P., Mitra T., Ivanenko M.; Patent DE 10133341A1
              "Laserschneiden"; (2001)

[Hib89]   Hibst R., Keller U.; Experimental Studies of the application of the
              Er.YAG Laser on Dental Hard Substances: I. Measurement of the
              Ablation Rate; Lasers in Surgery and Medicine; 9; pp. 338-344; (1989)

[Hib93]   Hibst R., Keller U.; The mechanism of Er:YAG laser induced ablation
              of dental hard substances; Proc. of SPIE Vol.1880; pp. 156-162;
              (1993)

[Hib97]   Hibst R.; Technik, Wirkungsweise und medizinische Anwendung von
              Holmium- und Erbium-Lasern; Chapter 3: Untersuchungen zur Physik
              der Gewebeablation; Fortschritte in der Lasermedizin; edt. Müller G.J.,
              Berlien H.-P.; ecomed; Landsberg; (1997)

[Hor77]   Horch H.-H.; Laser-Osteotomie und Anwendungsmöglichkeiten des
              Lasers in der oralen Weichteilchirurgie; Chapter 6: Eigene
              Untersuchungen; Medizinische Fakultät; Heinrich-Heine-Universität;
              Düsseldorf; (1977)

[Hua91]   Huang D., Swanson E.A., Lin C.P., Schuman J.S., Stinson W.G., Chang W., Hee M.R., Flotte T., Gregory K., Pulifato C.A., Fujimoto J.G.; Optical Coherence Tomography; Science; 254; 5035; pp. 1178 - 1181; (1991)

[Iva98]   Ivanenko M.M., Hering P.; Wet bone ablation with mechanically Q-switched high-repetition-rate CO_2 laser; Applied Physics B; 67; pp. 395-397; (1998)

[Iva98b]   Ivanenko M.M., Hering P.; Hard tissue ablation with a mechanically Q-switched CO_2 laser; SPIE Proc. Laser Welding and Tissue Interaction; 3565; pp. 110-115; (1998)

[Iva00]   Ivanenko M., Mitra T., Hering P.; Hard tissue ablation with sub-µs CO_2 laser pulses with the use of an air-water spray; SPIE Proc. Optical Biopsy and Tissue Optics; 4161; pp. 46-51; (2000)

[Iva00b]   Ivanenko M.M., Eyrich G., Bruder E., Hering P.; In vitro incision of bone tissue with a Q-switch CO2 laser . Histological examination; Lasers in Life Sciences; 9; pp. 171-179; (2000)

[Iva02]   Ivanenko M., Fahimi-Weber S., Mitra T., Wierich W., Hering P.; Bone Tissue Ablation with sub-µs Pulses of a Q-switch CO_2 Laser: Histological Examination of Thermal Side-Effects; Lasers in Medical Science; 17; pp. 258-264; (2002)

[Iva05]   Ivanenko M., Werner M., Afilal S., Klasing M., Hering P.; Ablation of hard bone tissue with pulsed CO_2 lasers; Medical Laser Application; 20; pp. 13-25; (2005)

[Iva05b]   Ivanenko M., Sader R., Afilal S., Werner M., Hartstock M., v.Hänisch C., Milz S., Erhardt W., Zeilhofer H-F., Hering P.; In Vivo animal Trials with a Scanning CO_2 Laser Osteotome;
            Lasers in Surgery and Medicine; 37; pp. 144-148; (2005)

[Iva05c]   Ivanenko M., Afilal S., Werner M., Hering P.; Bone Tissue Ablation with CO_2 Lasers at different Pulse Durations; SPIE Proc. Vol. 5863 - Therapeutic Laser Applications and Laser-Tissue Interactions II; pp.; (2005)

[Iza90]   Izatt J.A., Albagli D., Tzkan I., Feld M.S.; Pulsed laser ablation of calcified tissue: Physical mechanisms and fundamental parameters; Proc. of SPIE Vol.1202, Laser Tissue Interaction; pp. 133-140; (1990)

[Iza90b]   Izatt J.A., Sankey N.D., Partovi F., Fitzmaurice M., Rava R.P., Itzkan I., Feld M.; Ablation of Calcified Biological Tissue Using Pulsed Hydrogen Fluoride Laser Radiation; IEEE Journal of Quantum Electronics; 26(12); pp. 2261-2269; (1990)

[Jah92]   Jahn R., Dressel M., Neu W., Jungbluth K.H.; Abtragung von
            biologischem Hartgewebe mit dem Excimerlaser; Unfallchirurgie; 18
            (Nr.5); pp. 261-265; (1992)

[Jan93]   Jansen D.E., Chundru R.K., Samanani S.A., Tibbetts T.A., Welch A.J.;
            Pulsed Infrared Laser Irradiation of biological Tissue: Effect of Pulse
            Duration and Repetition Rate;
            Proc. of SPIE Vol.1882, Laser Tissue Interaction IV; (1993)

[Jel84]   Jellinek H.H.G., Srinivasan R.; Theory of etching polymers by far
            ultraviolet, high-intensity pulsed laser and long-term irradiation;
            J Phys Chem; 88; pp. 3048-3051; (1984)

[Kur84]   Kuroda S., Fowler B.O.; Compositional, structural and phase changes
            in in-vitro laser-irradiated human tooth enamel;
            Calcified Tissue Int.; 36; pp. 361-369; (1984)

[Kut05]   Kuttenberger J., Sader R., Stübinger S., Waibel A., v. Rechenberg B.,
            Ivanenko M., Zeilhofer H.F., Hering P.; Frakturheilung nach
            Osteotomie mit einem kurzgepulsten CO_2-Laser Tierexperimentelle
            Ergebnisse an der Schaftibia; 24. Internationales Symposium für
            Mund-Kiefer-Gesichtschirurgen, Oralchirurgen und Zahnärzte; St.
            Anton; (2005)

[Kut05b]   Kuttenberger J., Sader R., Stübinger S., Waibel A., v. Rechenberg B.,
            Ivanenko M., Zeilhofer H.F., Hering P.; Fracture healing under
            functional loading after laser osteotomy with a short-pulsed CO_2-Laser
            results of an animal study in the tibia of the sheep;
            CO-ME Combined 2005 Symposium; Bern; (2005)

[Lus91]   Lustmann J., Ulmansky M., Fuxbrunner A., Lewis A.;
            193 nm Excimer Laser Ablation of Bone;
            Lasers in Surgery and Medicine; 11; pp. 51-57; (1991)

[Lus92]   Lustmann J., Ulmansky M., Fuxbrunner A., Lewis A.; Photo acoustic
            injury and bone healing following 193nm excimer laser ablation;
            Lasers in Surgery and Medicine; 12; pp. 369-396; (1992)

[Mai60]   Maiman T.H.; Stimulated Optical Radiation in Ruby;
            Nature; 187; pp. 493-494; (1960)

[Maj98]   Majaron B., Sustercic D., Lukac M., Skaleric U., Funduk N.;
            Heat diffusion and debris screening in Er:YAG laser ablation of hard
            biological tissues; Applied Physics B; 66; pp. 479-487; (1998)

[Mar99]   Martin R.B.; Bone as a ceramic composite material;
            Material Science Forum; 293; pp. 5-16; (1999)

[Mar05]   Martinem H., Hage H., Rath W., Frauenpreiß T.; Diffusionsgekühlte CO_2-Slab-Laser: 10 Jahre kontinuierliche Entwicklung zu Leistung, Strahlqualität und Markterfolg; Eurolaser; 2/05; pp. (2005)

[McK90]   McKenzie A.L.; Physics of thermal processes in laser-tissue interaction; Phys. Med. Biol.; 35; 9; pp. 1175-1209; (1990)

[Mey96]   Meyer D., Foth H.-J.; Bearbeitung von Zahnhartsubstanz mit sehr kurzen CO_2-Laserpulsen / Treatment of Hard Dental Tissue by Very Short CO_2 Laser Pulses; Lasermedizin; 12; pp. 58-66; (1996)

[Mit02]   Mitra T.; Ablation biologischen Hartgewebes mit gepulsten IR-Lasern; Institute of Laser Medicine; PhD Thesis; Heinrich-Heine-University; Düsseldorf; (2002);
           http://www.ub.uni-duesseldorf.de/home/etexte/diss/show?dissid=220

[Mül02]   Müllejans R., Eyrich G., Raab W.H.-M., Frentzen M.; Cavity Preparation Using a Super-pulsed 9.6-µm CO_2 Laser - A Histological Investigation; Lasers in Surgery and Medicine; 30; pp. 331-336; (2002)

[Mur04]   Murray A.K., Dickinson M.R.; Tissue ablation-rate measurements with a long-pulsed, fibre-deliverable 308 nm excimer laser; Lasers in Medical Science; 19; pp. 127-138; (2004)

[Mür05]   Mürtz M.; Breath diagnostics using laser spectroscopy; Optics & Photonics News; 16; pp. 30-35; (2005)

[Nak99]   Nakamura Y., Hossain M., Watanabe H., Tokonabe H., Matsumoto N., Matsumoto K.; Morphological Changes of Rat Mandibular Bone with ArF Excimer Laser in Vivo; Journal of Clinical Laser Medicine & Surgery; 17(4); pp. 145-149; (1999)

[Nee96]   Neev J., Da Silva L.B., Feit M.D., Perry M.D., Rubenchik A.M., Stuart B.C.; Ultrashort Pulse Lasers for Hard Tissue Ablation; IEEE Journal of selected Topics in Quantum Electronics; 2(4); pp. 790-800; (1996)

[New77]   Newesely H.; High temperature behaviour of hydroxy- and fluorapatite; Journal of Oral Rehabilitation; 4; pp. 97-104; (1977)

[Nie94]   Niemz M.H.; Investigation and Spectral Analysis of the Plasma-Induced Ablation Mechanism of Dental Hydroxyapatite;
           Applied Physics B; 58; pp. 273-281; (1994)

[Nie96]   Niemz M.H.; Laser-Tissue Interactions; Chapter 3 Interaction Mechanisms; Springer Verlag; Berlin Heidelberg NewYork; (1996)

[Nis01]   Nishikawa H.; Thermal behavior of hydroxyapatite in structural and spectrophotometric; Material Letters; 50; pp. 364-370; (2001)

[Nus88]   Nuss R.C., Fabian R.L., Sarkar R., Puliafito C.A.; Infrared Laser Bone Ablation; Lasers in Surgery and Medicine; 8; pp. 381-391; (1988)

[OLE99]   Optics develops ways to support medicine; Optics & Lasers Europe; pp. 29-32; (September 1999)

[Oxford]   Oxford Systems; Manual Oxford INCA;

[PC]   personal communication Dr. M. Ivanenko; Research Centre caesar, Bonn;

[Pea99]   Peavy G.M., Reinisch L., Payne J.T., Venugopalan V.; Comparison of Cortical Bone Ablations by Using Infrared Laser Wavelengths 2.9 to 9.2 µm; Lasers in Surgery and Medicine; 26; pp. 421-434; (1999)

[Rau98]   Rauber A., Kopsch F.; Anatomie des Menschen Lehrbuch und Atlas; Bd. 1 Der Bewegungsapparat; edt. Tillmann B., T. G., Zilles K.; Georg Thieme Verlag; Stuttgart; (1998)

[Rho98]   Rho J-Y., Kuhn-Spearing L., Zioupos P.; Mechanical properties and the hierarchical structure of bone; Medical Engineering & Physics; 20; pp. 92-102; (1998)

[Rog03]   Roggan A., Binding U., Wäsche W., Zgoda F.; Properties of Biological Tissues (Chapter I-3.1); Applied Laser Medicine; edt. Berlien H-P., Müller G. J.; Springer Verlag; Berlin, Heidelberg, New York,; (2003)

[Ro0X]   Rommel F., Herdmann J., Werner M., Ivanenko M., Hering P.; Volumetric tissue ablation-rate measurements with a CO_2 laser on human flavum ligament; (to be published)

[San97]   Sanchez F., Espana Tost A.J., Morenza J.L.; ArF excimer laser irradiation of human dentin; Lasers in Surgery and Medicine; 21; pp. 474-479; (1997)

[Sas02]   Sasaki K.M., Aoki A., Ichinose S., Ishikawa I.; Ultra structural analysis of bone tissue irradiated by Er:YAG Laser; Lasers in Surgery and Medicine; 31; pp. 322-332; (2002)

[SC3000]   Flir Systems; Manual Therma CAM SC 3000; Danderyd, Schweden (2002)

[Sch92]   Scholz C.; Neue Verfahren der Bearbeitung von Hartgewebe in der Medizin mit dem Laser; Advances in Lasermedicine 7; Chapter 5: Das Schneiden und Abtragen von Knochen mit dem Laser; edt. Müller G.J., Berlien. H.-P.; ecomed; Landsberg/Lech; (1992)

[Sch92b]   Scholz C., Grothves-Spork M.; Die Bearbeitung von Knochen mit dem Laser (Kapitel III -3.11.1); Angewandte Lasermedizin 6; edt. Berlien H-P., Müller G. J.; ecomed; Landsberg/Lech; (1992)

[Sch00]   Schneider H., Walther M., Schönbein C., Rehm R., Fleissner J., Pletschen W., Braunstein J., Koidl P., Weimann G., Ziegler J., Cabanski W.; QWIP FPAs for high-performance thermal imaging; Physica E; 7; pp. 101-107; (2000)

[See98]   Seeley R.R., Stephens T.D., Tate P.; Anatomy and Physiology; Chapter 6: Skeletal System: Bones and Bone Tissue; McGraw-Hill; Boston; (1998)

[She04]   Sheth K.K., Staninec M., Sarma A.V., Fried D.; Selective targeting of protein, water and mineral in dentin using UV and IR pulse lasers: The effect on the bond strength to composite restorative materials; Lasers in Surgery and Medicine; 35; pp. 245-253; (2004)

[Spe99]   Spencer P., Payne J.M., Cobb C.M., Reinisch L., Peavy G.M., Drummer D.D., Suchman D.L., Swafford J.R.; Effective Laser Ablation of Bone Based on the Absorption Characteristics of Water and Proteins; Journal of Periodontology; 70; 1; pp. 68-74; (1999)

[Sta01]   Stanislawski M., Meister J., Mitra T., Ivanenko M.M., Zanger K., Hering P.; Hard tissue ablation with a free running Er: YAG and a Q-switched CO_2 laser : a comparative study; Applied Physics B; 72; pp. 115-120; (2001)

[Ste64]   Stern R.H., Sognnaes R.F.; Laser beam effect on dental hard tissue; Journal of Dental Research; 43; pp. 873; (1964)

[Ste66]   Stern R.H., Sognnaes R.F., Goodman F.; Laser Effect on in vitro enamel permeability and solubility; Journal Am Dent Assoc; 78; pp. 838-843; (1966)

[Stü05]   Stübinger S., Werner M., Ivanenko M., Sader R., Hering P., Zeilhofer H.-F.; Retrograde root canal therapy with a pulsed CO_2 Laser - an in-vitro study in human tooth; Esola - Laser Congress; Barcelona; (2005)

[Sut86]   Sutcliffe E., Srinivasan R.; Dynamics of UV laser ablation of organic polymer surfaces; J. Appl. Phys.; 60; pp. 3315-3322; (1986)

[v.B05]   v.Borstel M., Ederer S., Zefferer H.; CO_2-Laser: the ultimate laser power; Laser Technik Journal; No.2; pp. (2005)

[Vis96]   Visuri S.R., Walsh J.T., Wigdor H.A.; Erbium Laser Ablation of Dental Hard Tissue: Effect of water cooling; Lasers in Surgery and Medicine; 18; pp. 294-300; (1996)

[v.Hän03]   von Hänisch C.; Osteogenese nach Laserosteotomie mit einem CO_2 Laser im Vergleich zur Osteotomie mit konventioneller Sägetechnik - eine tierexperimentelle Studie; Doktorarbeit,Tierärztliche Fakultät; Ludwig-Maximilians Universität; München; (2003)

[Wal89]   Walsh J.T., Flotte T.J., Deutsch T.F.; Er:YAG Laser Ablation of Tissue: Effect of Pulse Duration and Tissue Type on Thermal Damage; Lasers in Surgery and Medicine; 9; pp. 314-326; (1989)

[Wal91]   Walsh J.T., Deutsch T.F.; Measurement of Er:YAG Laser Ablation Plume Dynamics; Applied Physics B; 52; pp. 217-224; (1991)

[Wei92]   Weiner S., Traub W.; Bone structure: from Angstroms to microns; The FASEB Journal; 6; pp. 879-885; (1992)

[Wei98]   Weiner S., Wagner H.D.; The Material Bone: Structure-Mechanical Function Relation; Annu. Rev. Mater.Sci.; 28; pp. 271-298; (1998)

[Wei99]   Weiner S., Traub W., Wagner H.D.,; Lamellar Bone: Structure-Function Relation; Journal of Structural Biology; 126; pp. 241-255; (1999)

[Wer05]   Werner M., Afilal S., Ivanenko M., Klasing M., Hering P.; Laserosteotomie mit gepulsten CO_2-Lasern; Aktuelle Methoden der Laser- und Medizintechnik, Berlin, VDE (2. Remagener Physiktage); pp. 275-280; (2005)

[Whi00]   Whitters C.J., Strang R.; Preliminary Investigation of a Novel Carbon Dioxide Laser for Applications in Dentistry; Lasers in Surgery and Medicine; 26; pp. 262-269; (2000)

[Wil01]   Williams G.J., Zhigilei L.V., Garrison B.J.; Laser ablation in a model two-phase system; Nuclear Instruments and methods in Physics Research B; 180; pp. 209-215; (2001)

[Win02]   Wintermantel E., Ha S.; Medizintechnik mit biokompatiblen Werkstoffen und Verfahren; Chapter 7.3: Knochengewebe; Springer-Verlag; Berlin, Heidelberg, New York; (2002)

[Wit87]   Witteman W.J.; The CO_2 Laser; Chapter 4-6: Different CO_2 Laser Systems; Springer Series in Optical Sciences; edt. Shimoda K.; Spinger-Verlag; Berlin, Heidelberg, New York; (1987)

[Wol71]   Wolbarsht M.L.; Laser applications in medicine and biology; Plenum Press; New York; (1971)

[Won00]   Wong B.J.F., Gibbs L., Neev J., Shanks J.; Measurement of Acoustic
            Transients During Pulsed Holmium: YAG Laser Ablation of Cadaveric
            Human Temporal Bone; Lasers in Medical Science; 15; pp. 2-5; (2000)

[Yan72]   Yannas I.V.; Collagen and Gelatine in the Solid State;
            J. Macromol. Sci. Rev. Macromol. Chem.; 1; pp. 49-104; (1972)

[Yow89]   Yow L., Nelson S., Berns M.; Ablation of Bone and
            Polymethylmethacrylate by an XeCl (308 nm) Excimer Laser; Lasers in
            Surgery and Medicine; 9; pp. 141-147; (1989)

[Zah97]   Zahn H., Jungnickel V., Ertl T., Schmid S., Müller G.;
            Knochenchirurgie mit dem Er: YAG-Laser / Bone Surgery with Er: YAG
            Laser; Lasermedizin; 13; pp. 31-36; (1997)

[Zar61]   Zaret M.M., Breinin G.M., Schmidt H., Ripps H., Siegel I.M., Solon
            L.R.; Ocular lesions produced by an optical maser (laser); Science;
            134; pp. 1525; (1961)

Acknowledgements

I also want to thank all the members of the trace gas group at the University Düsseldorf for the very good and pleasant collaboration.

Prof. Dr. Thorsten Buzug is gratefully acknowledged for the possibility to use the IR camera of the RheinAhrCampus in our lab for thermal measurements of bone ablation and the very good and pleasant cooperation.

For their help with the SEM and EDX analysis I want to thank Dr. Barbara Wehner and Rene Borowski.

Dr. Frank Rommel is thanked for the very good and pleasant collaboration within the scope of the laser ablation of flavum ligament.

Dr. Dr. Johannes Kuttenberger is thanked for the very good and pleasant collaboration within the scope of the clinical in-vivo trials of the laser osteotomy on sheep.

Dr. Stefan Stübinger is thanked for the very good and pleasant collaboration within the scope of the laser treatment of teeth.

I wish also to acknowledge the support of the caesar foundation in Bonn that provided excellent working conditions and an inspiring interdisciplinary working environment.

And of course I want to thank all my friends, for being there and giving me encouragement and offer their companionship whenever I needed it.

Especially I want to thank my parents Irmhild and Dr. Siegfried Werner for their enduring encouragement and support over all the years.

Die hier vorgelegte Dissertation habe ich eigenständig und ohne unerlaubte Hilfe angefertigt. Die Dissertation wurde in der vorgelegten oder in ähnlicher Form noch bei keiner anderen Institution eingereicht. Ich habe bisher keine erfolglosen Promotionsversuche unternommen.

Düsseldorf, den 24.07.2006

_____
(Martin Werner)